Fy2015 Progress Report To:

the

Japan Aerospace Exploration Agency

Project title:

Validation of global water and energy balance monitoring in the Australian Murray-Darling Basin using GCOM-W1 data

Specification No: JX-PSPC-402691; Contract No: 14RSTK-01528

Investigators:

Jeffrey Walker, Christoph Rüdiger, Jason Beringer, Edoardo Daly, Olivier Merlin

Contributors:

Gift Dumedah, Alessandra Monerris-Belda, Mei Sun Yee, Frank Winston, Darren Hocking

March 2016

MONASH University
Engineering

Executive Summary

This report outlines project activities carried out in the past year in the Yanco area, Australia to (i) maintain the JAXA flux monitoring tower and validation site, (ii) evaluate two soil moisture retrieval algorithms used to validate AMSR-2 soil moisture against in-situ soil moisture, (iii) evaluate MTSAT evapotranspiration against those obtained from the flux tower and scintillometer observations, and (iv) evaluate updated evapotranspiration obtained from soil moisture assimilation against in-situ data. It was found that the two soil moisture retrieval methods have similar accuracies but with differences in performance for observation frequencies of C-band and X-band. Moreover, the integration of AMSR2 Level 3 soil moisture into the Joint UK Land Environment Simulator (JULES) has been demonstrated to improve soil moisture estimation but with no positive impact on evapotranspiration.

Contents

List of Tables

List of Figures

Chapter 1

Introduction

This report presents a summary of tasks undertaken during the FY2015 for the project titled: 'Validation of global water and energy balance monitoring in the Australian Murray-Darling Basin using GCOM-W1 data'. The project objectives include i) validation of the low resolution AMSR2 soil moisture product, ii) validation of the derived high resolution soil moisture products from multi-sensor downscaling, iii) validation of the derived root zone soil moisture from land surface data assimilation, and iv) validation of the derived land surface fluxes from land surface data assimilation. In line with these objectives, research activities have been undertaken in the past year to maintain and analyze weather and flux observation tower, and assimilate AMSR2 soil moisture into a land surface model to derive model land surface fluxes. Other stated objectives will be the focus of subsequent years. Consequently, this report presents detailed descriptions for the following research activities.

a) Maintenance of the JAXA flux monitoring tower and validation site

b) Validation of AMSR-2 soil moisture retrieved using JAXA and LPRM algorithms against in-situ soil moisture obtained from representative monitoring stations.

c) Evaluation of the MTSAT evapotranspiration against those obtained from the EC flux tower and scintillometer observations.

d) Data assimilation of AMSR2 soil moisture into the Joint UK Land Environment Simulator (JULES) model, validated against in-situ soil moisture and evaluation of model evapotranspiration.

1.1 Study site description - Yanco

The Yanco area shown in Figure 1.1 is a $60km \times 60km$ area located in the western plains of the Murrumbidgee Catchment, an area where the topography is flat with very few geological outcroppings. The locations of the OzNet stations (Smith et al., 2012) within the Yanco area are indicated with blue (surface-only measurements) and red circles (profile measurements), whereas the location of the flux tower and weather station from JAXA are indicated with green circles. Soil types are predominantly sandy loams, scattered clays, red brown earths, transitional red brown earth, sands over clay, and deep sands. According to the Digital Atlas of Australian Soils, dominant soil is characterized by plains with domes, lunettes, and swampy depressions, and divided by continuous or discontinuous low river ridges associated with prior stream systems (McKenzie et al., 2000). The area is traversed by present stream valleys with layered soil or sedimentary materials common at fairly shallow depths, along with primary soils of hard alkaline red soils, grey and brown cracking clays.

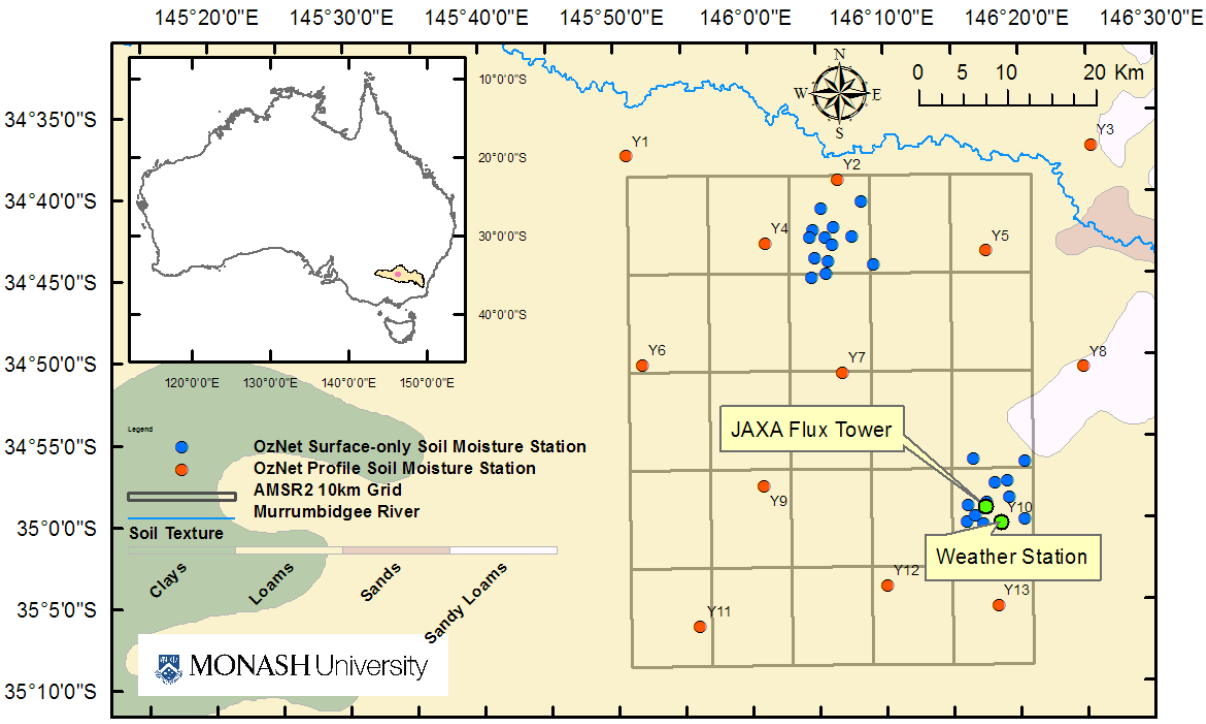

Figure 1.1: *Overview of the Murrumbidgee River catchment in Australia (inset), with focus on the Yanco study area showing soil moisture monitoring stations (from OzNet), the flux tower and weather station from JAXA, and soil textural classes according to the digital Atlas of Australian Soils.*

Chapter 2

Flux tower maintenance and upgrades

Regular site maintenance carried out during 2015 included cleaning of rain gauge, radiation sensors and solar panels, trimming long grass surrounding the solar panels and insect control. New multiplexers were purchased to replace the existing ones that were nearing the end of their rated lifetime. The installation of these is discussed in more detail in the section below. Some problems with noisy sensors were detected early in 2016 and these are also discussed in the sections below. The causes for these faults will be checked and rectified in upcoming field trips. The infra-red gas analyser calibration is planned for the next trip on 29/2/2016. The details of the calibration will not be available in time for inclusion in this report and will appear in next year's report. On 1/3/2016 all four temperature and humidity sensors were replaced with new units supplied by JAXA, since humidity sensors can deteriorate after a number of years in service.

2.1 New Multiplexers

Two new AM16/32B multiplexers were ordered from Campbell Scientific Australia in June 2015. These were fitted in place of the old ones on 3/9/2015. The new multiplexers were an upgraded version with a plug and socket arrangement for the signal connections, making wiring and installation much simpler. The photo in Figure 2.1 shows the replacement in progress.

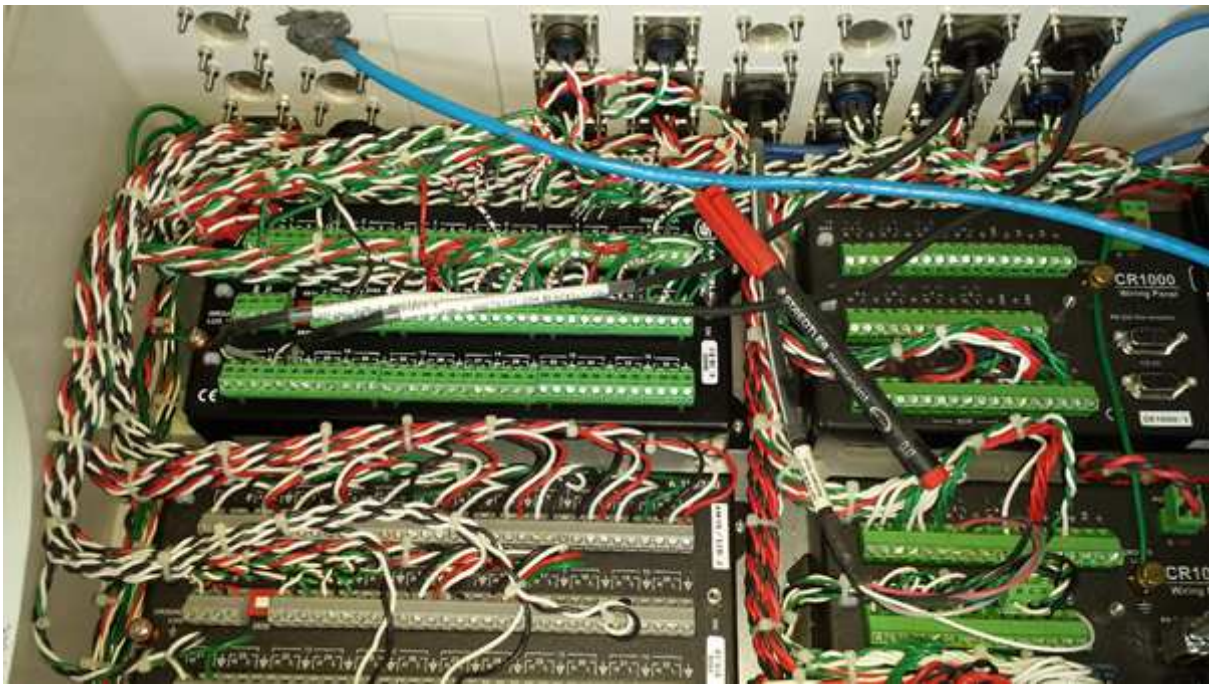

Figure 2.1: *An image showing the multiplexer changeover.*

2.2 Data and Sensor Issues

The RTD temperature sensors gradually developed noisy signals starting mid-2014 and worsening during 2015. Currently, there are random temperature fluctuations of 1.5 to 1.8^oC. The problem began around July 2014 with fluctuations up to 1.0^oC on T5 and gradually T4 and T3 began to be affected as well, until by January 2016 T3, T4 and T5 exhibited fluctuations up to 1.8^oC. Typically the fluctuations occur during daylight hours as shown in Figure 2.2.

This problem is unlikely to be caused by the multiplexer as the problem was evident before and after the change to new multiplexers. Campbell Scientific have remarked that the temperature fluctuations only occur during daylight hours and therefore the solar panel regulators should be investigated. The regulators use pulse width modulation of the charging voltage and could be imposing an AC ripple onto the supply voltage. During the next trip, capacitive input line filtering will be tested to see if the noise can be eliminated. If no obvious problems can be found, consideration should be given to installing new RTD temperature sensors. In the meantime, clipping outliers in the data and averaging will give reasonable values for the soil temperature. The deepest Trime Pico soil moisture sensor (Soil Water5) appears to have failed on 23rd January 2016. The graph below shows the data giving unusual spikes for a few days and then dropping to near-zero. The wiring and connections were checked without any obvious

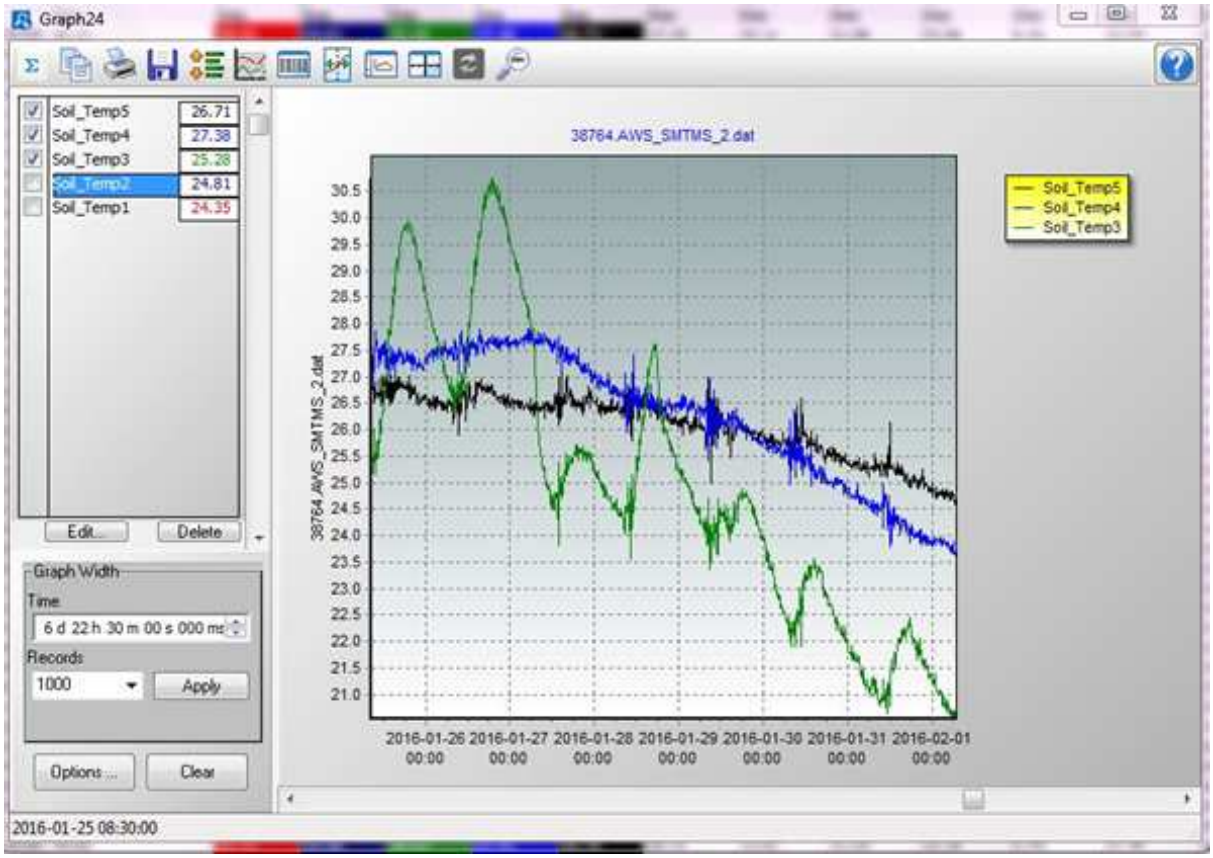

Figure 2.2: *Graph showing soil temperature data from January 2016 and displaying random fluctuations during daylight hours.*

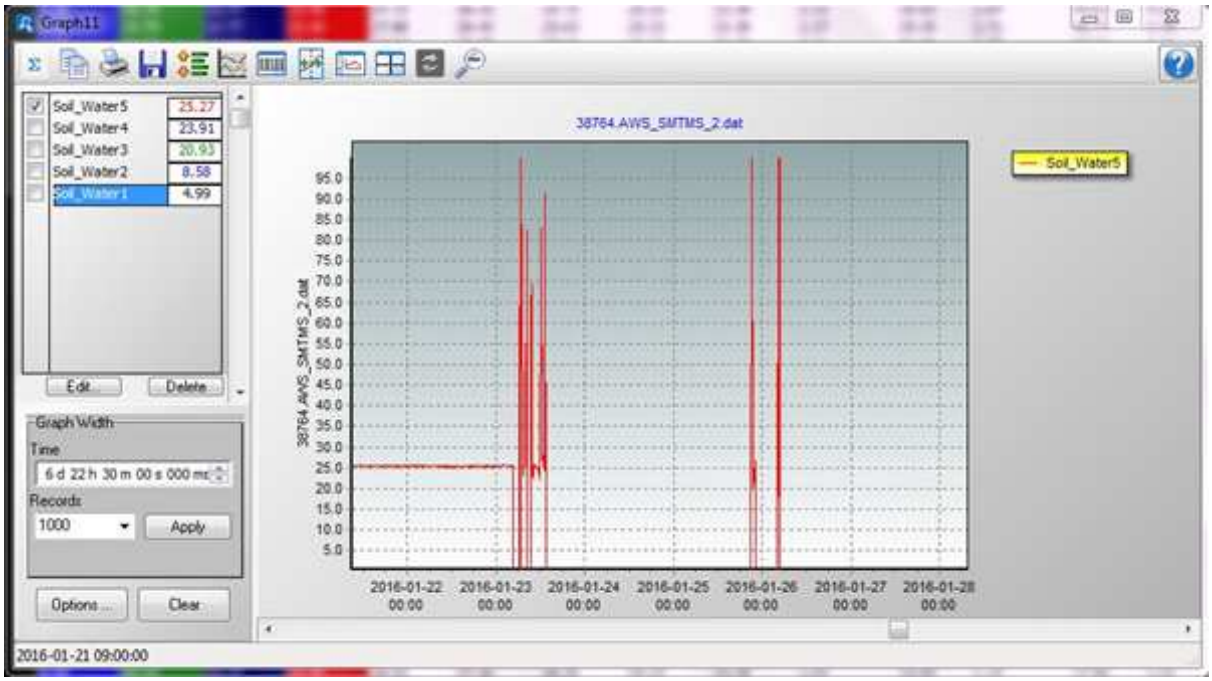

Figure 2.3: *Graph showing soil water data from January 2016 and displaying random fluctuations during daylight hours.*

problems being found, therefore it is recommended that the sensor should be replaced as soon as possible. This will be investigated during the next visit to the site.

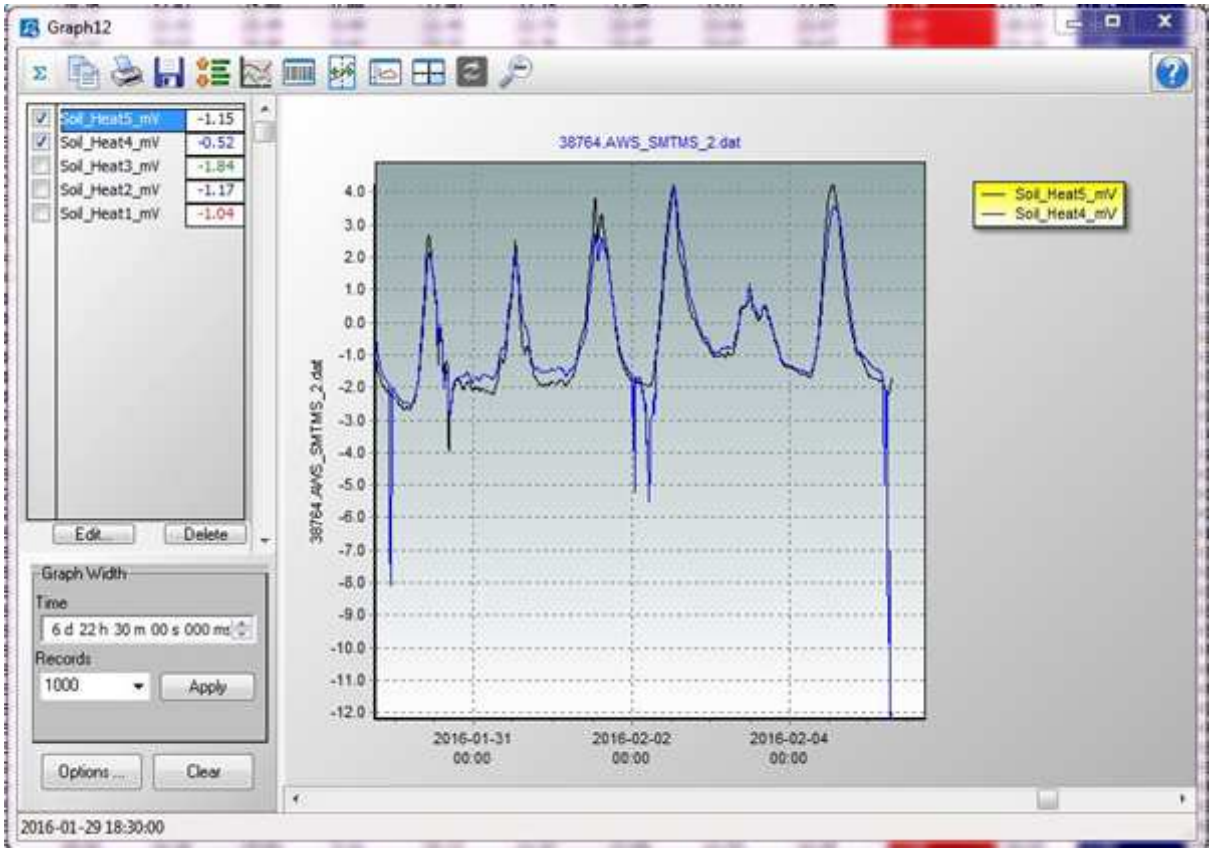

Figure 2.4: *Graph showing soil heat data from January 2016 and displaying random fluctuations during daylight hours.*

One of the heat flux plates has begun to show anomalous output spikes since late January 2016. The following screenshot illustrates the problem. HFP 4 (normal) and HFP 5 (faulty) are plotted on the same graph. Connections and wiring were checked and no problems were found. However, a failed heat flux plate still seems an unlikely scenario. During the next trip, a spare heat flux plate will be temporarily installed to see if the data spikes go away. The data could still be used provided outlying data spikes are manually edited out.

Chapter 3

On the impact of using representative stations for passive microwave soil moisture validation

3.1 Introduction

Due to the high spatial variability of soil moisture, it is important to understand the representativeness of measurements from soil moisture stations of the areal average prior to utilizing them in evaluating coarse-resolution soil moisture products. Previously i) long-term soil moisture measurements from the Yanco region of the OzNet Monitoring Network, ii) high resolution soil moisture measurements taken during three extensive field campaigns, and iii) airborne soil moisture products derived for the area were used to investigate the representativeness of stations within OzNet of Soil Moisture Active Passive (SMAP) soil moisture product grids. The methods employed to carry out this investigation included the temporal stability analysis, point to pixel comparisons, and the centered variogram analysis.

To address the issue of non-representativeness, and demonstrate the impact of poorly selected stations, validation of remote sensing soil moisture products are based on the careful selection of stations, as in (Yee et al., 2016). This also allows resources to be concentrated on representative stations. The most representative stations have been used to validate the AMSR-2 soil moisture products from two different versions of algorithms, developed by the Japan Aerospace eXploration Agency (JAXA) and the Land Parameter Retrieval Model (LPRM)

compared with the SMOS soil moisture product (L-band). This comprehensive comparison of different soil moisture products leads to 1) an understanding of how well each product meets their respective performance requirements under very controlled analysis, and 2) identification of the best performing product under the conditions of this site.

3.1.1 Study area and in-situ soil moisture data

This validation study was carried out for the Yanco site which is within the Murrumbidgee River catchment in New South Wales, Australia (Fig. 3.1).

The western side of the study area includes the Coleambally Irrigation Area (CIA), which consists of farms with a mix of flood irrigation and dryland cropping. Main crops grown during summer include rice, corn, and soybeans whereas wheat, oat, barley and canola are grown during winter. Flood irrigating of rice crops occur in November (Panciera et al., 2014). Conversely, land use to the eastern side consists of pastures for grazing. YA is used to describe the cropping area, and YB for the grazing area. There are 13 stations within the study area (denoted with the prefix 'Y-') equipped with vertically installed Stevens Water Hydraprobe (0-5 cm) and Campbell Scientific CS616 water reflectometers (0-30 cm, 30-60 cm, and 60-90 cm) to measure the profile soil moisture content at the sites; and 24 stations equipped with a Hydraprobe inserted vertically from the surface (0-5 cm) concentrated within the YA and YB area (denoted 'YA-' and 'YB-'). To compare as closely as possible with the depth sensed by the microwave sensors, only measurements from 0 - 5 cm have been used here (Adams et al., 2015). Average soil moisture based on station measurements was obtained by taking the average of available measurements from stations which fall within the satellite pixel at each time-step.

3.1.2 Satellite soil moisture data

AMSR-2

AMSR-2 on-board the GCOM-W1 satellite was launched in May 2012 as a follow-on of the Advanced Microwave Scanning Radiometer (AMSR, December 2002 to 2003) and AMSR for the EOS (AMSR-E, May 2002 to Oct 2011). Compared to AMSR/AMSR-E, AMSR-2 has a larger antenna (2.0 m diameter) than AMSR-E (1.6 m diameter). Compared to AMSR / AMSR-E, AMSR-2 has a larger antenna (2.0 m diameter) than AMSR-E (1.6 m diameter),

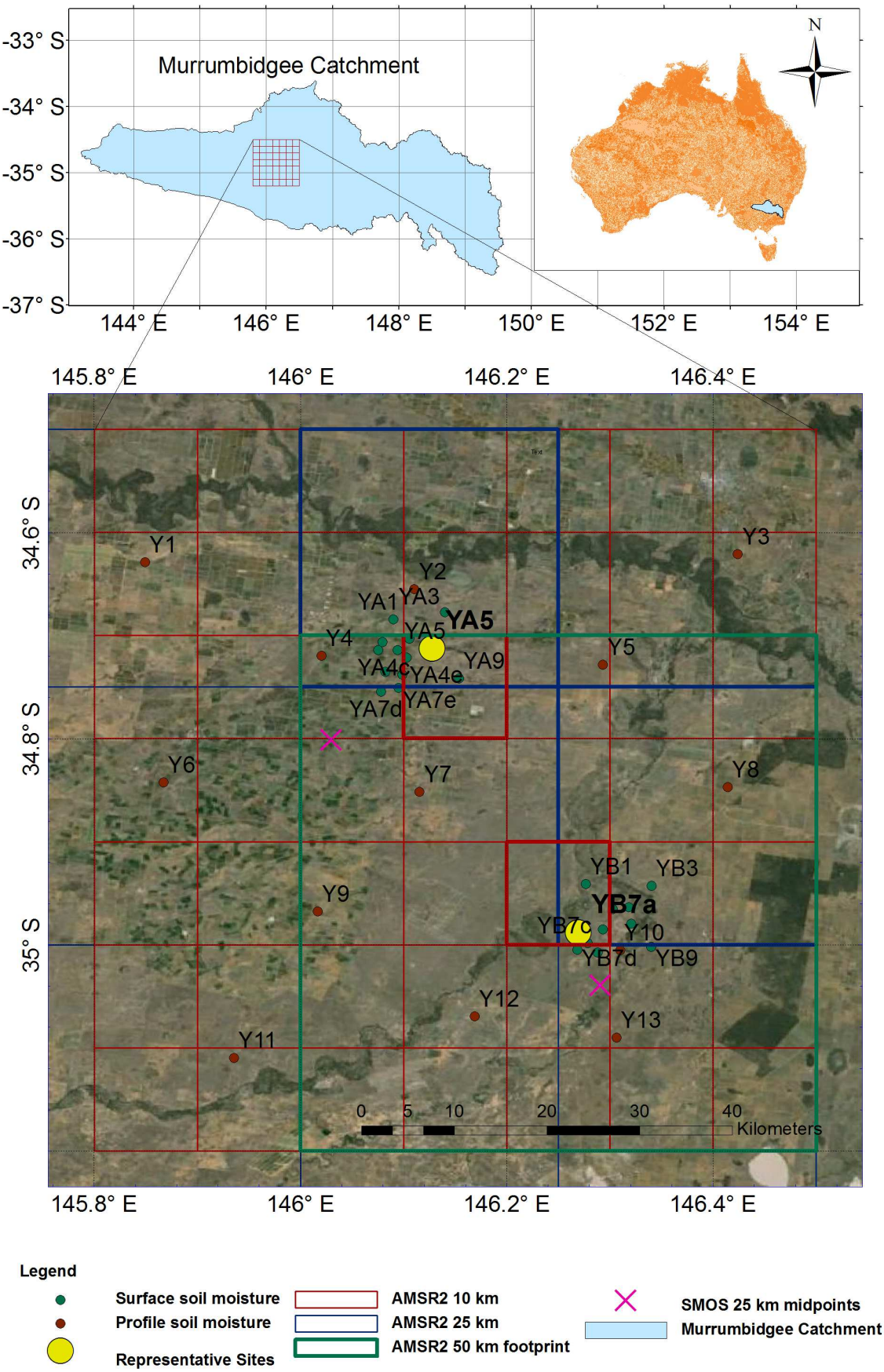

Figure 3.1: *Map of study area showing locations of most representative stations and satellite pixels selected for validation. Top left inset: Relative location of the study area within the Murrumbidgee catchment. Top right inset: Relative location of Murrumbidgee catchment within the Australian continent.*

an additional C-band (7.3 GHz) channel to mitigate RFI (e.g. de Nijs et al., 2015), and an improvement in calibration accuracy through a change in thermal design (Imaoka et al., 2010; Maeda et al., 2011). Observations from AMSR-2 are available twice (ascending/evening and descending/morning) every one to two days.

The two AMSR-2 products compared here are based on the JAXA (Fujii et al., 2009; Maeda and Taniguchi, 2013) and LPRM (Owe et al., 2001; Parinussa et al., 2015) algorithms. Due to an improvement in calibration of AMSR-2, both JAXA and LPRM products have been reprocessed. The JAXA AMSR-2 Level 3 soil moisture content products, version 1.11 (herein referred to as JX1) and version 2.21 (herein referred to as JX2), were obtained from the GCOM-W1 Data Providing Service (`https://gcom-w1.jaxa.jp/`). As JX1 was only available up till the end of 2014; and to obtain an equal number of seasons, soil moisture products from July 2012 to July 2014 were considered here.

As for the LPRM products, the former version (herein referred to as LP1) were obtained from Goddard Earth Sciences Data and Information Services Center (GES DISC) (`http://disc.sci.gsfc.nasa.gov/hydrology/`) whereas the updated version (herein referred to as LP2) were reprocessed following (Parinussa et al., 2015) and (Kim et al., 2015). The AMSR-2 products are available at 10 km and 25 km grid resolutions although its footprint is approximately 50 km. Hence, products of 10 km and 25 km were included in the analysis for both evening (1:30 pm) and morning (1:30 am) overpasses.

SMOS

Launched in 2009, the radiometer on-board SMOS measures L-band at 1.4 GHz every 3-days. Whilst the resolution of SMOS is approximately 40 km (Kerr et al., 2001), the soil moisture L3 products are provided at 25 km resolution. These products are derived based on the L-band microwave emission of the biosphere (L-MEB) model which involves an iterative algorithm to minimize a cost function computed from the differences between measured and modelled brightness temperature from all available incidence angles (Wigneron et al., 2007). The data used here were obtained from the Centre Aval de Traitement des Données SMOS (CATDS), operated for the Centre National d'Etudes Spatiales (CNES, France) by IFREMER (Brest, France) (Jacquette et al., 2010). The daily 25 km SMOS Level 3 products, both ascending/morning

(6:00 am) and descending /evening (6:00 pm), CATDS version 2.72 which is aligned with version 6.11 Level 2 products were used. Although night-time retrievals have generally been shown to be more accurate than day-time retrievals (e.g Al-Yaari et al., 2014; Njoku et al., 2003), recent studies have suggested that day-time retrievals are just as good (e.g. Rowlandson et al., 2012). Following Al-Yaari et al. (2014), instances when the soil moisture data quality index (DQX) was larger than 0.06 were removed. As the reanalysis soil moisture products (EASE grid) were only available for 2012 to 2013, the operational product was used for 2014 (EASE2 grid). For consistency, it is assumed here that the operational products are also on the EASE grid.

To differentiate the products, where applicable, AMSR-2 and SMOS products, have subscripts denoting the observed frequency used (X, C1 or C2), the overpass (M: morning, E: evening), and product resolution (10 or 25), whereas superscripts denote the area being validated (YA or YB). For instance, $JX1^{YA}_{X(M),25}$ is the 25 km soil moisture product based on the JAXA algorithm (version 1), derived based on observations at X-band during morning overpasses at the YA area.

3.1.3 Analysis

Based on results in Yee et al. (2016), incorrect conclusions and biases may be introduced into the results unless there is a good understanding of the sites. Therefore, coarse scale passive microwave remote sensing soil moisture products are validated here based on a careful understanding of the representativeness of stations within YA and YB area. Since stations within the Yanco area are well distributed, based on temporal stability methods, YA5 and YB7a were found to provide a good measure of the areal average of the YA and YB area ($\approx$ 9 km X 9 km), and YA5 for the Yanco region ($\approx$ 36 km X 36 km). It is assumed here that although results from the previous analysis focused on SMAP grids, they are transferable to the AMSR-2 25 km grids. Pixels with center points closest to these areas was selected for validation. As the native footprint of the satellites overlaps the adjacent pixels, the stations which fall around the pixels were also used to compute an average for the entire pixel.

Consistent with mission objectives, the statistical metrics which are used to evaluate the products include bias, root mean square difference (RMSD) (similar to RMSE), Pearson correlation coefficient (r), MAE and unbiased RMSD (ubRMSD). Bias was computed as the difference

in subtracting means of soil moisture based on the remote sensing products from means based on ground measurements. MAE is the average of the absolute errors, and differs from RMSD in that the squaring of the errors in RMSD gives a greater weight to larger errors.

Taylor diagrams are used to combine measures of r, standardized centered RMSD (cRMSD) and standardized standard deviation with ground soil moisture measurements (Taylor, 2001). Taylor diagrams provide a comprehensive visualization of how well two datasets relate to each other in terms of r, RMSD and their standard deviations. They have also recently been applied for soil moisture validation by Champagne et al. (2015). The geometric relationship between these statistics allows the Taylor diagram to be plotted. For N discrete points of two variables, f_n and g_n, r is given as:

$$r = \frac{\frac{1}{N}\sum_{n=1}^{N}(f_n - \overline{f})(g_n - \overline{g})}{\sigma_f \sigma_g} \tag{3.1}$$

where $\overline{f}$ and $\overline{g}$ are their means, and σ_f and σ_g are the standard deviations, of f and g respectively. The cRMSD, which is the unbiased RMSD (ubRMSD), is then given by

$$\text{cRMSD} = \sqrt{\frac{1}{N}\sum_{n=1}^{N}[(f_n - \overline{f})(g_n - \overline{g})]^2}. \tag{3.2}$$

The maximum soil moisture established in the JAXA algorithm is 0.60 m^3 m^{-3} whereas the LPRM algorithm is 1.00 m^3 m^{-3} (Kim et al., 2015). Therefore, assuming f_g is the reference dataset, these statistics were then further standardized by σ_g such that standardized cRMSD, $\hat{\text{RMSD}} = \text{cRMSD}/\sigma_g$, and standardized σ_f, $\hat{\sigma_f} = \sigma_f/\sigma_g$ (Albergel et al., 2012). Note that although this procedure was referred to as normalization in Taylor (2001), the term standardization is used here. Consequently, $\hat{\sigma_g} = 1$. Therefore, the radial distance of f_n from the origin, represents $\hat{\sigma_f}$, the distance radius from the origin represents $\hat{\text{RMSD}}$, and finally, the azimuthal position represents r between f_g and f_n. A more comprehensive description regarding the derivation and use of the Taylor diagram can be found in Taylor (2001).

As the general consensus within the remote sensing community is that morning observations are more ideal than during the day (referred to as evening here), as the difference in temperature between vegetation canopy and soil surface is minimum, the analysis here will firstly concentrate on morning observations and 25 km products. Comparisons with evening observations and 10

km products will only be introduced in latter sections.

3.2 Results and discussion

3.2.1 Representativeness

Table 3.1 and 3.2 summarizes the statistics from comparison of individual stations with satellite soil moisture products for each season within the YA and YB area respectively as Taylor diagrams. The red squares indicate the representative stations, green diamonds the average based on all stations, and blue circles all other individual stations. Generally, the closer a point is to the baseline (black point), the better its performance.

Table 3.1: *Taylor diagrams for 25 km morning products in the YB area. Satellite products are treated as the baseline soil moisture (black dot). □: Representative station. ◇: Average. ◯: Individual stations. Note the difference in scale for JAXA products.*

Product	Summer	Autumn	Winter	Spring
$JX1^{YA}_{X(M),25}$	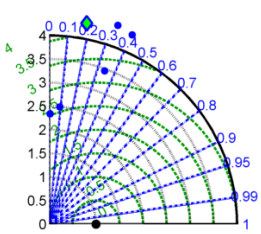	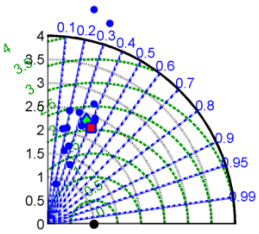	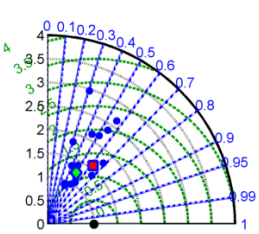	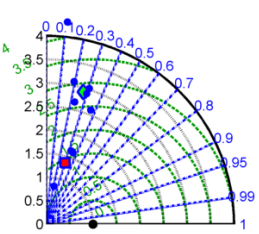
$JX2^{YA}_{X(M),25}$	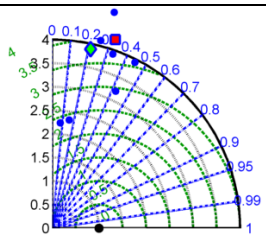	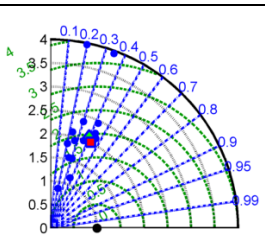	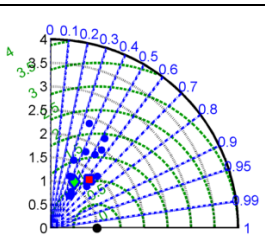	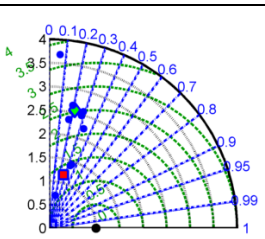
$LP1^{YA}_{X(M),25}$	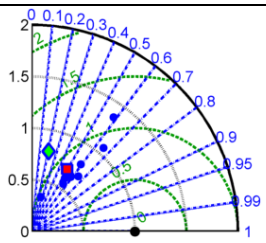	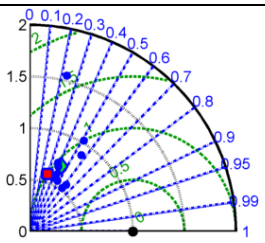	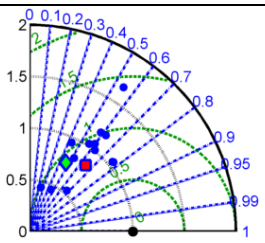	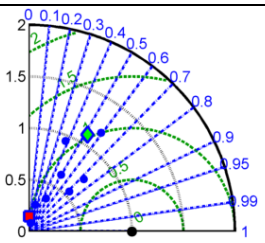

Continued on next page

Table 3.1 – continued from previous page

Product	Summer	Autumn	Winter	Spring
$LP1^{YA}_{C1(M),25}$	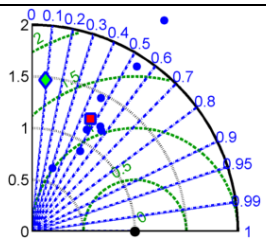	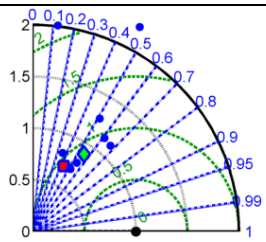	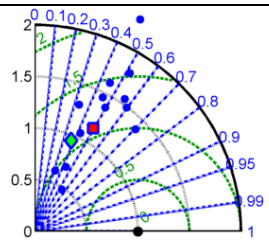	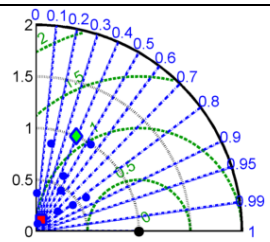
$LP1^{YA}_{C2(M),25}$	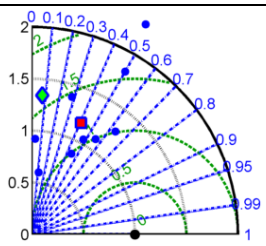	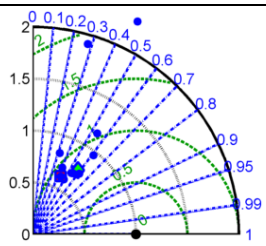	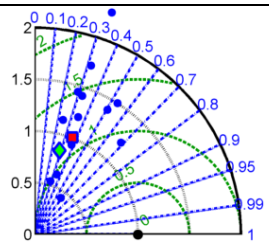	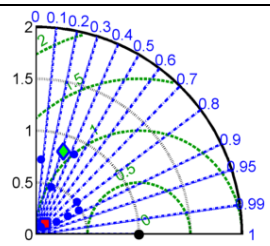
$LP2^{YA}_{C1(M),25}$	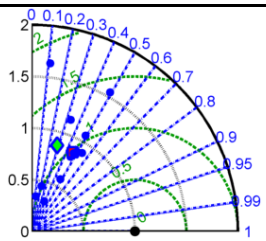	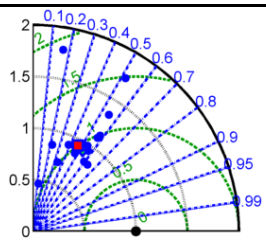	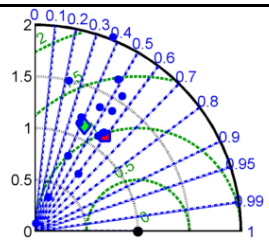	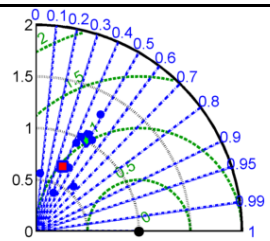
$LP2^{YA}_{X(M),25}$	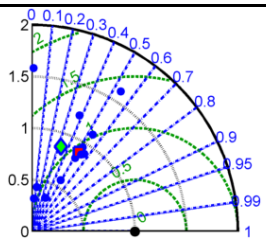	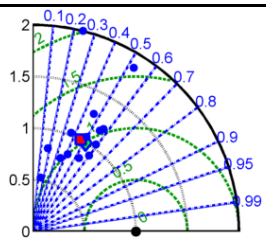	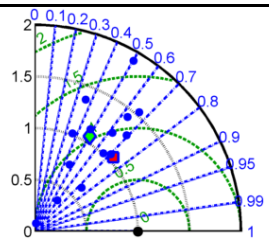	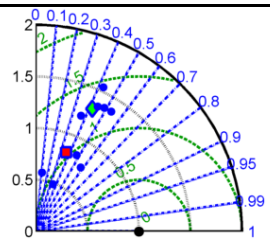
$LP2^{YA}_{C2(M),25}$	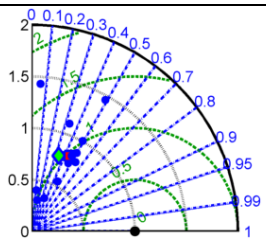	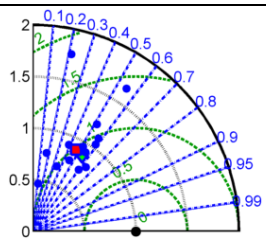	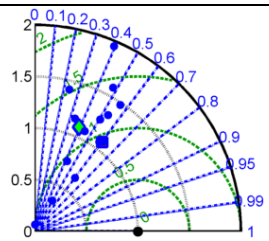	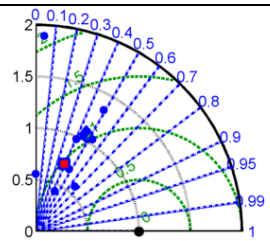
$SMOS^{YA}_{L(M),25}$	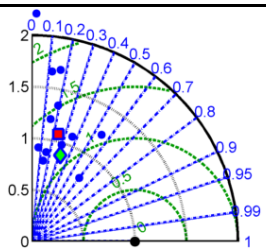	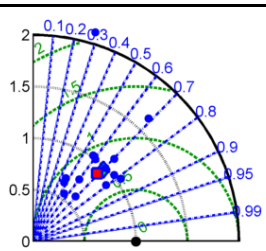	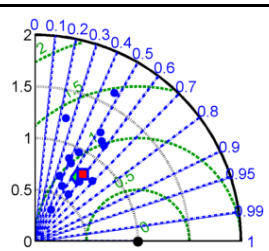	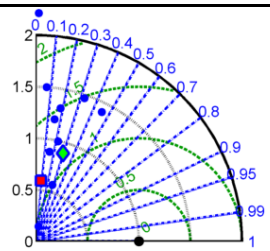

Table 3.2: *Taylor diagrams for 25 km morning products in the YB area. Satellite products are treated as the baseline soil moisture (black dot). □: Representative station. ◇: Average. ◯: Individual stations. Note the difference in scale for JAXA products.*

Product	Summer	Autumn	Winter	Spring
$JX1^{YB}_{X(M),25}$	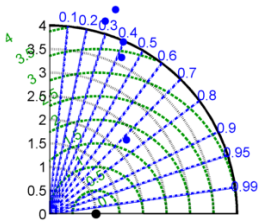	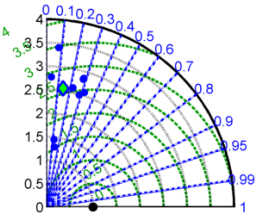	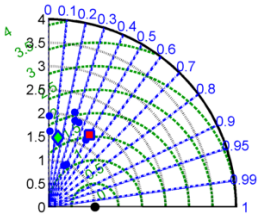	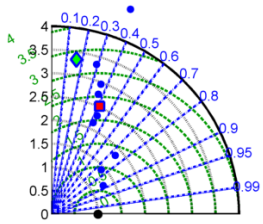
$JX2^{YB}_{X(M),25}$	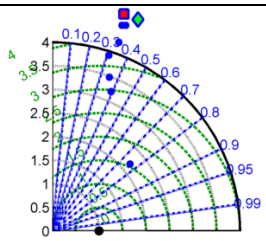	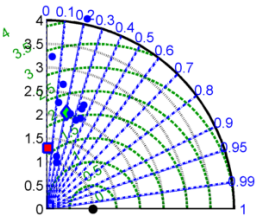	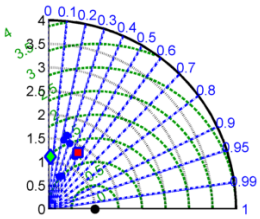	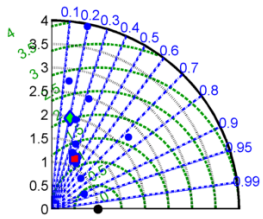
$LP1^{YB}_{X(M),25}$	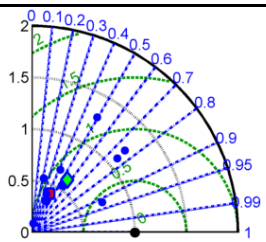	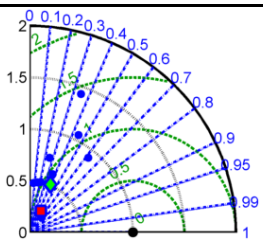	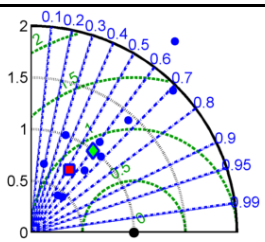	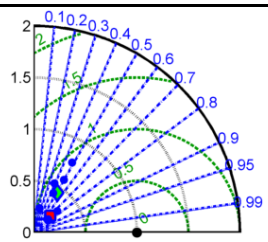
$LP1^{YB}_{C1(M),25}$	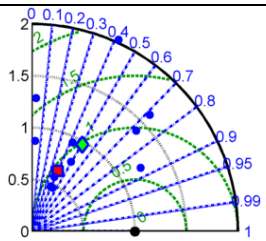	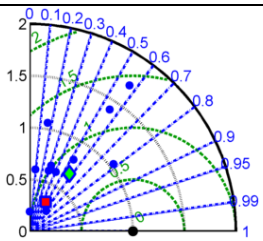	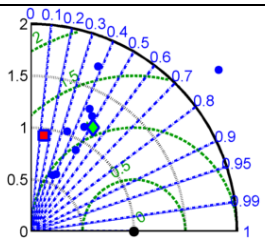	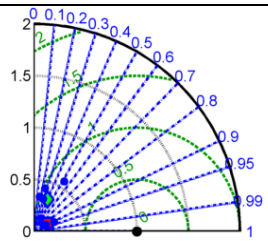
$LP1^{YB}_{C2(M),25}$	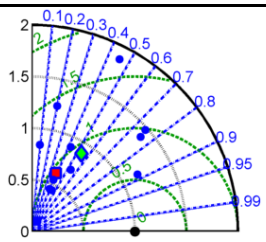	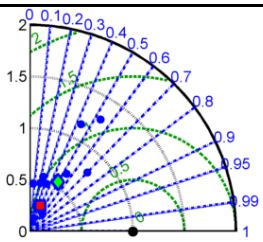	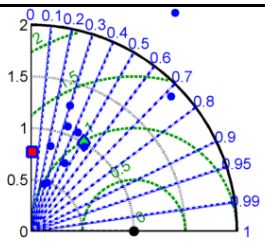	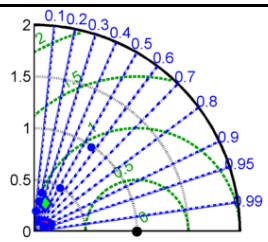
$LP2^{YB}_{X(M),25}$	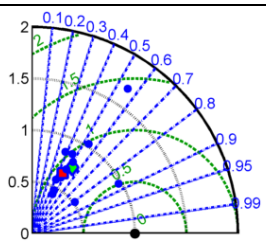	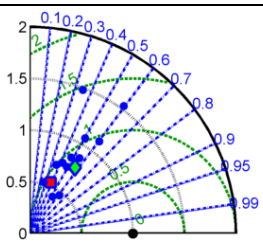	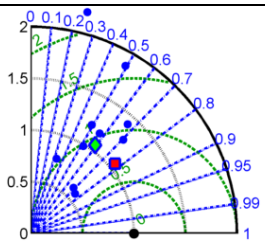	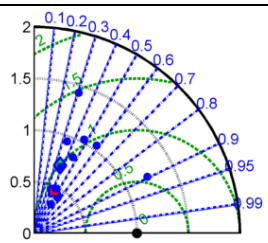

Continued on next page

Table 3.2 – continued from previous page

Product	Summer	Autumn	Winter	Spring
$LP2^{YB}_{C1(M),25}$	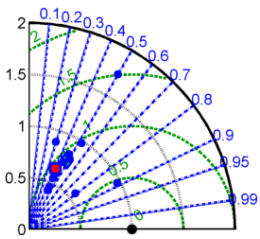	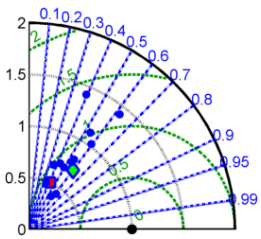	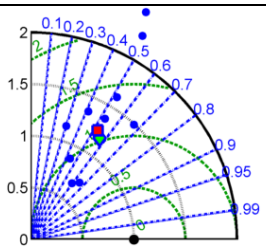	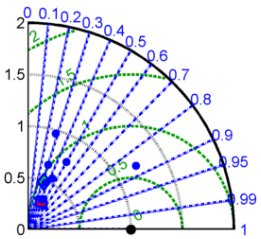
$LP2^{YB}_{C2(M),25}$	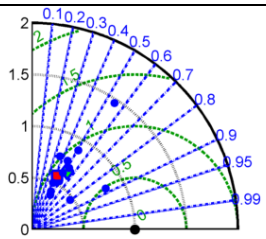	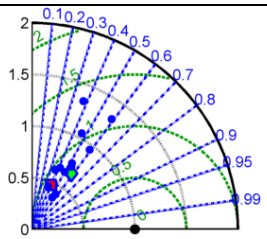	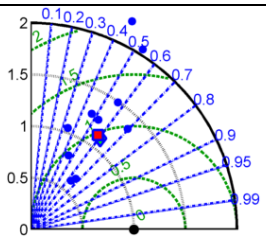	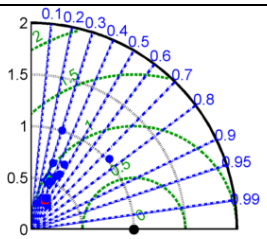
$SMOS^{YB}_{L(M),25}$	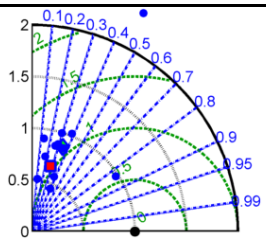	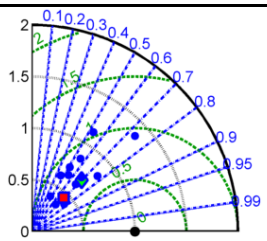	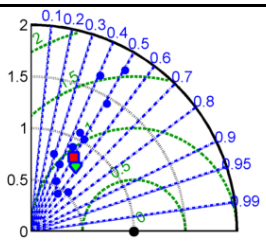	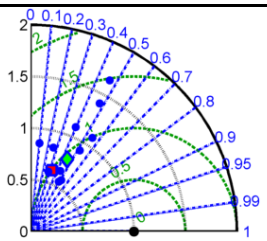

The scatter of blue dots within the Taylor diagrams for the YA area (Table 3.1), particularly during summer and winter, indicates that statistics differ depending on the stations used for validation. Some individual stations were found to have an r of < 0.1 (stations with $r < 0$ are not shown) or a cRMSD > 1.5 m^3 m^{-3}. Further investigation (not shown here) revealed that during summer and autumn, YA4b and YA4d recorded high soil moisture values (> 0.40 m^3 m^{-3}); likely due to irrigation. Individually, when compared to SMOS 25 km soil moisture products (morning overpasses), YA4b and YA4d had an overall r of 0.07 and -0.16, RMSD of 0.14 m^3 m^{-3} and 0.28 m^3 m^{-3}, and bias of 0.09 m^3 m^{-3} and 0.22 m^3 m^{-3} respectively. Other stations had an r ranging between 0.24 to 0.68, RMSD between 0.07 m^3 m^{-3} to 0.14 m^3 m^{-3}, and bias between 0 m^3 m^{-3} to 0.09 m^3 m^{-3}. Although each of these irrigated plots consist of approximately 0.10% of the entire 25 km pixel, they can have a large impact on the average soil moisture if not weighted appropriately.

In the case of the YB area, the scatter in r values (Table 3.2) is seen to be less apparent due to homogeneity of the area. In comparison to SMOS 25 km soil moisture products (morning

overpasses), r ranged between 0.53 to 0.73, RMSD 0.07 m^3 m^{-3} to 0.10 m^3 m^{-3}, and bias between 0.01 m^3 m^{-3} to 0.09 m^3 m^{-3}. As expected, r and RMSD between the average of all stations and the representative stations has similar results (as identification of the representative station was in large based on its ability to represent the mean), whereas a big variation can be found if a single station was used without prior knowledge of its representativeness. This also demonstrates that, whilst the absolute accuracy of a representative station is difficult to determine, by directing limited resources to most representative stations, similar results can be obtained as having a number of stations. Results here have shown the importance of understanding the representativeness of soil moisture stations prior to using them for validation. Ideally, if intensive data was available, the representativeness of stations within the AMSR-2 grid could be determined with better confidence. However, since this is not, the satellite soil moisture products will be validated based on the representative stations YA5 and YB7a for the YA and YB area respectively which was determined based on SMAP grids Yee et al. (2016) for the remainder of this study.

3.2.2 Overall performance

Based on comparison with the representative stations, there is a noticeable seasonal impact on the performance of absolute soil moisture based on JX1 and JX2 whereby cRMSD decreased sequentially from summer, autumn, spring and winter (Table 3.1 and 3.2). This was more consistent for LP1, LP2 and SMOS, cRMSD was ($\approx$ 1 throughout the year). The JAXA algorithm assumes that surface and canopy temperature is both equal and constant throughout the year at 295 K. Whilst canopy temperatures are not compared here, it is expected that this assumption would be valid only during winter. Consequently, cRMSD is lowest during winter and highest during summer.

Fig. 3.2 and 3.3 compares measurements from 25 km (morning) soil moisture products from JX1, JX2, LP1, LP2 and SMOS within the YA area with YA5, and within the YB area with YB7a. Generally, JX1 and JX2 underestimated soil moisture by $>$ 0.05 m^3 m^{-3} and had an r of approximately 0.5, while LP1 and LP2 overestimated (ranging from 0.04 m^3 m^{-3} to 0.20 m^3 m^{-3}), particularly when soil moisture conditions were $>$ 0.10 m^3 m^{-3}. Based on the scatterplots, it can be seen that the performance of the JAXA algorithm decreased with

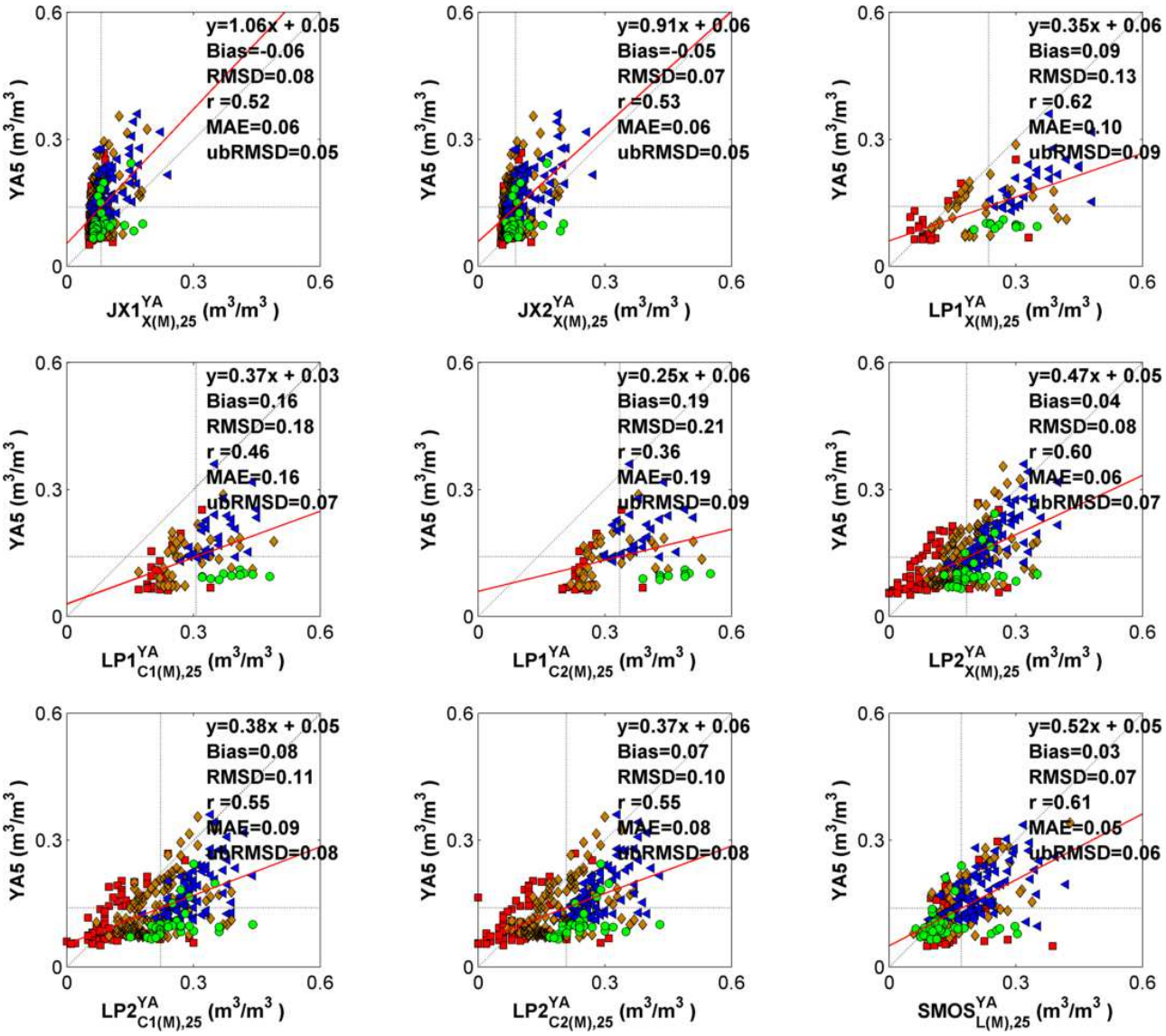

Figure 3.2: *Scatterplots comparing different soil moisture products (morning overpass) based on JX1, JX2, LP1, LP2, and SMOS soil moisture products in the a) YA area with YA5 (baseline). Summer: □ (Red), Autumn: ◇ (Orange), Winter: ◁: (Blue), Spring: ◯ (Green). Dotted horizontal and vertical lines indicate the means of the corresponding x- or y-axis variables, whereas the diagonal line is the 1:1 line.*

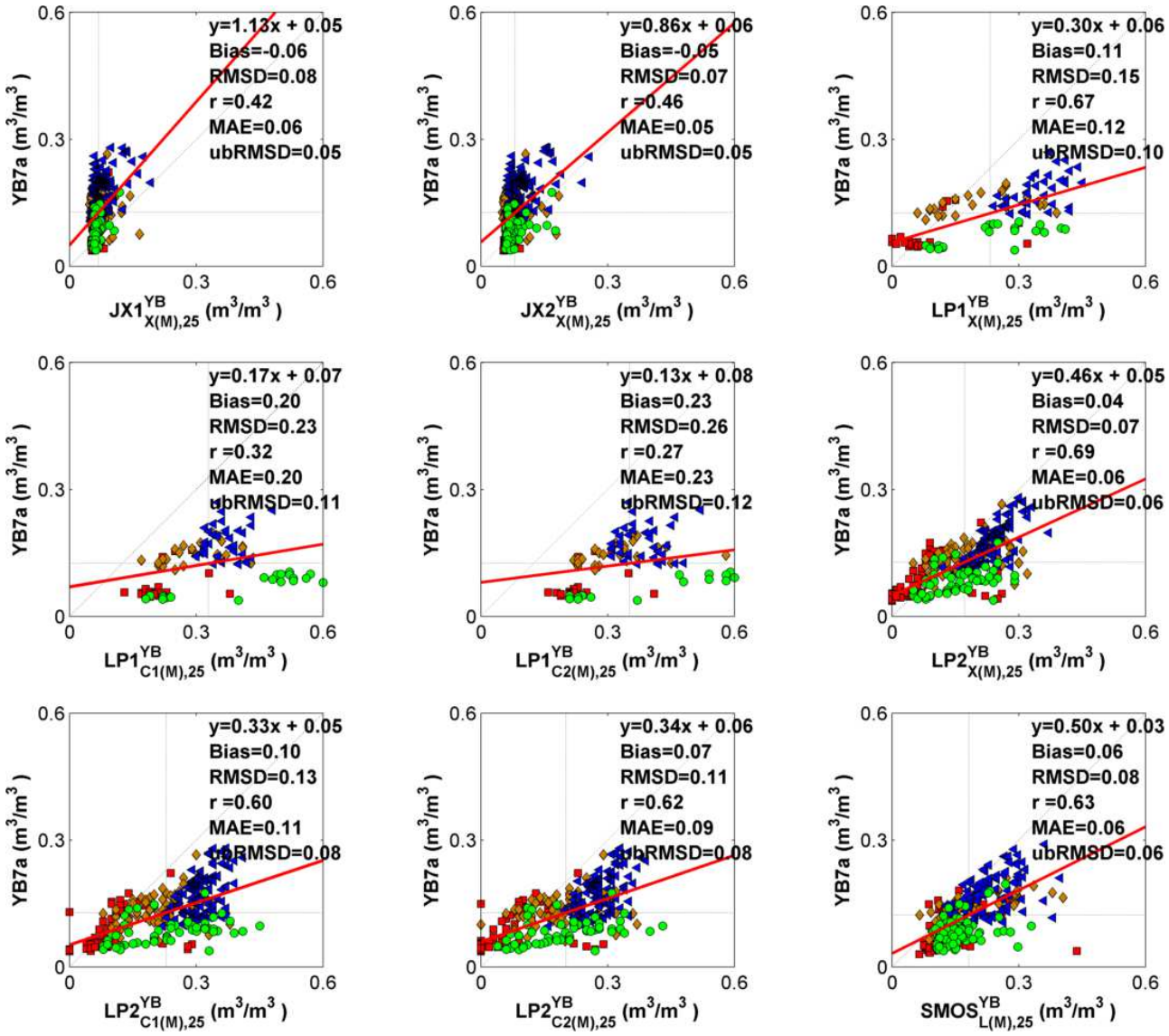

Figure 3.3: *Scatterplots comparing different soil moisture products (morning overpass) based on JX1, JX2, LP1, LP2, and SMOS soil moisture products in the YB area with YB7a (baseline). Summer: □ (Red), Autumn: ◇ (Orange), Winter: ◁: (Blue), Spring: ◯ (Green). Dotted horizontal and vertical lines indicate the means of the corresponding x- or y-axis variables, whereas the diagonal line is the 1:1 line.*

increasing soil moisture values whereas the opposite is true for LPRM. Kim et al. (2015) found similar results when comparing AMSR-2 soil moisture products based on the JAXA and LPRM algorithm globally. Only a slight improvement was observed in the latter version of the JAXA products (JX2) with a reduction of MAE from 0.06 m^3 m^{-3} to 0.05 m^3 m^{-3}. Whilst LP1 had a larger RMSD (0.13 - 0.23 m^3 m^{-3}) and MAE (0.10 - 0.20 m^3 m^{-3}) than JX1 and JX2, they decreased to 0.06‘ - 0.11 m^3 m^{-3} and 0.07 - 0.13 m^3 m^{-3} respectively in LP2. The correlation of C-band observations also increased to > 0.55 but did not change much for X-band observations (Fig. 3.2 and 3.3). SMOS is seen to slightly underestimate, agreeing with the findings of previous studies (Al Bitar et al., 2012; Collow et al., 2012; Su et al., 2013) but its slope was closer to 1 than that of LP2.

Generally, based on the scatter plots, the C-band observations based on LP1 did not meet the AMSR-2 mission objectives of achieving an MAE of less than ± 0.08 m^3 m^{-3}, whereas based on LP2, only C-band observations met the objectives at the YA and YB area. Likewise, RMSD of SMOS observations exceeded the mission requirements of 0.04 m^3 m^{-3} accuracy. However, in terms of MAE, SMOS satisfies the mission objective of AMSR-2. Yet, although JX1 and JX2 managed to meet their own mission objective, they had a lower overall r. As the latter products based on the JAXA and LPRM algorithm were found to be superior over the former versions, in the following analyses, only JX2, LP2 ('X-' and C-band) and SMOS are discussed in detail.

3.2.3 Overpass periods

Fig. 3.4 shows the time-series of morning (top) and evening (bottom) retrievals from JX2, LP2 and SMOS compared to station measurements for the YA area. The large variation in soil moisture measurements based on individual stations (gray lines) re-emphasizes the need for validation with most representative stations. Generally, it can be seen that soil moisture retrieved based on JX2 was the driest followed by SMOS, $LP2_X$, $LP2_{C2}$ and $LP2_{C1}$ for both morning and evening overpasses. The variation in soil moisture was also lower during evening overpasses. During July 2014 (Austral winter), there was a clear underestimation by JX2 with a more noticeable difference in morning retrievals rather than evening. Moreover, as LP2 and SMOS did not display this pattern, the underestimation is most likely due to the algorithm.

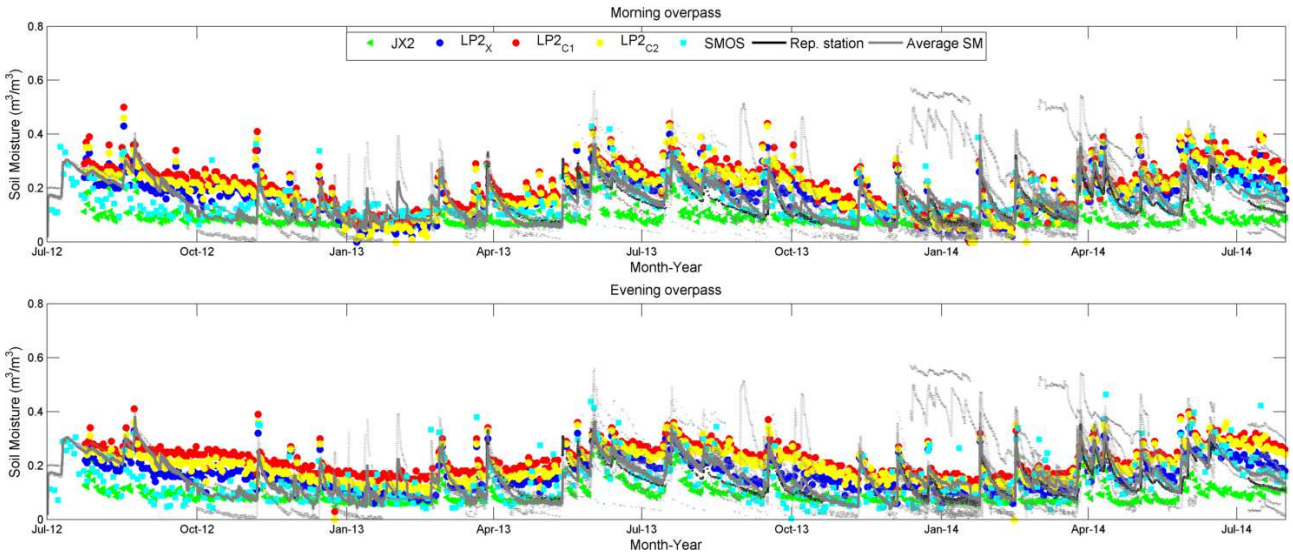

Figure 3.4: *Timeseries of morning (top) and evening (bottom) observations based on different 25 km satellite products from July 2012 to July 2014 for the YA area.*

Fig. 3.5 summarizes the performance of each product based on comparisons with the most representative stations. Both JX1 and JX2 showed the lowest variations whereby $\sigma_{\hat{JX1}}$ and $\sigma_{\hat{JX2}}$ ranged between 0.5 and 1. Correspondingly, this led to the underestimation observed earlier and its cRMSD was the lowest in all cases.

$LP1_X$ showed the largest variation in all cases with $\sigma_{\hat{LP1_X}} > 1.5$ in most cases. In cases where $LP1_{C1}$ and $LP1_{C2}$ had a positive correlation, r was still the lowest among other products with C2 (7.3 GHz) performing worse than C1 (6.9 GHz). In the case of LP2, $LP2_{C2}$ performed only slightly better than $LP2_{C1}$ and $LP2_X$ performed the best. Theoretically, one would expect retrievals based on observations at 6.9 GHz (C1) to correlate better with the 5 cm soil moisture measurements since the depth sensed at lower frequencies should correspond more closely with the 5 cm depth of soil moisture probes and be less affected by the vegetation. However, results showed 10.7 GHz performed better than 6.9 GHz which overestimated and had a larger variance compared to the station measurements. This is in-line with the findings of Owe et al. (2008) and Draper et al. (2009) who found little differences between X- and C-band retrievals in Australia. Moreover, based on probability of RFI provided by the SMOS product, the percentage of RFI detected in the Yanco study area was negligible (at most 1.5%) and Njoku et al. (2005) previously found very little RFI in X-band over Australia. Consequently, it is postulated that most AMSR-based studies have concentrated on the development of the higher frequencies, and thus the algorithms have been calibrated to match X-band due to widespread occurrence of

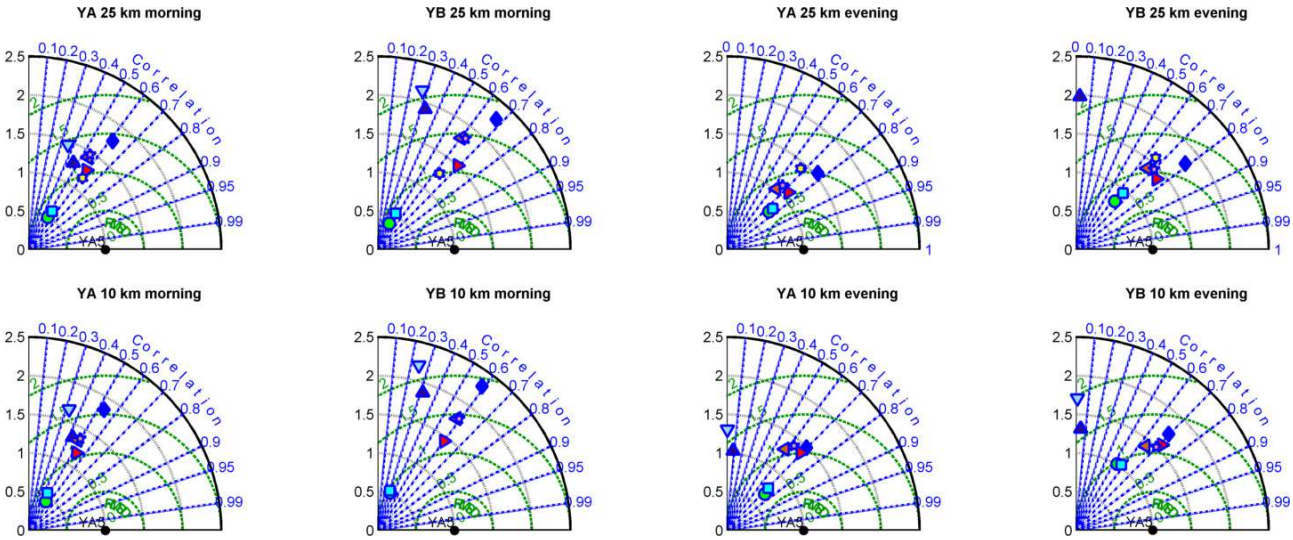

Figure 3.5: *Taylor diagrams comparing 25 km (top) and 10 km (bottom) morning and evening products for the YA and YB area. Green: JX1. Cyan: JX2. Blue: LP1$_{\mathrm{X}}$. Purple: LP1$_{\mathrm{C1}}$. Light blue: LP1$_{\mathrm{C2}}$. Red: LP2$_{\mathrm{X}}$. Orange: LP2$_{\mathrm{C1}}$. Peach: LP2$_{\mathrm{C2}}$. Yellow: SMOS. Note: SMOS products at 10 km resolution is not available.*

RFI at C-band in North America, Europe and East Asia.

In addition, evening overpass (1:30 pm) products were found to perform better for both the LPRM and JAXA algorithm than the morning passes (1:30 am). Moreover, the variation of soil moisture based on the evening overpasses matches better with that of the stations ($\hat{\sigma_f}$ closer to 1) than morning overpasses. Due to the negative r for 25 km evening retrievals based on LP1$_{\mathrm{C1}}$ and LP1$_{\mathrm{C2}}$, they were not shown on the diagrams. SMOS showed a more consistent performance for both evening and morning retrievals (cRMSD $\approx$1, $0.6 < \mathrm{r} < 0.7$, $\hat{\sigma_f} < 1.5$).

3.2.4 Resolutions

Moving down from 25 km to 10 km resolution, there was a very slight change in cRMSD (radial distance from baseline) due to homogeneity of the area (Fig. 3.5). Similarly, Champagne et al. (2015) emphasized that non-representativeness of stations at the coarser scale may be more important than the impact of land cover on soil moisture retrievals. Fig. 3.6 compares the morning and evening retrievals based on an assumed 50 km footprint product. The 10 km AMSR-2 product located within the centre of the Yanco study area was used here. As SMOS does not have a 10 km product, the 25 km product which was closest to the centre of the study area was selected. These retrievals were then validated based on measurement from YA5, as this station was found to be most representative of the regional Yanco study area in Yee et al.

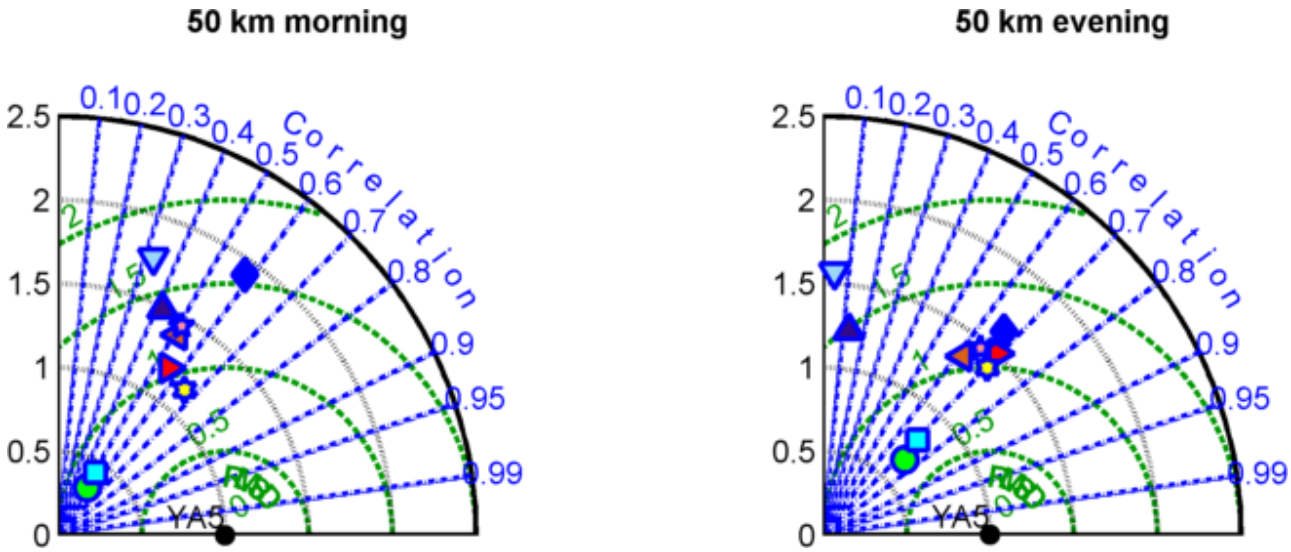

Figure 3.6: *Taylor diagrams comparing 50 km ascending and descending products for the Yanco area. Green: JX1. Cyan: JX2. Blue: LP1$_{\mathrm{X}}$. Purple: LP1$_{\mathrm{C1}}$. Light blue: LP1$_{\mathrm{C2}}$. Red: LP2$_{\mathrm{X}}$. Orange: LP2$_{\mathrm{C1}}$. Peach: LP2$_{\mathrm{C2}}$. Yellow: SMOS.*

(2016). According to the Taylor diagrams, SMOS and JX2 performed the best overall during morning and evening overpasses respectively. Nevertheless, r remained the same for JX1, JX2 and SMOS at the different resolutions. This backs the assumption that measurements from YA5 and YB7a are representative of the wider spatial footprint observed by the space-borne sensors.

3.3 Conclusion

This study validated AMSR-2 soil moisture products from two different versions of two different algorithms (JAXA and LPRM), and the SMOS soil moisture product using the most representative stations identified by an earlier study. It was shown that the use of unrepresentative stations can have a large impact on validation results (r of -0.16 as opposed to 0.61) particularly for non-homogeneous areas. Therefore, it is paramount that representativeness of stations be well understood prior to use for any validation purposes. While the absolute accuracy of a representative station is difficult to determine, having a representative station enables the reduction of resources needed to maintain a network of stations whilst providing consistent reliable data.

Generally, the later versions of the JAXA (JX2) and LPRM (LP2) products were confirmed to be superior over the former ones. Furthermore, JAXA products were found to underestimate

the soil moisture by ≈ 0.05 m^3 m^{-3} whereas LPRM products overestimated by between 0.04 - 0.20 m^3 m^{-3}. LP1 C-band observations performed badly with negative correlations and therefore should not be used. This is likely an effect of model miscalibration which was rectified in LP2.

Performance of soil moisture products during different seasons revealed varying performance of JAXA products, possibly due to assumptions that the difference in temperature between the soil surface and canopy is constant throughout the year. In the case of LP2, X-band retrievals performed better than C-band. Similarly, evening retrievals at X-band from AMSR-2 performed better than morning retrievals, whereas performance for both morning and evening retrievals was consistent for SMOS. Overall, JX2, LP2$_X$ and SMOS met the "goal accuracy" of ± 0.08 m^3 m^{-3} with an MAE of 0.05 m^3 m^{-3}, but none of the products achieved SMOS's goal of achieving an RMSD < 0.04 m^3 m^{-3}. Whilst SMOS performed the best based on morning retrievals (RMSD: 0.07 m^3 m^{-3}; r: 0.62), and LP2$_X$ performed best based on evening retrievals (RMSD: 0.06 m^3 m^{-3}; r: 0.74), JX2 evening products were just as good (RMSD: 0.06 m^3 m^{-3}; r: 0.70).

Consequently, depending on the interest of the user of the products, different soil moisture products should be applied. If soil moisture is used as an indicator of wetness condition, i.e. the ability to capture temporal variability is prioritized, LP2$_X$ evening overpasses are recommended for use. However, where accuracy in absolute soil moisture is needed, SMOS retrievals are recommended due to its ability to capture both the temporal and absolute variability of soil moisture for both morning and evening observations with the same confidence. Finally, these results need to be considered in the light that this study focuses on two carefully selected pixels and may not reflect the product accuracy at other sites. Therefore, it is important that such careful analysis can be conducted at other sites.

Chapter 4

Evaluation of MTSAT-1R evapotranspiration product with eddy covariance systems

4.1 Introduction

This study evaluates the Multi-functional Transport SATellites (MTSAT) evapotranspiration (ET) products of Ershadi et al. (2014) and McCabe et al. (2015) based on a combination-type method (the three-source Penman-Monteith model; PM-Mu developed by Mu et al., 2011), and a radiation-based technique (the modified Priestley-Taylor model; PT-JPL, Fisher et al., 2008).

The most popular approach adopted to validate remote sensing surface heat fluxes is based on the eddy covariance (EC) method (Kaimal and Finnigan, 1994), with EC systems deployed globally through the FLUXNET network (Baldocchi et al., 2001; El Maayar et al., 2008). However, two of the inherent problems of satellite validation with EC systems are i) the differences in spatial scale of the EC system's footprint and the scale which is sensed by the space borne sensor, and ii) the inability of EC systems to close the energy balance. As the footprint of EC systems changes with meteorological conditions, its representativeness of coarse scale satellite products, particularly in a heterogeneous landscape, is debatable (Ward et al., 2014).

Scintillometry presents an alternative method, as it is able to measure path integrated fluxes ranging from a few hundred meters to 10 km, i.e. equivalent to a satellite pixel (Baghdadi et al.,

2007; Beyrich et al., 2002; Meijninger and De Bruin, 2000; Samain et al., 2012b). They have been shown to perform well in the estimation of surface heat fluxes over different types of landscapes (e.g. Brunsell et al., 2011; Chehbouni et al., 2000; Ezzahar et al., 2009; Lagouarde et al., 2002; Liu et al., 2013; McJannet et al., 2011; Pauwels et al., 2008; Samain et al., 2012a, 2011; Savage, 2009; Yee et al., 2015; Zeweldi et al., 2010), including open water and urban areas (Lagouarde et al., 2006; McJannet et al., 2013; Samain et al., 2011; Ward et al., 2013). However, whilst scintillometry presents an alternative to measuring area averaged surface heat fluxes equivalent to a satellite pixel, considering the complexity involved in its operation and interpretation of its measurements, and the availability of EC measurements globally, it is desirable for EC systems to continue to be used for the long-term validation of satellite retrieved surface heat flux products.

Following the issues described above, this study attempts to validate remote sensing ET products by combining the strength of EC systems (i.e. more established and available method) and scintillometry (i.e. area averaged and consistent with satellite pixel). The focus of this study is firstly to understand how well the measurements derived from EC systems truly represent fluxes observed by the space-borne sensors (regional) in the study area. The hypothesis is that the study area is ideal due to its homogeneity, such that measurements from the EC tower are similar to fluxes within a satellite pixel and thus, its measurements can be used for long-term validation of remotely sensed surface flux products. To verify the homogeneity of the site, a field campaign was carried out whereby four scintillometers were placed across different locations within a single satellite pixel where an EC system has been established. If the location of the EC system is representative of the satellite pixel, regardless of the wind-direction, and therefore footprint of the scintillometers or EC tower, differences between the scintillometers and EC tower should be within the order of magnitude of errors associated with differences in measurement techniques (i.e. scintillometers and EC tower according to the results in (Yee et al., 2015). Following this, hourly 4 km resolution actual ET products derived based on the SEBS, PM-Mu, and PT-JPL models were validated using measurements from the EC system.

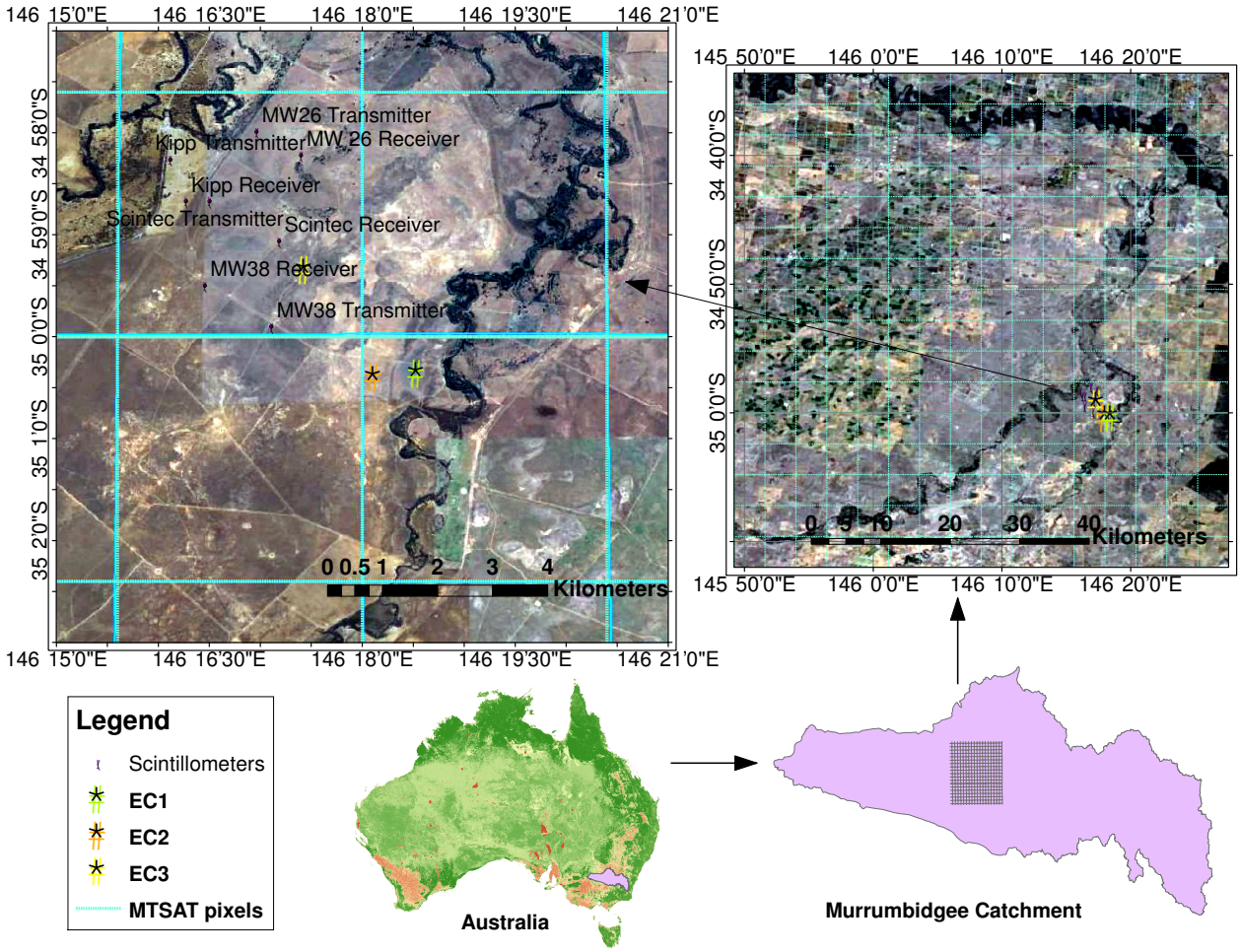

Figure 4.1: *Top left: Location of EC stations (EC1, EC2 and EC3) and scintillometers within the satellite pixel of interest and adjacent pixels. Top right: Yanco study area overlaid with 4 km MTSAT pixels.*

4.2 Site description and field measurements

The satellite pixel of interest is located within the Yanco Study Area (Fig. 4.1, top left pixel). It is situated within the center of the Murrumbidgee River catchment, in New South Wales, Australia (Smith et al., 2012). Perennial grasses cover a majority of the study area which is used for cattle grazing. Mean 3 pm temperature varies between 32.1°C in January to 13.5°C in July whereas majority of the 418.5 mm annual rainfall occur during winter and late autumn (Bureau of Meteorology station ID. 074037). The dominant wind directions are from the south-west and north-east (Fig. 4.2). Soil at the site is sand over clay (loamy sand) which has a typical porosity of about 0.30 m^3 m^{-3} (Hornbuckle et al., 1999; Smith et al., 2012).

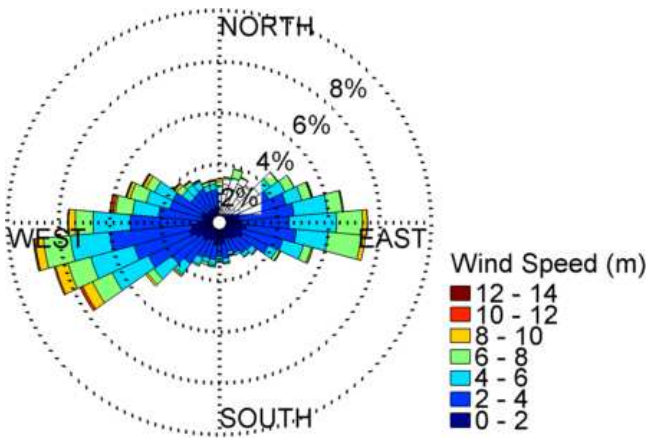

Figure 4.2: *Windrose showing wind direction and speeds during experimental period.*

4.3 Methodology and Data

4.3.1 Methodology

Scintillometers were placed in different locations within the 4 km × 4 km MTSAT pixel as shown in Fig. 4.1. Measurements from the scintillometers were then compared with those from the EC systems to understand how representative the tower is of the entire pixel. On the basis that this location is representative, and therefore ideal for satellite product validation due to its homogeneity, the ET products for that pixel was validated against EC measurements. However, as the EC system was only commissioned in May 2012 (from this point on-wards referred to as EC3), and the remote sensing ET products available to this study only extended up to May 2013, the length of EC record used to validate the ET product was extended by using measurements from EC stations set up close to EC3; from the 21st of November 2009 to the 20th of October 2010, and from the 2nd of May 2011 to the 11th of April 2012 (from this point onwards referred to as EC1 and EC2 respectively). EC1 and EC2 were located ∼100 m and ∼730 m south-west of EC3 respectively (Fig. 4.1).

4.3.2 Scintillometer measurements

Scintillometers of two different optical (LAS) manufacturers, Kipp and Zonen and Scintec (herein referred to as Kipp and Scintec, respectively), two microwave scintillometers (MWS) with a frequency, f, of 26 GHz and 38 GHz (herein referred to as MW26 and MW38, respectively) and two polarizations (horizontal, h and vertical, v) were used in this study. Due to

instrument maintenance, Kipp and MW26 were installed on the 21st of September 2014 whereas MW38 was installed on the 21st of December 2014, and the Scintec on the 6th of February 2015. Therefore, the data which has been used for this study was from the 21st of September 2014 (start of spring) up to 15th June 2015 (start of winter). The locations in which each scintillometer pair were located are shown in Fig. 4.1. Location, height, measurement periods and distances of the scintillometer receivers from their transmitters are also summarized in Table 4.1. The steps which were taken to derive the surface heat fluxes are similar to that in Yee et al. (2015).

Table 4.1: *ET datasets used where start and end indicates the period used in this study. T: Transmitter. R: Receiver.*

Name	T/R?	Lat(^{o})	Lon(^{o})	Distance(m)	Height(m)	Start	End
Kipp	T	34.971	146.269	800	2.95	19-Sep-14	15-Jun-16
	R	34.978	146.271				
MW26	T	34.967	146.283	792	2.73	19-Sep-14	15-Jun-16
	R	34.970	146.290				
Scintec	T	34.978	146.275	1267	2.68	6-Feb-15	15-Jun-16
	R	35.006	146.286				
MW38	T	34.998	146.285	1240	2.71	21-Dec-15	15-Jun-16
	R	34.992	146.274				
EC1	-	35.006	146.309	-	3.00	21-Nov-09	20-Oct-10
EC2	-	34.711	146.099	-	3.00	2-May-11	11-Apr-12
EC3	-	34.989	146.291	-	6.00	1-Jun-12	current
ET data	-			4 km X 4 km	-	1-Jan-10	1-May-13

Only daytime data were used for comparisons between scintillometers and EC3, only daytime data, defined as times when the Monin-Obukhov length (L_{Ob} [m]) derived from the EC system was negative (i.e. unstable conditions). Measurements of wind speed and direction, air temperature, pressure, humidity and precipitation from a weather station installed next to Kipp were used to derive surface heat fluxes from the scintillometers as described in Yee et al. (2015) with an assumed vegetation height of 0.3 m. Measurements taken between 30-min before and after a rainfall event were not considered.

4.3.3 EC measurements

For validation of the remote sensing ET products, all three EC systems used for comparisons consisted of a CSAT3 3-D sonic anemometer (Campbell Scientific, Inc.) and an open path

infrared gas analyzer (IRGA) (LI-COR Inc., U.S.) with a sampling frequency of 10 Hz following the general approach of Beringer et al. (2007) and Hutley et al. (2005). Fluxes were then computed and averaged at 30-min intervals. EC1 (-35.00^o, 146.31^o, 21st of November 2009 to the 10th of October 2010) and EC2 (-35.00^o, 146.30^o, 25th of May 2011 to the 11th of April 2012) were elevated ∼3 m above the ground, giving a fetch of about 300 m. EC3 is the flux tower funded by JAXA whereby the EC system was installed at a height of 6 m. As 10 Hz data were available for EC2 and EC3, they were processed using the software EddyPro (version 5.2.1) to calculate average fluxes at 30-min intervals. Corrections and processing implemented included spike detection and removal, lag correction relative to the vertical wind component based on covariance maximization method, linear de-trending, sonic virtual temperature correction, coordinate rotation using the double rotation method, spectral corrections for low and high pass filtering effects (Moncrieff et al., 2005) and the Webb-Pearman-Leuning correction (Webb et al., 1980). As 10 Hz data were not available for EC1, the 30-min fluxes computed within the logger program were corrected based on Webb-Pearman-Leuning correction (Webb et al., 1980) and used for comparisons with ET derived from the remote sensing models.

Following Ershadi et al. (2014), only daytime measurements from EC systems were used for comparisons with the models. This was defined based on downward short-wave radiation measured at the site whereby measurements were only used when net radiation (R_n) was greater than 20 W m^{-2}. Measurements were also removed during rain events and when H or $L_\mathrm{v}E$ was less than 0 W m^{-2}. All three stations were equipped with weather stations which included sensors for measuring incoming and outgoing radiation for the derivation of R_n, and soil heat and moisture properties for the derivation of ground heat flux (G) and precipitation. Measurements and processing of R_n and G were as in Yee et al. (2015).

4.3.4 MTSAT ET product

Forcing data

The MTSAT ET products based on SEBS, PM-Mu and the PT-JPL models have been derived and validated from January 2010 to the end of May 2013. The models were forced with short- and long-wave downward radiation, wind speed, air temperature, humidity and atmospheric pressure from Australian Community Climate Earth System Simulator - Australia (ACCESS-

Table 4.2: *Input data required for each model and their sources.*

Variables	Source	SEBS	PM-Mu	PT-JPL
Incoming short & long wave radiations	ACCESS	x	x	x
Wind-speed	ACCESS	x		
Air Temperature	ACCESS	x	x	x
Humidity	ACCESS	x	x	x
Atmospheric Pressure	ACCESS	x	x	x
NDVI	MODIS	x	x	x
LAI	derived from NDVI	x	x	
Emissivity	derived from NDVI	x	x	x
FPAR	derived from NDVI	x	x	x
Albedo	derived from NDVI	x	x	x
Land surface temperature	MTSAT	x		
Cloud mask	MTSAT	x		

A). ACCESS-A is the Australian operational numerical weather prediction (NWP) system which provides hourly meteorological data at a resolution of 12 km (Table 4.2).

Additionally, Normalized Difference Vegetation Index (NDVI) from MODIS (temporal resolution of 16 days at 250 m scales) (MOD13Q1 product) was interpolated and used as an input in the models and to derive Leaf Area Index (LAI), emissivity, Fraction of Photosynthetically Active Radiation (FPAR) and albedo. Refer to Ershadi et al. (2014) for more details on the interpolation and conversion. These vegetation parameters are important for the parameterization of roughness parameters (SEBS), aerodynamic and surface resistance parameters (PM-Mu) and constraint functions (PT-JPL). Finally, land surface temperature (LST) and cloud mask (4 km) from MTSAT were also used (Table 4.2). These products were derived based on previous work done of Ershadi et al. (2014) and McCabe et al. (2015).

The Surface Energy Balance System (SEBS)

SEBS is a physically based model which calculates surface heat fluxes based on information regarding the land surface, atmospheric conditions and vegetation information (Table 4.2). SEBS provides formulations to estimate roughness parameters using NDVI. Following this, based on temperature gradient, wind speed and roughness parameters, SEBS estimates H for dry and wet conditions using either MOST or the Bulk Atmospheric Similarity Theory equations to derive H based on relative evaporation. $L_{\mathrm{v}}E$ is finally derived as a residual term of the energy balance equation. The accuracy of SEBS is very much dependent on the accuracy of R_{n}, LST,

air temperature, humidity, wind speed and vegetation phenology used in the model (Ershadi et al., 2014; McCabe et al., 2015; Su, 2002). Generally, SEBS has been found to overestimate evaporation except where short canopies exist, such as grasslands and cropland. Refer to Su (2002) for a comprehensive description of the model formulation.

Three-source Penman Monteith (PM-Mu)

PM-Mu is a physical model based on the Penman-Monteith equation (Monteith, 1965). The version used to retrieve the ET products here is a three source model whereby total evaporation comes from evaporation of water intercepted by the canopy ($L_{\mathrm{v}}E_{\mathrm{i}}$), canopy transpiration ($L_{\mathrm{v}}E_{\mathrm{c}}$) and soil evaporation ($L_{\mathrm{v}}E_{\mathrm{s}}$). Evaporation from each component was derived based on the Penman Monteith equation but weighted based on fractional vegetation cover (determined based on FPAR), relative surface wetness (based on relative humidity, Fisher et al., 2008), and available energy. In the PM-Mu model, the often difficult to obtain or measure aerodynamic and surface resistance parameters are based on biome specific parameters from a Biome Properties Look up Table. Leaf scale parameters are extended to the canopy scale using meteorological information such as R_{n}, air temperature, humidity, pressure and vegetation phenology (FPAR, NDVI and LAI) as in Ershadi et al. (2015). Resistance parameters in this look-up table were derived based on data from a set of EC towers. Equations and details on PM-Mu can be found in Mu et al. (2011, 2013).

PT-JPL

PT-JPL is also a three source model with total ET contributed from $L_{\mathrm{v}}E_{\mathrm{i}}$, $L_{\mathrm{v}}E_{\mathrm{c}}$ and $L_{\mathrm{v}}E_{\mathrm{s}}$. Using minimal meteorological and radiation information, PT-JPL computes the potential evaporation from each of these sources using the Priestley Taylor model. Based on bio-physiological properties of the land surface, potential evaporation is scaled using reduction functions which represent the impacts of the fraction of green canopy, relative wetness of the canopy, air temperature, and plant and soil water stress. Information for this scaling is provided by NDVI, relative humidity, air temperature, and pressure. The accuracy of $L_{\mathrm{v}}E$ derived from this model depends on the accuracy of optimum plant growth temperature (T_{OPT}), which is defined as the air temperature at the time of peak canopy activity when FPAR that is absorbed, and radiation is the highest, and minimum vapour pressure deficit (VPD) occurs. This optimum

temperature is used to determine temperature constraints in the reduction function for scaling potential evaporation of canopy to actual evaporation. This is based on the assumption that the optimal canopy stomatal conductance happens when green leaf area, light and temperature are high, and VPD is low. For a dry site like Yanco, it is expected that the constraints posed by plant and soil water stress in scaling canopy and soil evaporation would play a bigger role in the accuracy of the derived ET. For further details on the PT-JPL, refer to Fisher et al. (2008).

4.3.5 Statistical evaluation

Comparisons between the scintillometers, the EC systems and MTSAT ET products were based on the root mean square difference (RMSD), Pearson's correlation coefficient (r), bias (negative when the observed value is lower), relative error (RE) and the NashSutcliffe Efficiency (NSE) coefficient where,

$$\mathrm{RE} = \frac{\mathrm{RMSD}}{\overline{L_{\mathrm{v}}E_{obs}}}, \tag{4.1}$$

and

$$\mathrm{NSE} = 1 - \frac{\sum_{i=1}^{n}(L_{\mathrm{v}}E_{i,obs} - L_{\mathrm{v}}E_{i,sim})^2}{\sum_{i=1}^{n}(L_{\mathrm{v}}E_{i,obs} - \overline{L_{\mathrm{v}}E_{o}bs})^2}. \tag{4.2}$$

Observed $L_{\mathrm{v}}E$ data are from the EC system with their mean denoted as $\overline{L_{\mathrm{v}}E_{obs}}$; $L_{\mathrm{v}}E_{i,obs}$ is the ith observed $L_{\mathrm{v}}E$ from the EC system. Similarly, $L_{\mathrm{v}}E_{i,sim}$ is the ith simulated $L_{\mathrm{v}}E$ by the model (i.e. SEBS, PM-Mu or PT-JPL) for n total number of observations. It should be noted that NSE is sensitive to extreme values and can yield sub-optimal results when the dataset contains large outliers. Additionally, whilst it is assumed in this study that the EC measurements represent the "truth", one should be aware of uncertainties in the EC measurements.

4.4 Results and discussion

4.4.1 Comparison between scintillometers

Fig. 4.3 shows scatterplots comparing H derived from the scintillometers distributed across the 4 km $\times$ 4 km satellite grid. The different coloured points represent the wind direction of the derived surface heat flux. The red line shows the linear regression derived from comparing each pair of sensors in the current experiment whereas the blue line represents the linear regression

derived by comparing the same pair of sensors in Yee et al. (2015), when the sensors were placed within the footprint of the EC system. As in the previous chapter, bias here is equivalent to $\overline{x} - \overline{y}$ where $\overline{x}$ is the mean of measurements on the x-axis and $\overline{y}$ is the mean of measurements on the y-axis.

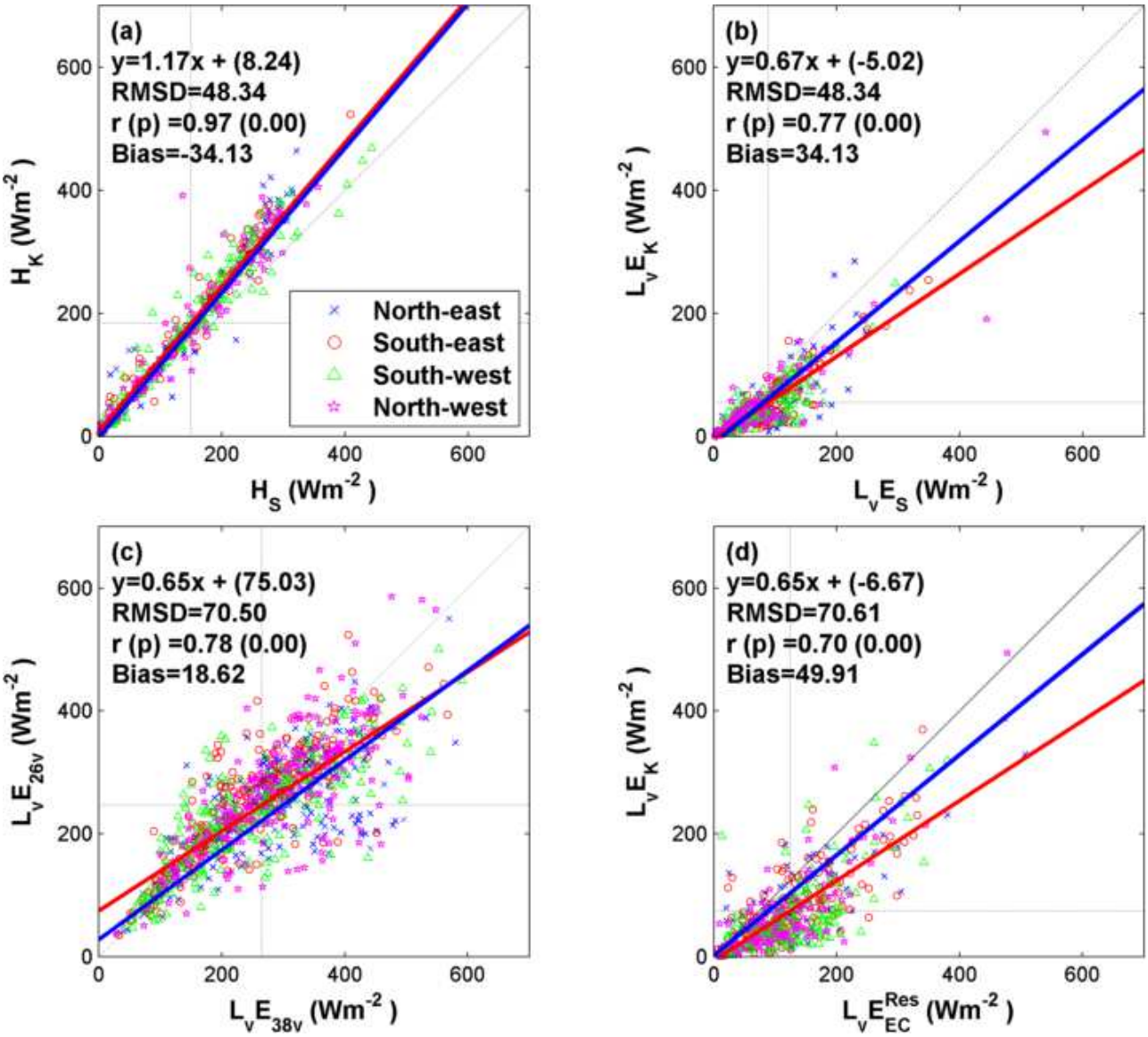

Figure 4.3: *Scatterplots comparing a) H and b) L_vE derived from LAS (subscript K: Kipp, S: Scintec); c) L_vE from microwave scintillometers (subscript 38v: MW38v, 26v: MW26v); and d) L_vE from Kipp and $L_vE_{EC}^{Res}$ EC3. Red line: Regression line derived from current experiment. Blue line: Regression line derived from experiment in Yee et al. (2015). 'p' is the probability from testing the hypothesis of no correlation against the alternative that there is a non-zero correlation.*

Due to differences in how surface heat fluxes are derived from optical and microwave scintillometers, the Scintec are compared with Kipp (optical with optical) and the MW38 with MW26 (microwave with microwave). As seen from Fig. 4.3(a), despite being in different locations, H

Table 4.3: *Summary statistics comparing derived H from current experiment and previous experiment.*

		Previous experiment					Current experiment				
x	**y**	**r**	**RMSD**	**Bias**	**NSE**	**RE**	**r**	**RMSD**	**Bias**	**NSE**	**RE**
H_S	H_K	0.98	49.06	-37.80	0.81	0.22	0.96	48.34	-34.13	0.74	0.32
	H_{38v}	0.79	76.76	45.10	0.36	0.31	0.20	158.54	128.24	-2.26	0.79
	H_{38h}	0.81	73.77	42.61	0.44	0.30	0.14	166.69	137.87	-2.77	0.80
	H_{26v}	0.82	67.52	29.42	0.53	0.27	0.25	181.20	156.81	-2.99	0.81
	H_{26h}	0.70	91.03	61.18	-0.13	0.34	0.23	206.43	190.22	-6.45	0.85
H_K	H_{38v}	0.82	105.36	82.56	0.17	0.35	0.35	195.09	156.56	-1.64	0.80
	H_{38h}	0.84	102.73	79.44	0.25	0.35	0.33	202.35	166.66	-2.03	0.79
	H_{26v}	0.83	91.16	63.91	0.38	0.31	0.59	178.83	151.36	-1.39	0.64
	H_{26h}	0.67	127.45	103.09	-0.67	0.39	0.39	230.63	206.89	-3.98	0.75
H_{38v}	H_{38h}	0.99	12.11	-3.43	0.98	0.06	0.98	11.21	2.27	0.97	0.14
	H_{26v}	0.96	36.29	-23.74	0.84	0.17	0.49	71.93	-19.44	-0.26	0.85
	H_{26h}	0.91	38.36	14.31	0.78	0.17	0.26	89.14	7.65	-0.36	0.95
H_{26v}	H_{26h}	0.95	48.18	38.94	0.71	0.19	0.75	79.95	54.20	0.16	0.55
H_{EC}	H_S	0.96	41.31	13.67	0.90	0.18	0.88	60.05	-20.95	0.75	0.34
	H_K	0.94	51.14	-20.38	0.85	0.21	0.93	70.66	-48.09	0.71	0.38
	H_{38v}	0.82	90.11	61.92	0.36	0.34	0.26	198.31	159.15	-1.94	0.82
	H_{38h}	0.84	86.61	58.61	0.44	0.34	0.25	202.95	167.12	-2.31	0.81
	H_{26v}	0.83	81.97	50.02	0.50	0.31	0.39	198.05	168.92	-2.31	0.75
	H_{26h}	0.74	109.84	83.52	-0.11	0.38	0.32	225.56	201.32	-3.88	0.81

derived from Kipp and Scintec agreed well with a correlation of 0.96 and a bias of 34.13 Wm^{-2} regardless of wind direction.

Table 4.3 summarizes the statistics derived from comparing different scintillometers in the previous experiment with those from the current experiment. Generally, H derived from optical scintillometers compared well with each other and the EC system. Correspondingly, it can be seen that L_vE derived from the optical scintillometers also agreed well with an r of 0.84 and an RMSD of 48.34 Wm^{-2}. Fig. 4.3 (c) shows that L_vE derived from the two microwave scintillometers also agreed despite being in different locations with an r of 0.79 and an RE which is very similar to that of the previous experiment, i.e. 0.24 and 0.27 respectively. Although H derived from the microwave scintillometers did not perform well, this is in-line with findings from Yee et al. (2015), where microwave scintillometers were found to be less accurate for semi-arid environments such as the study area.

Finally, measurements from the scintillometers were compared with measurements from the EC system (Table 4.3 and 4.4). H derived from the optical scintillometers compared well with the EC system with an r of 0.88 and 0.93 for Scintec and Kipp respectively. In

Table 4.4: *Summary statistics comparing derived L_vE from current experiment and previous experiment.*

		Previous experiment					Current experiment				
x	**y**	**r**	**RMSD**	**Bias**	**NSE**	**RE**	**r**	**RMSD**	**Bias**	**NSE**	**RE**
L_vE_S	L_vE_K	0.93	49.06	37.80	0.67	0.33	0.84	48.34	34.13	0.41	0.54
	L_vE_{38v}	0.65	88.83	-53.77	-0.04	0.62	0.42	158.54	-128.24	-6.35	1.92
	L_vE_{38h}	0.67	85.46	-50.86	0.05	0.60	0.39	166.69	-137.87	-6.96	1.98
	L_vE_{26v}	0.64	76.60	-35.78	0.21	0.55	0.33	181.20	-156.81	-9.12	2.24
	L_vE_{26h}	0.50	109.38	-74.97	-0.76	0.73	0.41	206.43	-190.22	-7.75	1.90
L_vE_K	L_vE_{38v}	0.56	113.42	-87.12	-1.38	1.00	0.44	195.09	-156.56	-8.23	2.50
	L_vE_{38h}	0.58	109.66	-83.50	-1.21	0.97	0.40	202.35	-166.66	-8.97	2.51
	L_vE_{26v}	0.55	95.20	-66.37	-0.69	0.85	0.38	178.83	-151.36	-6.98	2.16
	L_vE_{26h}	0.37	137.19	-110.22	-2.66	1.15	0.40	230.63	-206.89	-10.42	2.41
L_vE_{38v}	L_vE_{38h}	0.98	18.54	4.99	0.95	0.09	1.00	11.21	-2.27	0.99	0.04
	L_vE_{26v}	0.87	47.00	26.11	0.66	0.24	0.79	70.50	18.62	0.60	0.27
	L_vE_{26h}	0.78	51.78	-17.86	0.52	0.25	0.69	86.54	-7.52	0.41	0.31
L_vE_{26v}	L_vE_{26h}	0.87	59.16	-44.89	0.18	0.33	0.83	79.95	-53.77	0.22	0.33
L_vE_{EC}	L_vE_S	0.59	118.43	-92.96	-9.52	2.32	0.40	71.53	-39.94	-2.27	1.72
	L_vE_K	0.51	92.02	62.96	-5.06	1.71	0.28	71.77	-20.34	-1.46	1.31
	L_vE_{38v}	0.44	164.26	-148.64	-17.92	2.96	0.14	242.29	242.29	-37.53	4.80
	L_vE_{38h}	0.47	160.26	-144.74	-17.10	2.91	0.12	249.42	-221.85	-40.07	4.88
	L_vE_{26v}	0.49	143.95	-130.57	-18.91	2.90	0.23	249.90	-230.88	-55.12	5.76
	L_vE_{26h}	0.37	189.34	-175.99	-35.15	3.62	0.40	284.34	-267.01	-65.64	6.19
$L_vE_{EC}^{Res}$	L_vE_S	0.90	40.70	-12.94	0.72	0.34	0.69	58.32	23.48	0.33	0.56
	L_vE_K	0.82	50.58	22.09	0.56	0.38	0.77	70.61	49.91	0.17	0.57
	L_vE_{38v}	0.62	96.28	-66.92	-0.55	0.75	0.33	190.69	-152.72	-6.61	1.78
	L_vE_{38h}	0.63	93.68	-63.89	-0.45	0.74	0.33	195.08	-160.45	-6.88	1.77
	L_vE_{26v}	0.57	86.55	-52.75	-0.28	0.71	0.33	191.80	-163.53	-6.83	1.74
	L_vE_{26h}	0.44	122.27	-92.92	-1.77	0.93	0.44	221.04	-197.15	-8.02	1.90

Yee et al. (2015), it was shown that the LASs compared well with the EC data by assuming perfect closure of the energy balance. Therefore, L_vE derived from the EC systems were corrected based on the 'residual-LE closure' method (Twine et al., 2000). The energy budget was forced to close based on the estimate of L_vE_{EC} derived as a residual from the energy balance (i.e., $L_vE_{EC}^{Res} = R_n - G - H_{EC}$). Fig. 4.3(d) compares $L_vE_{EC}^{Res}$ with L_vE derived from Kipp. Comparing the slopes from the current experiment (red) and the previous experiment (blue), the underestimation of L_vE from the optical scintillometers is larger in magnitude (lower slope) compared to the previous experiment. This is likely an effect of the better energy balance closure for the current experiment (slope: 0.85) compared to the previous experiment (slope: 0.79). As a result, it is postulated that the reduced performance of H and L_vE derived from the microwave scintillometers may also be related to R_n - G measured for this experimental period. As seen in Yee et al. (2015), the accuracy of surface heat fluxes derived from microwave scintillometers are

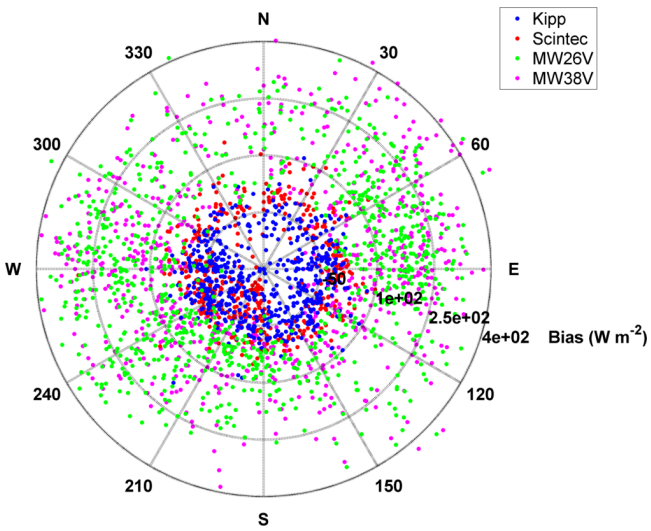

Figure 4.4: *Scatterplots showing difference in* $L_{\mathrm{v}}E_{\mathrm{EC}}^{\mathrm{Res}}$ *(in* Wm^{-2}*) derived from the EC system and scintillometers according to wind-direction. Colours indicates scintillometer.*

very prone to errors in the assumption made regarding parameters such as vegetation height, and R_{n} - G, particularly for a semi-arid environment and when scintillometer heights are low. As the experimental period here encompassed three seasons as opposed to one in the previous experiment, a larger variation in vegetation height and meteorological conditions are expected, thereby increasing the uncertainty of the derived fluxes. Nevertheless, comparisons between optical scintillometers and between microwave scintillometers showed good agreement, which supports the hypothesis that the fluxes from different areas within the 4 km pixels are similar due to homogeneity of the site.

The difference between measurements from the EC system and the scintillometers were then delineated based on wind direction. Based on Fig. 4.4, it can be seen that regardless of wind direction, the difference between measurements from EC3 and the scintillometers are of the same order. Likewise, if these differences were delineated based on wind speed (Fig. 4.5), there was little correlation between wind speed and the flux differences.

Based on these comparisons which have been carried out in this section, it can be concluded that 1) spatial distribution of surface heat fluxes within the MTSAT 4 km pixel is homogeneous and therefore, 2) measurements from EC3 is representative of the areal surface heat flux of the MTSAT 4 km pixel. Moreover, this hypothesis can be extended to EC1 and EC2.

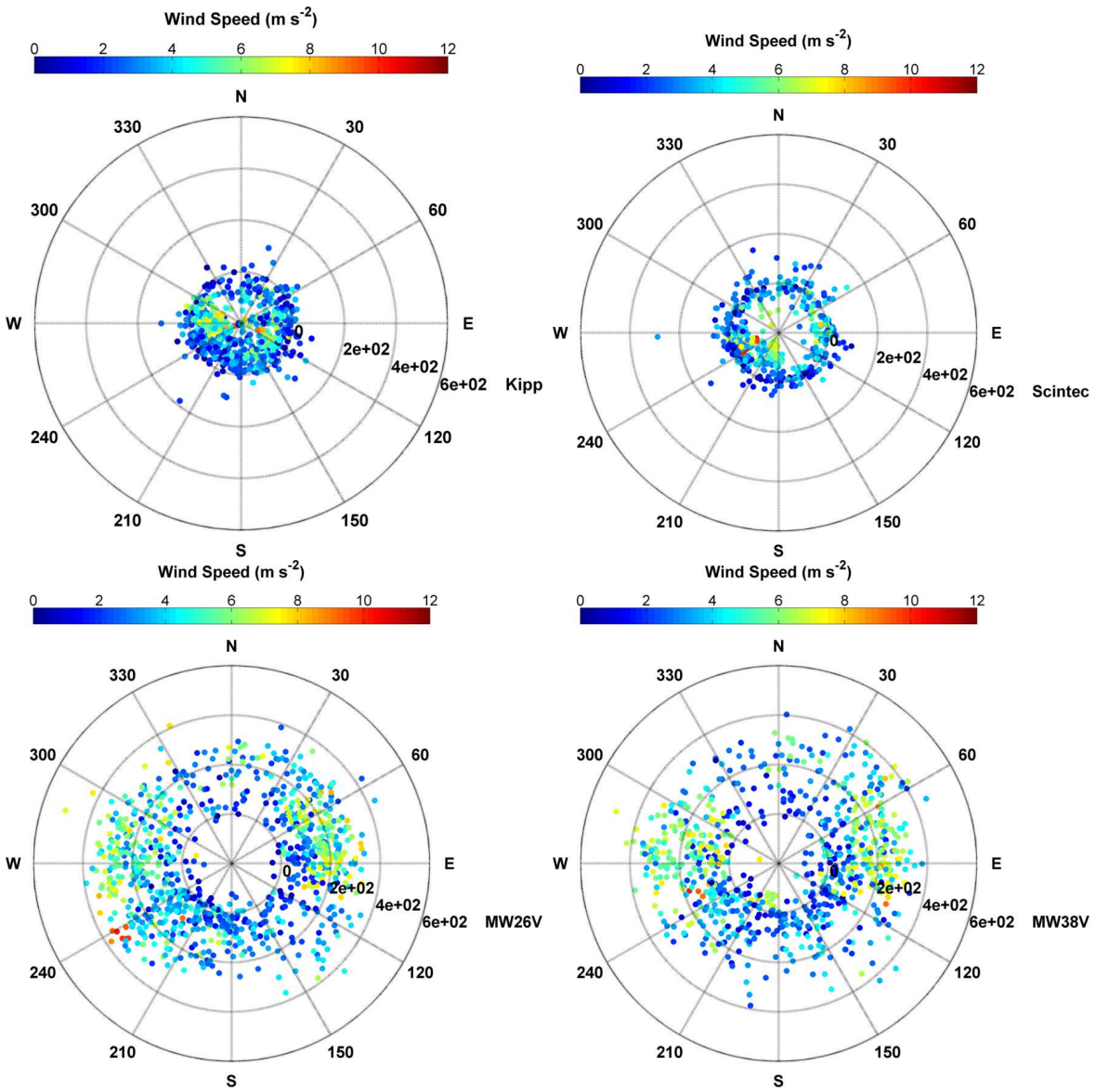

Figure 4.5: *Scatterplots showing difference in* $L_{\mathrm{v}}E_{\mathrm{EC}}^{\mathrm{Res}}$ *(in* Wm^{-2}*) derived from the EC system and scintillometers (as indicated by name) according to wind-direction. Colours indicate magnitude of wind speed.*

4.4.2 Validation of RS ET product

Overall Performance

As it has been shown that EC3 is representative of the MTSAT satellite pixel, and by default EC1 and EC2, measurements from EC1, EC2 and EC3 are used to validate the MTSAT ET products. Due to the homogeneity of the grassland where the EC systems were located, it is assumed that the measurements from all EC stations are representative of the MTSAT pixel in which EC3 is located. The energy balance closure of the different stations were investigated and shown to have a slope of 1.04, 0.75 and 0.87 respectively (Fig. 4.6).

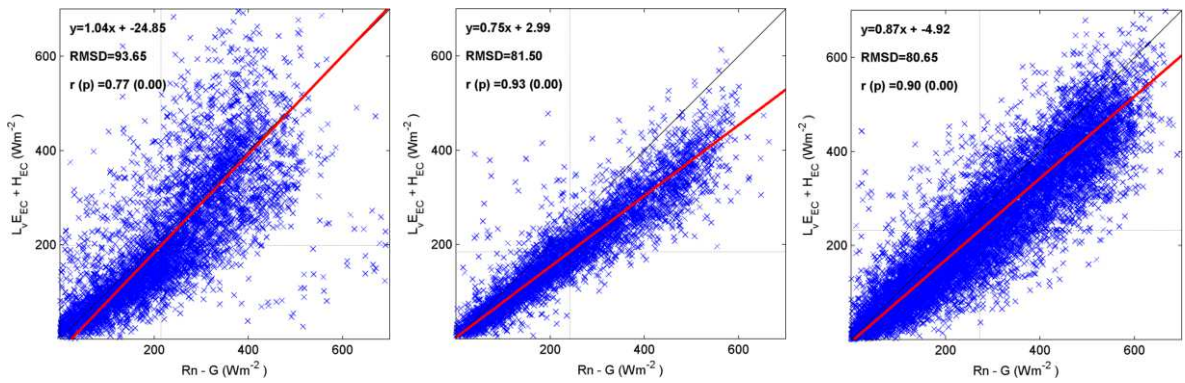

Figure 4.6: *Energy balance closure of EC1, EC2 and EC3 (left to right). Solid black line: 1:1 line. Solid red line: fitted line from orthogonal regression.*

Measurements from EC1, EC2 and EC3 have been collated into a single dataset which are referred to collectively as measurements from the EC system. These L_vE measurements from the EC system (L_vE_{EC}) (first row) were also corrected based on the 'residual-LE closure' ($L_vE_{\mathrm{EC}}^{\mathrm{Res}}$) (2nd row) and β correction technique ($L_vE_{\mathrm{EC}}^{\beta}$) (third row) before comparison with L_vE derived from the SEBS, PM-Mu and PT-JPL remote sensing ET models in Fig. 4.7. The EC measurements have been re-sampled at the hourly time-steps when remote sensing ET products were available. Hourly data from the EC system and the model were then filtered in such a way that only times where measurements were available from the EC system and all three models were available.

Generally, it can be seen that regardless of the L_vE used for comparison, PT-JPL outperformed the other two models with an r which ranged from 0.68 to 0.71 and an RMSD ranging from 51.05 W m^{-2} to 63.27 W m^{-2}. This is in-line with the results of previous studies (e.g. Ershadi et al., 2014; McCabe et al., 2015). When L_vE and $L_vE_{\mathrm{EC}}^{\mathrm{Res}}$ were used, SEBS performed better than PM-Mu whereas PM-Mu performed better when compared with $L_vE_{EC}^{\beta}$. In-comparison with the EC system, H from SEBS underestimates H with an RMSD of 92.90 W m^{-2} and r of 0.75. Another observation is that NSE derived from the comparisons of SEBS and PM-Mu showed that the models did not perform well with NSE < 0 for the majority of the pairs. This indicates that the observed mean is a better predictor than the model. As pointed out by Ershadi et al. (2014), depending on L_vE used for comparisons, the performance will differ. This is because L_vE from SEBS is calculated as a residual from observations of H whereas the PM-Mu method assumes similarity between H and L_vE which would be in-line with the assumptions of the β correction method. As Foken et al. (2011) have shown,

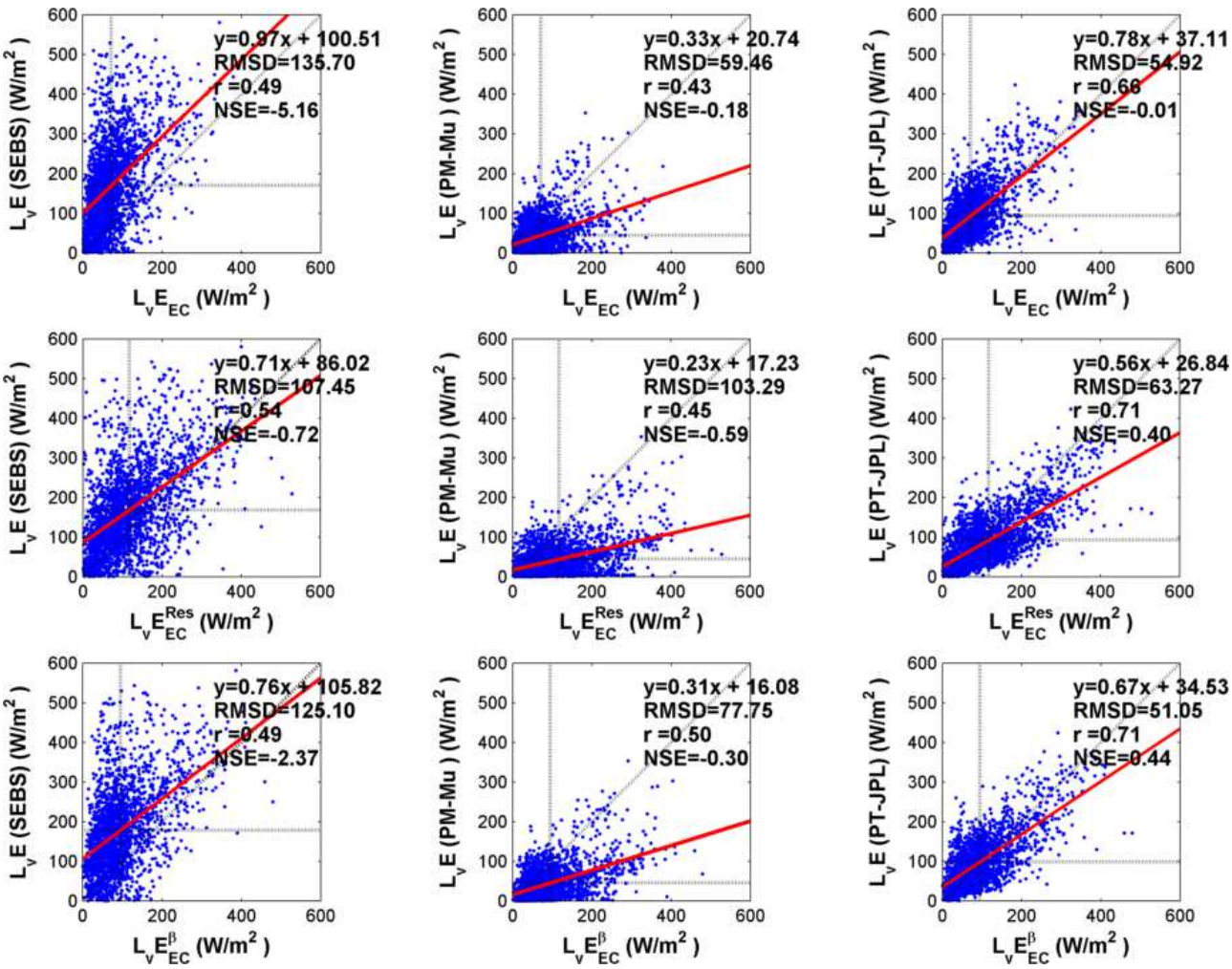

Figure 4.7: *Scatterplots comparing L_vE measured (top row), derived as a residual (middle row) and β-corrected (bottom row) from EC systems based on SEBS, PM-Mu and PT-JPL (left to right). Red solid line: Linear regression. Black dotted line: Mean of corresponding measurements and the 1:1 line.*

$L_vE_{EC}^{\beta}$ may be less accurate due to the lower reliability of the IRGA compared to the sonic anemometer, and lack of similarity between the transportation of H and L_vE; accordingly, unless specified, $L_vE_{EC}^{Res}$ is used for computing RMSD, r, bias, RE and NSE in the remaining sections of this study.

To better understand the distribution of $L_vE_{EC}^{Res}$ derived from the EC system and models, Fig. 4.8 summarizes their median, quartile, minima and maxima. It can be seen from the boxplots that the distribution of the observations have a positive skewness. All models and the EC system have the same minima as measurements lower than 0 W m^{-2} were filtered out prior to comparisons. Table 4.5 also summarizes the mean and standard deviations of $L_vE_{EC}^{Res}$ and L_vE based on MTSAT products. The Kruskal-Wallis non-parametric test was repeated for each pair, showing that the distribution of all datasets did not have the same median (p <

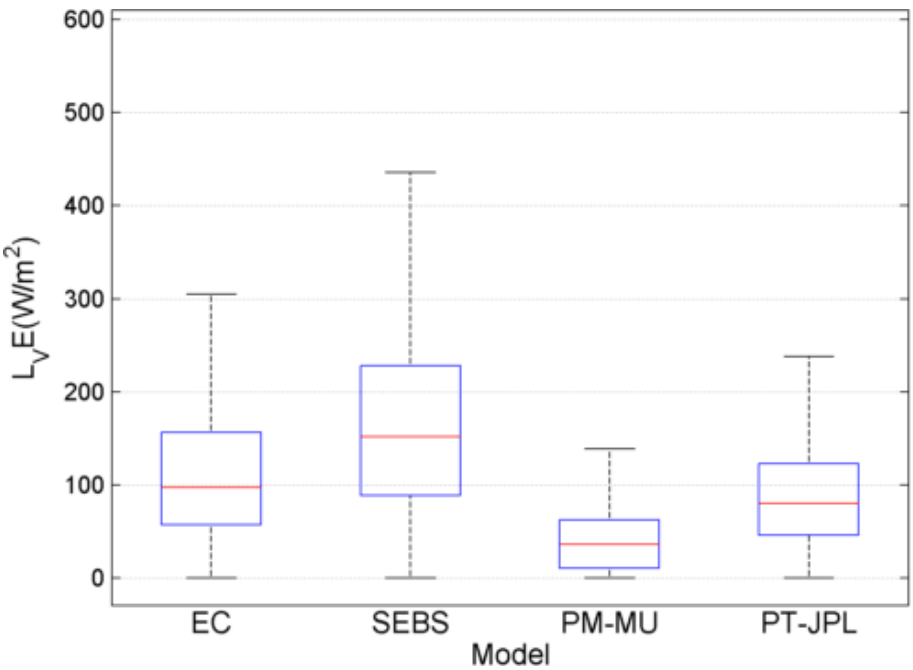

Figure 4.8: *Boxplots showing the median (red line), 25th and 75th percentile (q_1, q_3) (edge of box), minima and maxima excluding outliers (whiskers) of L_vE^{Res} measured from the EC system and remote sensing models.*

0.01). Additionally, as the r assumes a linear relationship, the correlation between the $L_vE_{EC}^{Res}$ and the models were computed using Kendall's Tau correlation coefficient (τ). Whilst the τ (and Spearman's rank) were lower than r for all cases, PT-JPL still performed the best (Table 4.5).

Table 4.5: *Summary statistics comparing L_vE as a residual from the EC system and ET models. Stdev: Standard deviation r: Correlation coefficient. τ: Kendall's correlation coefficient. m and c: slope and intercept derived from linear regression.*

Source	Period	Mean	Stdev	r Pearson	r Spearman	τ Kendall	RMSD	m	c	Bias	NSE	RE
EC	All	116.71	82.01	-	-	-	-	-	-	-	-	-
	Su	111.56	78.72	-	-	-	-	-	-	-	-	-
	Au	126.67	106.99	-	-	-	-	-	-	-	-	-
	Wi	99.61	58.75	-	-	-	-	-	-	-	-	-
	Sp	140.90	83.22	-	-	-	-	-	-	-	-	-
SEBS	All	168.31	107.91	0.54	0.52	0.37	107.45	0.71	86.02	-51.60	-0.72	0.92
	Su	174.10	126.26	0.27	0.28	0.19	143.97	0.43	126.60	-62.54	-2.35	1.29
	Au	163.11	103.68	0.67	0.57	0.41	93.47	0.65	81.35	-36.44	0.24	0.74
	Wi	141.53	79.45	0.59	0.56	0.40	77.29	0.80	61.54	-41.92	-0.73	0.78
	Sp	218.30	124.51	0.49	0.51	0.36	135.05	0.73	115.00	-77.40	-1.64	0.96
PM-MU	All	44.12	42.14	0.45	0.38	0.26	103.29	0.23	17.23	72.59	-0.59	0.89
	Su	10.17	17.93	0.30	0.53	0.37	126.22	0.07	2.51	101.39	-1.58	1.13
	Au	42.25	38.07	0.65	0.58	0.42	121.14	0.23	12.76	84.42	-0.28	0.96
	Wi	52.65	35.04	0.32	0.28	0.19	74.60	0.19	33.66	46.96	-0.61	0.75
	Sp	54.00	55.60	0.59	0.56	0.41	110.13	0.39	-1.24	86.90	-0.75	0.78
PT-JPL	All	92.42	65.17	0.71	0.64	0.47	63.27	0.56	26.84	24.29	0.40	0.54
	Su	63.59	42.37	0.66	0.70	0.51	76.56	0.36	23.78	47.97	0.05	0.69
	Au	105.29	81.33	0.82	0.71	0.53	65.11	0.62	26.31	21.38	0.63	0.51
	Wi	86.23	54.97	0.60	0.54	0.39	52.64	0.56	30.25	13.39	0.20	0.53
	Sp	110.12	67.74	0.69	0.67	0.49	68.63	0.56	31.34	30.78	0.32	0.49

From Table 4.5, it can be seen that due to the large differences in means, NSE alone is not enough to gauge the performance of the MTSAT ET products. Moreover, the NSE coefficient assumes that the distributions are normal. To further complicate the diagnosis, as mentioned in Ershadi et al. (2014), it is possible that measurement uncertainty might be equal to modelling uncertainty when $L_{\mathrm{v}}E$ is low. In fact, for an arid or semi-arid environment, such as the study area, mean $L_{\mathrm{v}}E_{\mathrm{EC}}^{\mathrm{Res}}$ is of the same magnitude ($\sim$ 116.71 W m^{-2}) as G (varies from 50 W m^{-2} to 170 W m^{-2}) and the energy balance non-closure ($\sim$ 80 W m^{-2}). Similarly, McCabe et al. (2015) found that a reduction in the skills of SEBS, PM-Mu and PT-JPL for arid sites, particularly for the first two.

Clearly, the low values of $L_{\mathrm{v}}E$ and non-closure of the EC system complicates the validation of remote sensing ET products, particularly for a semi-arid environment (Polhamus et al., 2013). Therefore, future studies should consider these issues in evaluating the performance of ET models by using a range of statistics to gauge the performance of each model. For instance, Cammalleri et al. (2013) introduced a statistical evaluation approach based on an ensemble-based inter-comparison method to better account for uncertainties in ET fluxes using EC measurements.

Finally, it can be seen here that despite using the same forcing data, actual ET modelled by the three remote sensing ET models showed vast differences, with SEBS derived $L_{\mathrm{v}}E$ having the largest variation followed by PT-JPL and PM-Mu. This is because the different models partitioned available energy into $L_{\mathrm{v}}E$ in different ways. In the case of SEBS, this partitioning is highly sensitive to LST (hourly input) prescribed to the model. On the other hand PM-Mu and PT-JPL partitions the available energy based on the NDVI (bi-monthly input) which acts as a proxy for vegetation phenology. To further investigate the cause for different performances of the model, the hourly and seasonal performance of the models are compared below.

Diurnal and seasonal pattern

Fig. 4.9 shows the mean diurnal pattern between 7 am and 9 pm (unstable conditions) of $L_{\mathrm{v}}E_{\mathrm{EC}}^{\mathrm{Res}}$ and $L_{\mathrm{v}}E$ from the models throughout the study period. As observed in the scatterplots of Fig. 4.7, SEBS overestimates $L_{\mathrm{v}}E$ whereas PM-Mu and PT-JPL underestimates. Whilst the diurnal pattern of the EC system is most closely depicted by PT-JPL, it can be seen that using

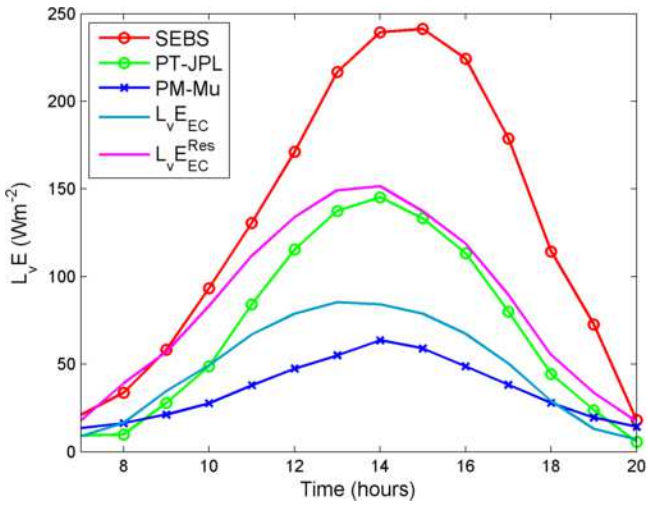

Figure 4.9: *Daily pattern of L_vE from each ET model and $L_vE_{EC}^{Res}$*

similar meteorological data, L_vE from SEBS peaks approximately an hour later than PM-Mu and PT-JPL. This may be an effect of the LST input from MTSAT used by SEBS.

To derive mean diurnal patterns by seasons, due to a lack of points for certain seasons, all available measurements have been used to get a sense of L_vE from each model in comparison to the EC system (Fig. 4.10). Generally, based on visual inspection, all remote sensing models are seen to perform well in summer. However, around 8 am to 10 am, $L_vE_{EC}^{Res}$ is seen to be higher than L_vE from the remote sensing models during autumn, winter and spring. This may be caused by uncertainties in measurements of R_n and G, or the minimum conditions defined by the remote sensing models for ET to occur may be too stringent, or soil evaporation may have been driven by G during these periods. It is to be noted, however, that the derived patterns may be biased due to the number of measurements available to derive them.

In terms of L_vE_{EC} (Fig. 4.10, bottom), this earlier peak is also observed in autumn and winter. It is interesting to see that PM-Mu also depicts this pattern during autumn. Further investigations revealed that L_vE_s simulated by PM-Mu was the main component of total L_vE the majority of the time, whereas L_vE_i and L_vE_c was a lot lower than that of PT-JPL, suggesting that the underestimation from PM-Mu may be due to uncertainty in the specification of vegetation type or parameters. McCabe et al. (2015) have also observed a decrease in the performance of PM-Mu for drier sites, possibly because ET consists of a small portion of total available energy (low evaporative fractions). Moreover, L_vE_s from PM-Mu is generally higher than that of PT-JPL during summer. Finally, a closer look at the individual components of L_vE showed that whilst L_vE_i, L_vE_c and L_vE_s from PT-JPL followed the diurnal pattern of R_n,

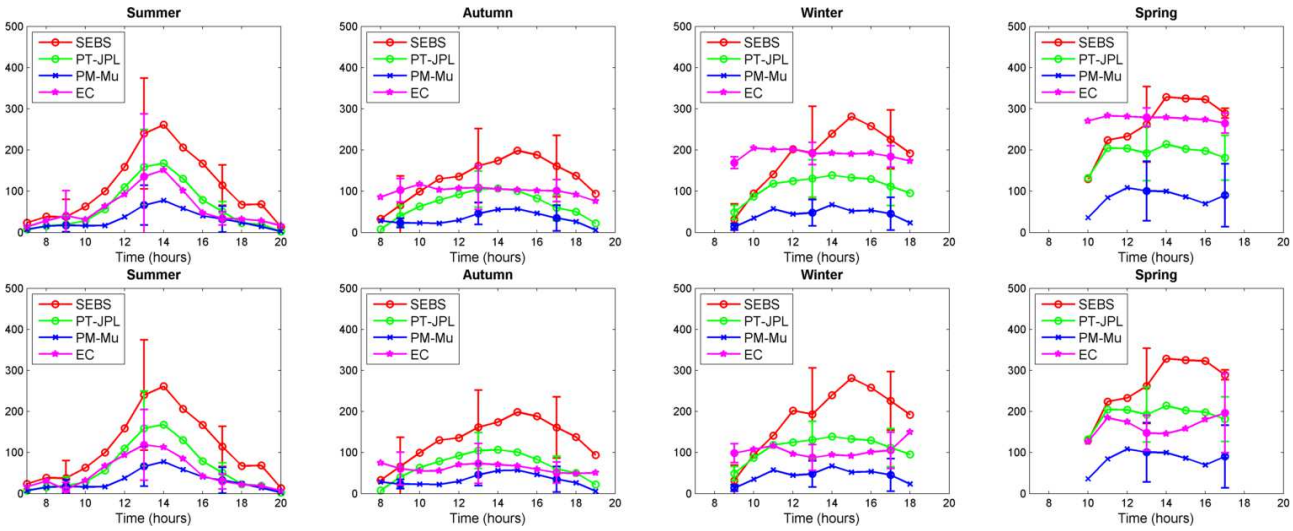

Figure 4.10: *Diurnal pattern based on seasons for L_vE derived as a residual (top) and L_vE measured (bottom). Whiskers represent the max and min.*

L_vE_s from PM-Mu begins earlier than the other components, thereby leading to a small peak earlier in the morning as also observed in L_vE_{EC}. This suggests that whilst the magnitude of L_vE derived from PM-Mu is too low, the scheme used by PM-Mu to simulate L_vE_s may be more appropriate for a semi-arid environment where ET may have been driven by G prior to sun-rise.

Hourly and seasonal performance

To investigate the performance of the model for each hour and season, the difference between L_vE_{EC} and modelled L_vE was delineated based on the hour and season. Based on Fig. 4.11, the bias between the EC system and SEBS corresponds to R_n and peaks at about 3 pm. As a result, RE is seen to be quite consistent throughout the day with SEBS having a lower RE than PM-Mu in the morning and inversely during the afternoon. The increase in RE and decrease in NSE across the day is likely affected by the increase in bias. If one were to establish the performance of SEBS solely on bias, RE and NSE, SEBS might have been mistaken for not performing well. However, by comparing the performance of SEBS with the other two models, it can be seen that for the majority of the time, bias, RE and NSE changed directions at similar times which indicates that the bias is likely to originate from biases in the ACCESS forcing as compared to actual meteorological conditions, rather than the ET model itself. However, further comparisons between the input forcing with *in situ* measurements is recommended to affirm this. Nevertheless, McCabe et al. (2015) also observed that SEBS was

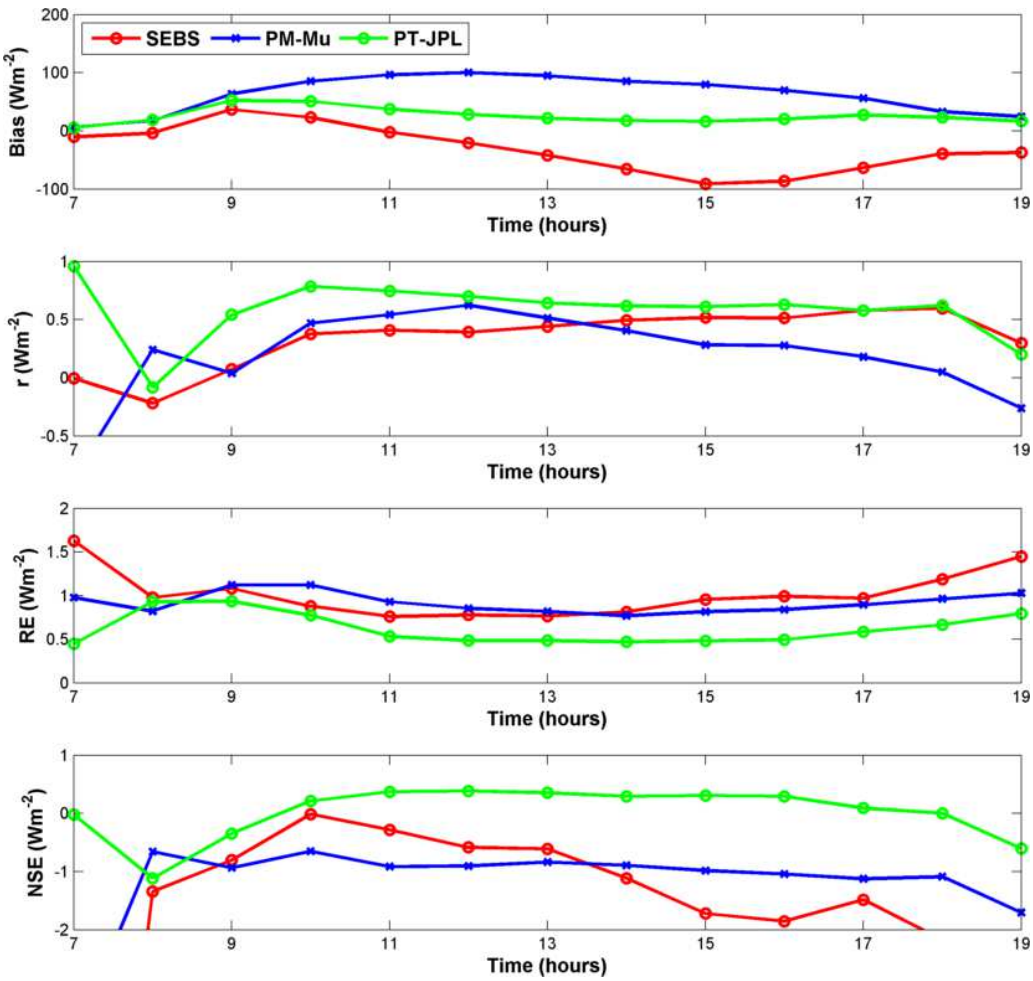

Figure 4.11: *Hourly pattern of statistics comparing $L_{\mathrm{v}}E_{\mathrm{EC}}^{\mathrm{Res}}$ from EC systems and $L_{\mathrm{v}}E$ derived based on different remote sensing models.*

more sensitive to forcing data than PM-Mu and PT-JPL. Conversely, while it was also found in the aforementioned study that PM-Mu was least sensitive to the forcing, it can be seen in Fig 4.11 that r of PM-Mu decreases sharply after 12 pm whereas r of SEBS increases after 10 am. Unlike bias, RE and NSE, which are seen to change relative to each other, the hourly pattern of r is different. Ershadi et al. (2014) found that although SEBS overestimated evaporation, its correlation with EC measurements was high. It is possible that as the day progresses and the role of LST increases, inputs from MTSAT helped to improve the performance of SEBS.

Performance of each model was investigated based on seasons and plotted as boxplots (Fig. 4.12). The derived statistics are also summarized in Table 4.5. Although the amount of data available for each season will influence the results (since only times where data was available from the EC system and all models was considered), it is expected that the results will still give an indication of the spread and performance of the models relative to the EC system.

Although most rainfall occurs during winter, the available energy for ET to occur during

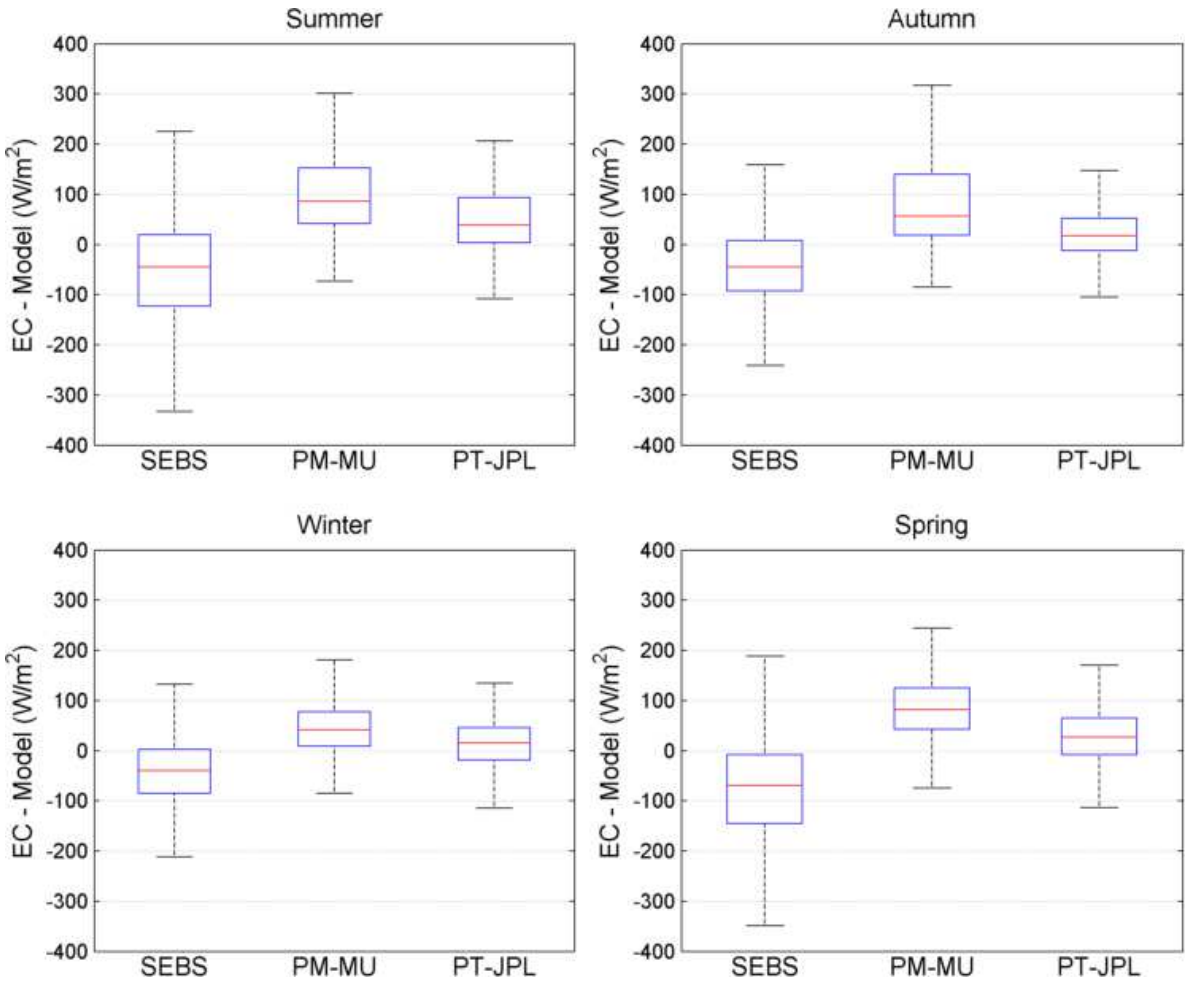

Figure 4.12: *Boxplot of bias between L_vE from EC systems and L_vE derived based on different remote sensing models.*

winter is low. From Table 4.5, it can be seen that $L_vE_{EC}^{Res}$ was the lowest during winter followed by summer, autumn and spring. In terms of variation, the standard deviation of $L_vE_{EC}^{Res}$ was the lowest in winter, followed by summer, spring and finally autumn. However, L_vE_{EC}, was the lowest during summer followed by winter. It is likely that during summer and winter, as the magnitude of L_vE is low, performance of the models will depend on the L_vE used to validate the ET model. During autumn and spring, as L_vE is larger in magnitude, the energy balance non-closure is less likely to affect the results. As before, the effect of bias on NSE and RE can be seen comparing bias, NSE and RE of SEBS and PM-Mu.

In terms of r, based on $L_vE_{EC}^{Res}$, it can be seen that all models had the highest correlation during autumn but their performance differed for other seasons. PT-JPL performed reasonably well regardless of season, whereas r for SEBS and PM-Mu was the lowest during summer, 0.27 and 0.30 respectively. As vegetation phenology from all three models were similar, the schemes employed by SEBS and PM-Mu to derive roughness or aerodynamic and surface resistance

from NDVI could have led to the poor performance of the models. Aerodynamic and surface resistance parameters used within PM-Mu are based on a lookup table which has been calibrated based on a number of FLUXNET sites. Consequently, it is likely that the parameters are unsuitable for the vegetation which exists in the study area, as different plant species may react differently in similar meteorological and water availability conditions (Mackay et al., 2003; Polhamus et al., 2013). In the case of SEBS, uncertainty is caused by an underestimation of H (and therefore overestimation of $L_{\mathrm{v}}E$). Su (2002) found that errors in the scalar roughness height for heat transfer estimated based on observations of vegetation phenology can lead to errors of the same magnitude or larger than uncertainties caused by errors in meteorological data. During summer, water availability is low whereas available energy is high. Therefore, potential $L_{\mathrm{v}}E$ is high and the role played by soil moisture and vegetation in the partitioning of energy increases. Conversely, although most rainfall occurs during the second half of the year, potential ET is constrained by available energy. As a result, model performance is the highest during autumn, and lowest during summer (Fig. 4.12). Previously, PM-Mu was shown to be able to simulate an early peak in $L_{\mathrm{v}}E$ during autumn (Fig. 4.10). However, based on statistics derived between $L_{\mathrm{v}}E_{\mathrm{EC}}$ and $L_{\mathrm{v}}E$ from the remote sensing ET models, r of PM-Mu during autumn (0.65) was still lower than SEBS and PT-JPL (0.67 and 0.76 respectively). Further investigations with a more complete set of measurements will be needed to investigate the influence of G.

Daily ET

To obtain daily ET, hourly $L_{\mathrm{v}}E$ were firstly interpolated using a cubic interpolation for gaps shorter than 18 hours. These gap-filled measurements were then converted into mm hr^{-1} for each hour and summed from 7 am to 7 pm. Therefore, the "daily flux" plotted in Fig. 4.13 is in fact only ET which occurs from 7 am to 7 pm (day-time). Only days in which measurements were available from the EC system and all ET products were used in the analysis. This reduced the number of days to just 59, in which 13 were during summer, 6 during autumn, 19 during winter, and 21 during spring (Fig. 4.13). It can be seen that whilst both PM-Mu and PT-JPL underestimates $L_{\mathrm{v}}E$ in comparison to $L_{\mathrm{v}}E_{\mathrm{EC}}^{\mathrm{Res}}$, the dynamics from these two-models follow closely that of the EC system. Conversely, SEBS had a larger range thereby causing it to under-

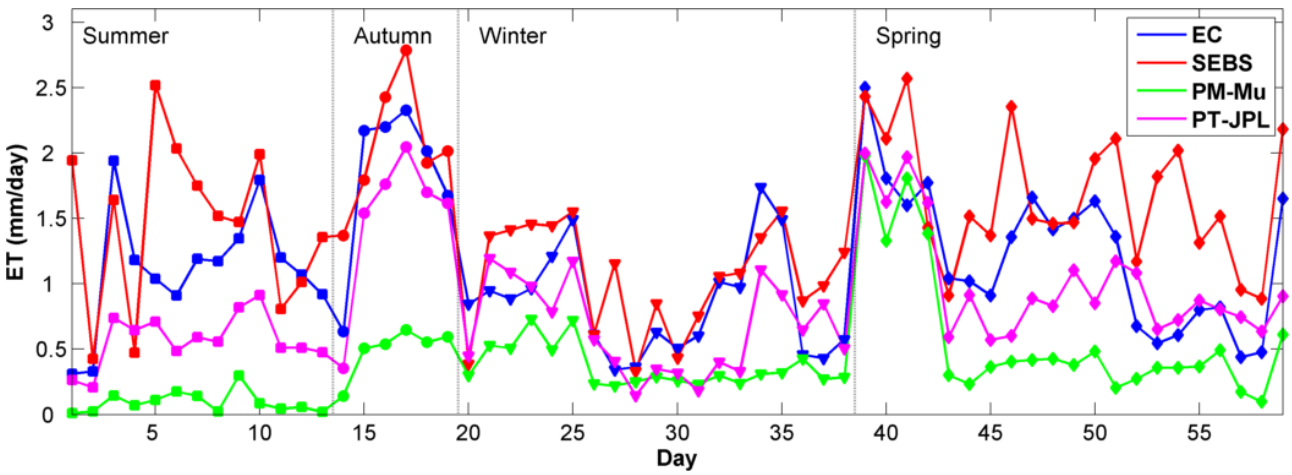

Figure 4.13: *Comparison of daily $L_v E_{EC}^{Res}$ and $L_v E$ derived based on remote sensing ET models for 59 days of concurrent data. The comparisons have been lumped according to seasons whereby measurements for each seasons are not in any particular order.*

or overestimate.

Based on the Kruskal-Wallis test, the daily ET from these different measurement methods did not have distributions with equal medians ($p < 0.01$). It can also be clearly seen from the histograms in Fig. 4.14 that they have different distributions. Multiple comparison of the mean ranks showed that the mean rank of ET from the EC system was significantly different from PM-Mu but not SEBS and PT-JPL. Aggregating ET from hourly to daily time scales improved the agreement between all models and the EC system (Fig. 4.15) as noise in the data or any temporal mismatch and issues related to energy closure are minimized (Finnigan et al., 2003). PT-JPL had the highest r and lowest RMSD in both cases, thereby making it the most reliable model based on this validation study followed by SEBS and PM-Mu.

Ershadi et al. (2014) concluded that the accuracy of LST and air temperature, derived aerodynamic resistance and surface roughness parameters based on NDVI were the most important factors affecting the accuracy of derived ET based on SEBS. Similarly, in the case of PM-Mu, estimation of surface and aerodynamic resistance based on a combination of the predetermined look-up table and meteorological conditions are likely to contribute to uncertainties in derived ET. Moreover, as the use of a high-quality tower dataset in PM-Mu showed a depreciation in performance in the aforementioned study, the model's structure and physics itself may be inaccurate. The good performance of PT-JPL has been attributed to its minimal requirement of data as inputs, thereby reducing the propagation of errors from the inputs. Its simple yet robust scheme of scaling potential ET to actual ET based on plant physiological status and soil

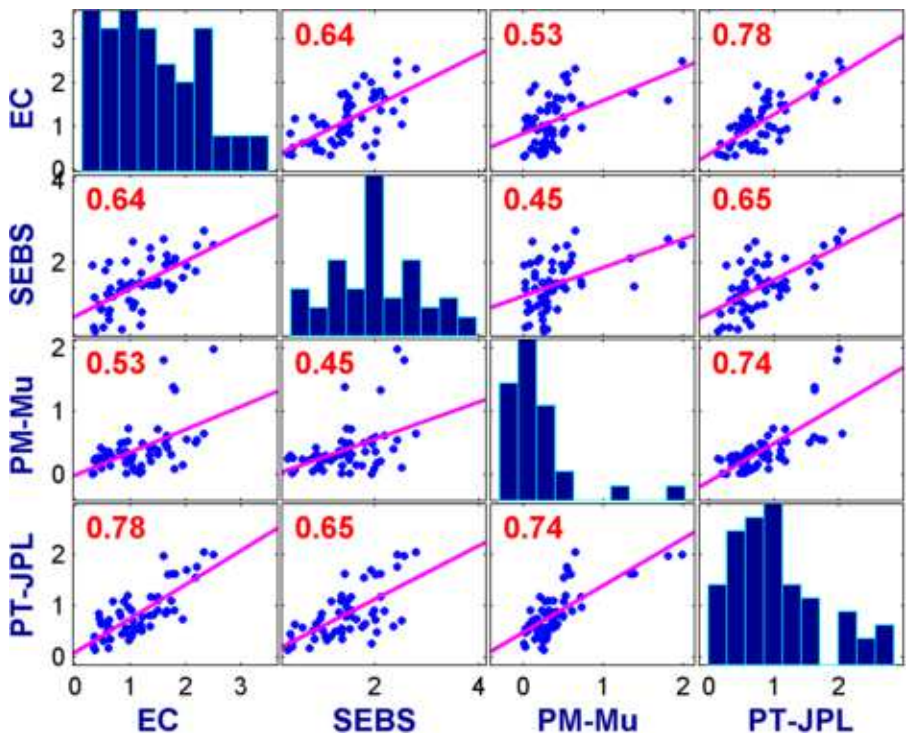

Figure 4.14: *Correlation matrix comparison of daily $L_{\mathrm{v}}E_{\mathrm{EC}}^{\mathrm{Res}}$ and $L_{\mathrm{v}}E$ derived based on remote sensing ET models for 59 days of concurrent.*

moisture availability has been found to perform well in previous studies (e.g. Ershadi et al., 2014; McCabe et al., 2015). Nevertheless, due to the importance of soil moisture in semi-arid environments, there is still room for improving PT-JPL estimates. García et al. (2013) showed an improvement in ET estimates by incorporating observations of soil moisture (or thermal inertia as a proxy) to improve the plant and soil moisture scaling scheme of PT-JPL. The assimilation of soil moisture remote sensing products from AMSR-2, SMOS or SMAP into remote sensing ET models such as PT-JPL (and SEBS or PM-Mu) is therefore expected to improve estimates of ET.

4.4.3 PT-JPL spatial distribution of ET

As PT-JPL has been shown to be the most suitable for the semi-arid environment of the study area, the ability of the model to replicate the variability of $L_{\mathrm{v}}E$ for a bigger area was investigated. Fig. 4.16 shows the mean $L_{\mathrm{v}}E$ derived based on PT-JPL for each season, whereas Fig. 4.17 shows its standard deviation. A comparison with Fig. 4.1 shows that PT-JPL can correctly detect the higher and larger range of ET expected at the north-western corner of the site where irrigated agricultural activities can be found during summer, and where a line of

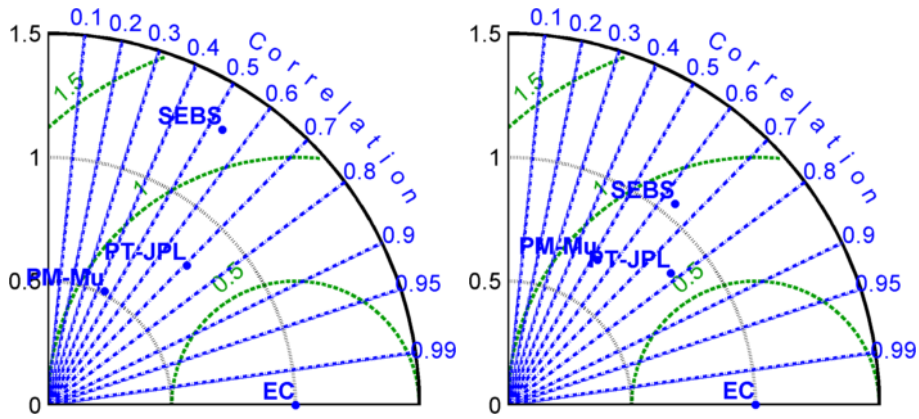

Figure 4.15: *Taylor diagram summarizing key statistics of ET models relative to EC for hourly L_vE (left) and daily ET (right). The statistics are based on centered RMSD (green radial axis), standard deviation normalized by standard deviation of EC (black) and correlation coefficient (blue spokes).*

trees along a river exist running from the east to north-west of the study area. The variation of L_vE was quite similar where the grasslands for grazing can be found south-west of the study area. Both the mean and standard deviation were the lowest during winter whereas the spatial variation of ET was the largest during summer due to the presence of mixed activities in the study area. Both autumn and spring showed very similar mean and standard deviation of L_vE. This shows that the PT-JPL ET product is suitable for mapping the temporal and spatial distribution of ET within the Yanco study area. As PT-JPL uses a minimum of meteorological and remote sensing inputs, it is less prone to errors in the input data itself. Moreover, as PT-JPL uses scaling function derived from the inputs themselves rather than parameters which have been tuned or calibrated (such as the look up table of PM-Mu), it is able to perform well regardless of the biome type.

4.5 Conclusion

This study investigated the representativeness of an EC tower for long-term validation of various MTSAT ET products. Scintillometers were placed across a single MTSAT ET product pixel to measure the contribution of L_vE from different areas within the pixel. As shown in Yee et al. (2015), microwave scintillometers were not suitable for use in a semi-arid environment. However, based on the comparisons between two LASs, it was found that regardless of wind direction derived L_vE agreed with an r of 0.84 and RMSD of 48.34 W m^{-2}, whereas the two microwave scintillometers had an r of 0.79 and RMSD of 70.50 W m^{-2}. The LAS were then

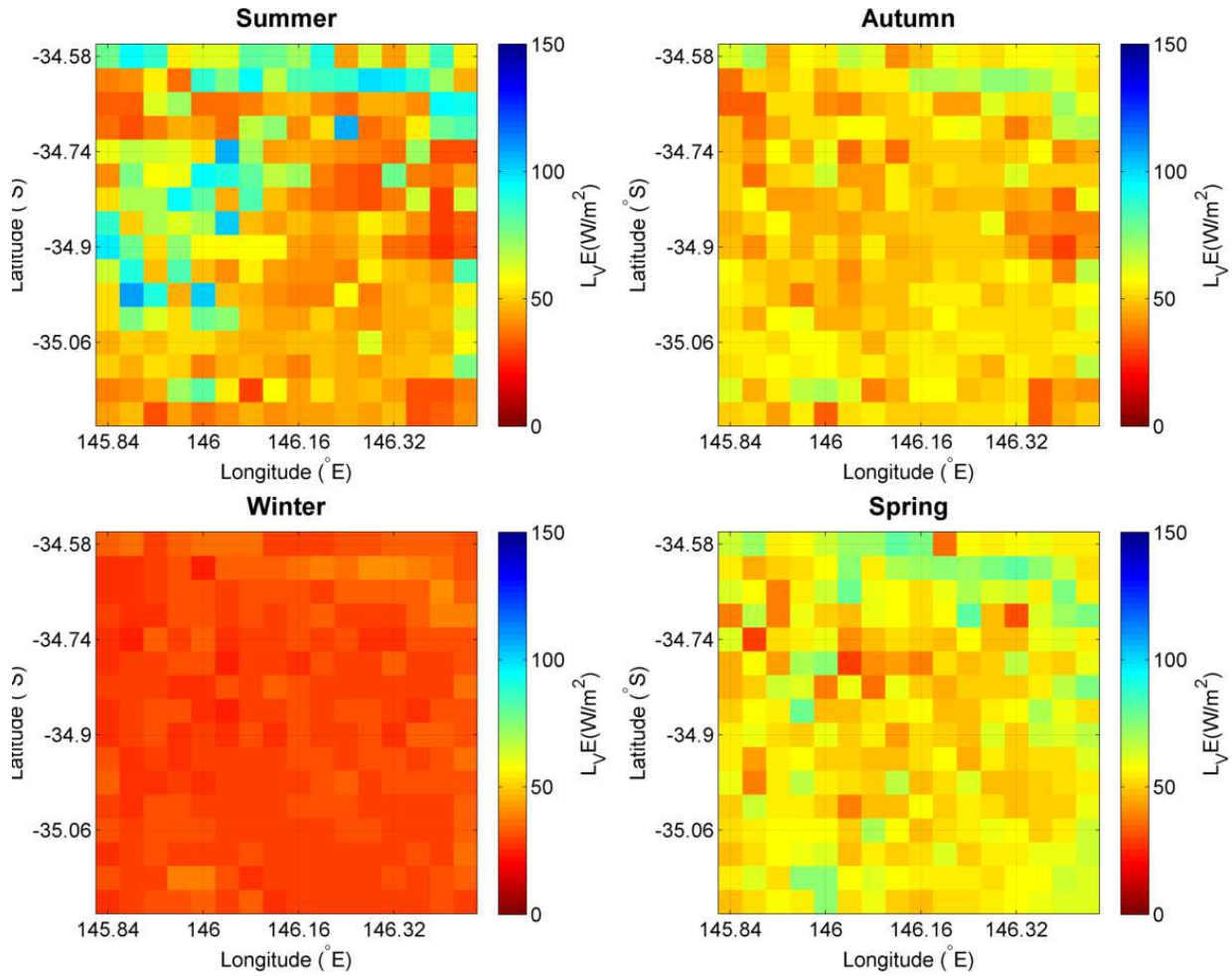

Figure 4.16: *Average L_vE derived based on PT-JPL at 12 pm for each season within Yanco.*

compared with $L_vE_{EC}^{Res}$ and it was found that they had an r of 0.69 and 0.77 and RMSD of 58.32 W m^{-2} and 70.61 W m^{-2} respectively. Therefore, it was concluded that measurements from the EC system are representative of the entire 4 km ET product due to homogeneity within the pixel.

Following the results of the above comparison, the MTSAT ET product was validated and the PT-JPL model found to be the best performer when compared to hourly $L_vE_{EC}^{Res}$, having an r of 0.71 and an RMSD of 63.27 W m^{-2}. However, SEBS was found to overestimate and PM-Mu to underestimate. Although PT-JPL uses a relatively simple and largely empirical formulation of the evaporative process, it was able to perform better than the other two models (Ershadi et al., 2014). As a result, ET models such as PT-JPL which utilizes 1) scaling functions derived as a function of conditions of the study area itself, 2) does not require any pre-calibration or tuning of parameters, and 3) requires minimal input forcing perform better. Conversely, as LAI and fractional vegetation cover, which are used to derive surface roughness, and aerodynamic

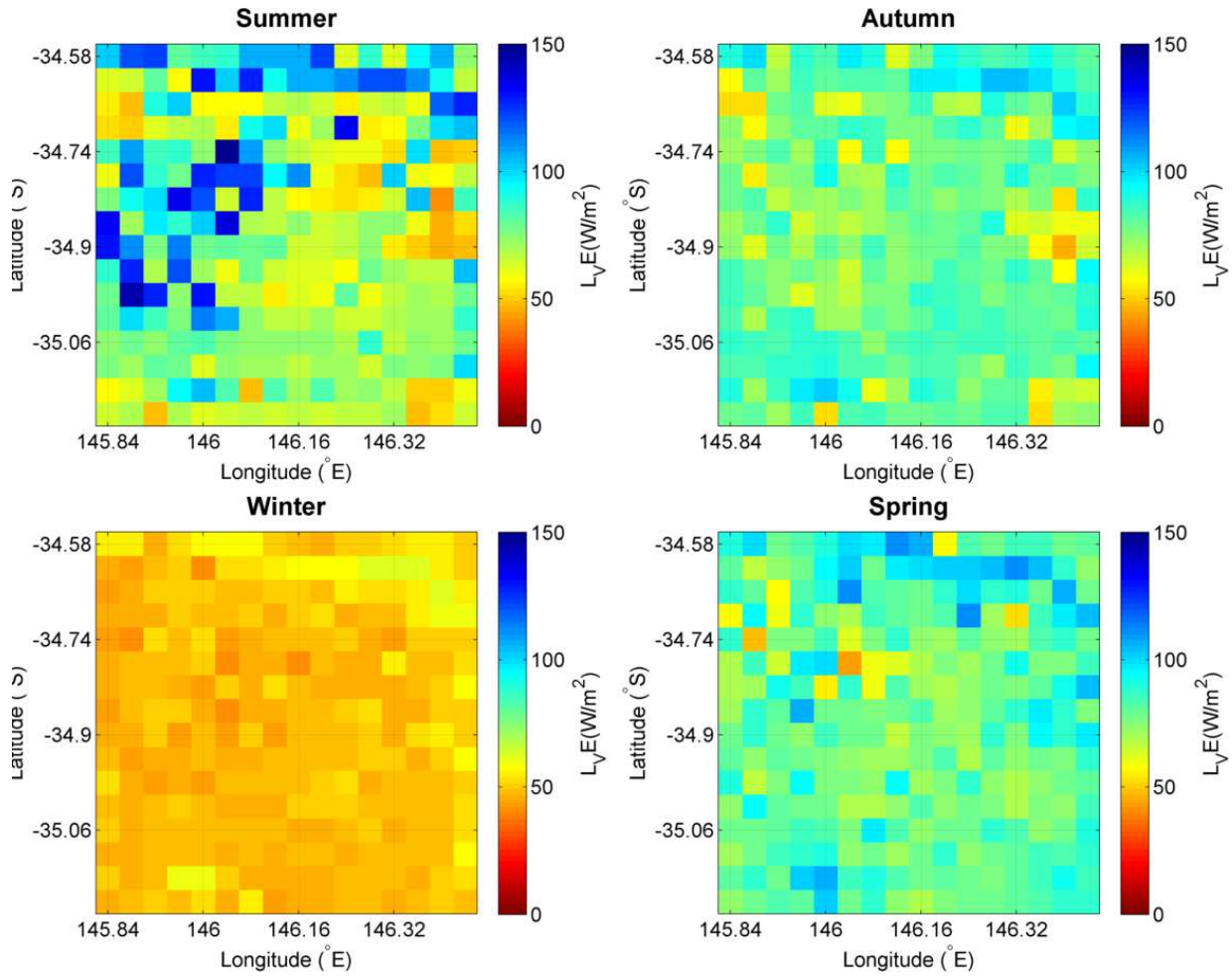

Figure 4.17: *Standard deviation L_vE derived based on PT-JPL at 12 pm for each season within Yanco.*

and surface resistance which are calculated from NDVI data, any errors in NDVI data will affect the performance of SEBS and PM-Mu. PT-JPL was also shown to be able to represent the spatial distribution of ET within the larger Yanco area, thereby making it suitable for further application in the validation of land surface model simulations.

Finally, measurements and estimation of ET in semi-arid and arid environments is undeniably a very challenging matter due to its small magnitude in comparison to other energy terms of the surface energy balance equation. Yet, the ability to manage water resources for such environments are even more crucial. Accordingly, it has been shown in this study how errors in the measurement of R_n, G and the non-closure of the energy balance complicates the validation of ET models with EC systems. Therefore, it is recommended that future studies for the validation of ET models should use different statistical parameters, considering both temporal and absolute accuracy to ensure that comparisons with EC measurements are not biased by errors in measurements of input data or observational data.

Chapter 5

Assimilation of AMSR2 soil moisture

Data assimilation (DA) has continued to facilitate root-zone soil moisture estimation from satellite data using land surface models (Reichle, 2008; Reichle et al., 2008; Walker et al., 2002). DA methods merge uncertain observation data with imperfect model output to provide an improved estimate of the quantity (e.g. soil moisture) under investigation. DA of soil moisture usually uses model estimates of soil moisture from land surface models to complement remotely sensed observations in order to provide an integrated and continuous soil moisture information. Land surface models employ land-atmosphere physics together with various data inputs including land cover, soil and meteorological forcing data to determine the profile soil moisture. Land surface models are capable to provide continuous soil moisture estimates at various time scales, and the spatial resolution of the model estimate is only limited by the resolution of the input data. As a result, land surface models can provide valuable soil moisture information to be integrated with remotely sensed satellite soil moisture through DA methods.

The DA section of this report examines the contribution of soil moisture on the estimation of evapotranspiration. This is achieved by estimating surface soil moisture through assimilation of AMSR2 soil moisture into the Joint UK Land Environment Simulator (JULES) at the flux tower site. The open loop and updated soil moisture estimates are compared against the in-situ soil moisture, after which the modeled evapotranspiration are examined in relation to the observation data.

5.1 The land surface model and data sources

The soil moisture assimilation is conducted for a single $25km$ AMSR2 grid which overlaps the flux tower location. The rationale to perform the assimilation for this single grid is to compare the updated flux outputs against those obtained from the flux tower observation system. The land surface soil moisture model estimates are generated for the $25km$ grid where they are updated with the overlapping AMSR2 soil moisture. The chosen AMSR2 data is the $25km$ Level 3 (L3) soil moisture, which was used as observation data to drive the assimilation from May 2012 to May 2015.

The land surface soil moisture estimates are obtained through the Joint UK Land Environment Simulator (JULES). The JULES model is a widely used tiled model of sub-grid heterogeneity which simulates water and energy fluxes between a vertical profile of soil layers, land surface, vegetation, and the atmosphere (Best et al., 2011). JULES uses meteorological forcing data, surface land cover data, soil information, and values for prognostic variables. The model initialization is conducted for several variables including the temperatures and the liquid and frozen moisture contents of the soil layers; temperature, density, and albedo of snowpack if present; the temperature and intercepted rain and snow on the vegetation canopy; the temperature and depth of ponded water on the soil surface; and an empirical vegetation growth index. JULES requires specification of layer thicknesses of the soil profile, and the proportion of nine land surface categories including broadleaf, needleleaf, grass (temperate and tropical), shrub, urban, inland water, bare soil, and ice-covered surfaces.

The land cover data used is the Australian National Dynamic Land Cover Dataset (DLCD) (Lymburner et al., 2011). The DLCD was generated from a 16-day Enhanced Vegetation Index composite collected at 250m resolution from the Moderate Resolution Imaging Spectroradiometer (MODIS) for the period of 2000 to 2008. The DLCD has land cover features clustered into 34 ISO classes with descriptions for the structural character of vegetation, ranging from cultivated and managed land covers (crops and pastures) to natural land covers such as closed forest and sparse, open grasslands. The DLCD data was used to determine the proportion of the nine land cover types for the JULES model.

The soils information is derived from the Digital Atlas of Australian Soils (McKenzie et al., 2000) which was obtained from the Australian Soil Resource Information System (ASRIS). AS-

RIS provides a digital map of soil types and their descriptions, typical ranges for soil properties for each soil type, morphology, and physical properties of soil profiles. The soil classification system was based on the widely applied Factual Key of Northcote (1979) and later revised to the Australian Soil Classification (Isbell et al., 1997; Isbell, 2002) into 6 textural groups including sand, sandy loams, loams, clay loams, and light clays. Soil properties in the Digital Atlas of Australian Soils (DAAS) include information on texture, clay content, bulk density, saturated hydraulic conductivity, and soil layer thickness for horizons A and B (McKenzie et al., 2000; McKenzie and Hook, 1992). The horizon A data was used to estimate the surface soil information whereas the horizon B data was used to estimate the soil properties for the root-zone soil moisture. The soil properties information are summarized to a 90% confidence interval by providing the mean/median value, and the dispersion of 5th and 95th percentile of the average interpreted value.

The meteorological forcing data including short and long wave incoming radiation, air temperature, precipitation, wind speed, pressure, and specific humidity are obtained from the weather station at the flux tower location. The land cover and the soils data are accordingly summarized to the $25km$ AMSR2 grid through spatial overlap, and subsequent determination of the proportions of constituent land cover and soils classes within the single grid. Using the forcing data together with its land cover and soils information, the JULES model was applied to simulate hourly soil moisture for 4 layer thicknesses including 0-8cm, 8-30cm, 30-60cm, and 60-90cm to correspond to the in-situ soil moisture.

5.2 Soil moisture assimilation scheme

The assimilation scheme used is the evolutionary data assimilation (EDA), a unified framework combining stochastic capabilities from multi-objective evolutionary strategy together with temporal updating from traditional data assimilation. The multi-objective evolutionary algorithm exemplified in the EDA is the Non-Dominated Sorting Genetic Algorithm e II (NSGA-II), which was developed by (Deb and Goel, 2001; Deb et al., 2002). The EDA procedure, shown in Figure 5.1, begins with an initial evolutionary cycle which involves the creation of a random population of members, followed by an assessment of the members based on evaluation objectives, and the selection of half of the population members for reproduction. For subsequent cycles of

evolution, the selected high performing members are combined with the new members to form a new population which undergoes another evaluation, selection, and reproduction. Each cycle of the evolution of the population members is called a generation. The initial genotype for population members is generated using the minimum and maximum bounds for model parameters, states, and forcing variables for JULES. This initial population is generated using the Latin hypercube sampling, which provides values over the entire length of the variable distributions. Subsequent populations were generated based on the evolutionary operators including tournament selection, mutation and crossover.

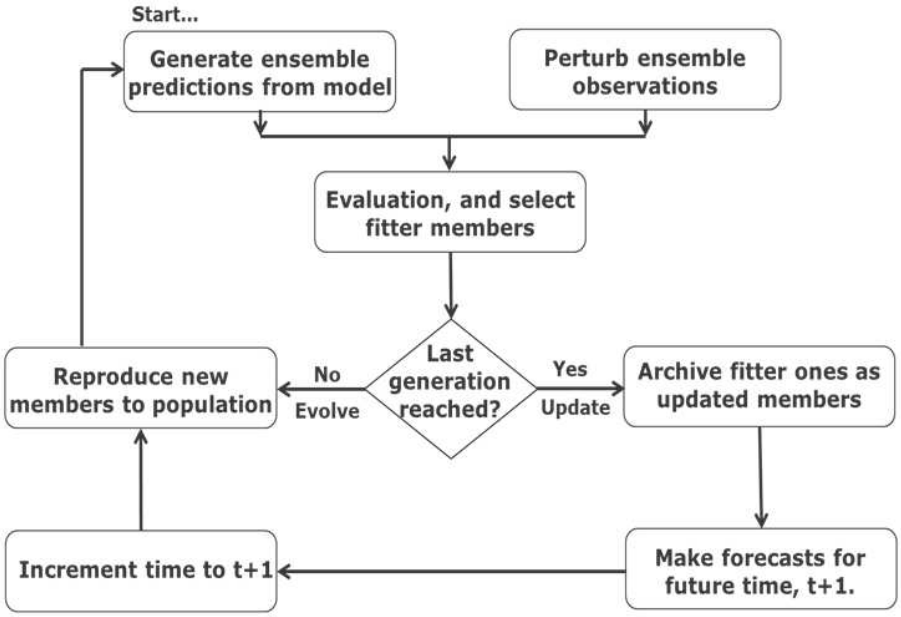

Figure 5.1: *Computational procedure of the EDA approach, showing the evaluation, selection and reproduction of the population and its update through time.*

5.3 Assimilation outputs

The open loop and updated soil moisture are evaluated by comparing their agreement to the in-situ data for 0-8cm soil depth in Figure 5.2. The updated estimate showed a slight improvement in its output, but the estimated soil moisture is almost similar in both cases.

The soil moisture estimation in both cases compared against in-situ data at the root zone for 0-30cm and 30-60cm are shown in Figure 5.3. The updated output is superior to both the open loop and the calibration estimates for both soil depths.

The slightly superior estimation of the updated output compared to open loop is further examined in relation to their estimation of evapotranspiration. The open loop and the soil moisture updated estimation of the daily evapotranspiration (from canopy and soil) are compared

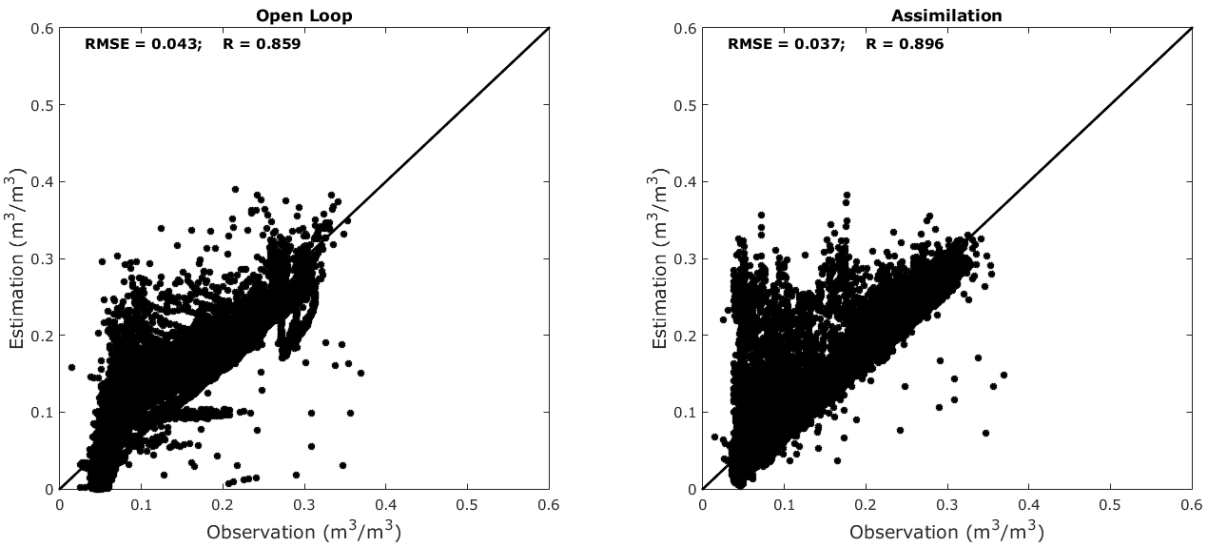

Figure 5.2: *Assessment of open loop, calibration, and updated estimates against AMSR2 soil moisture as observation data set.*

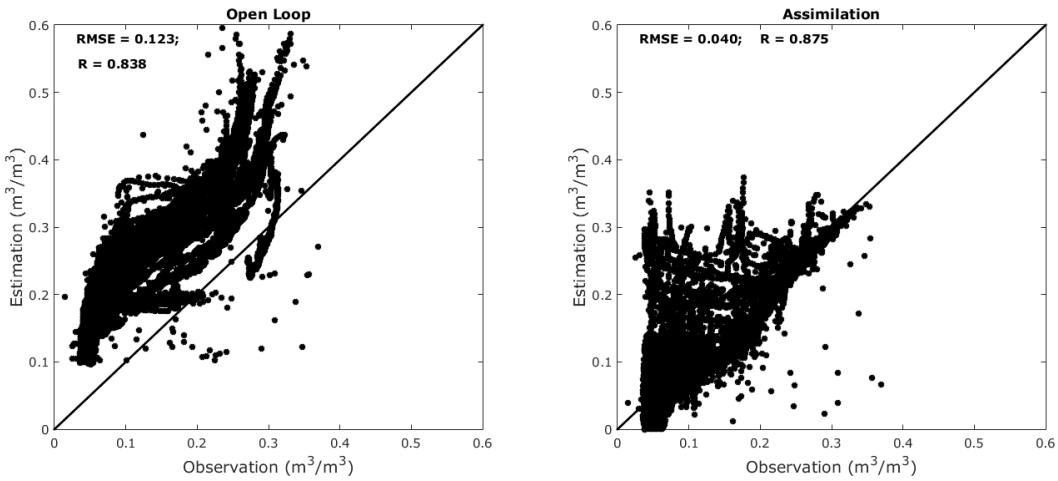

(a) Soil depth: 0-30cm

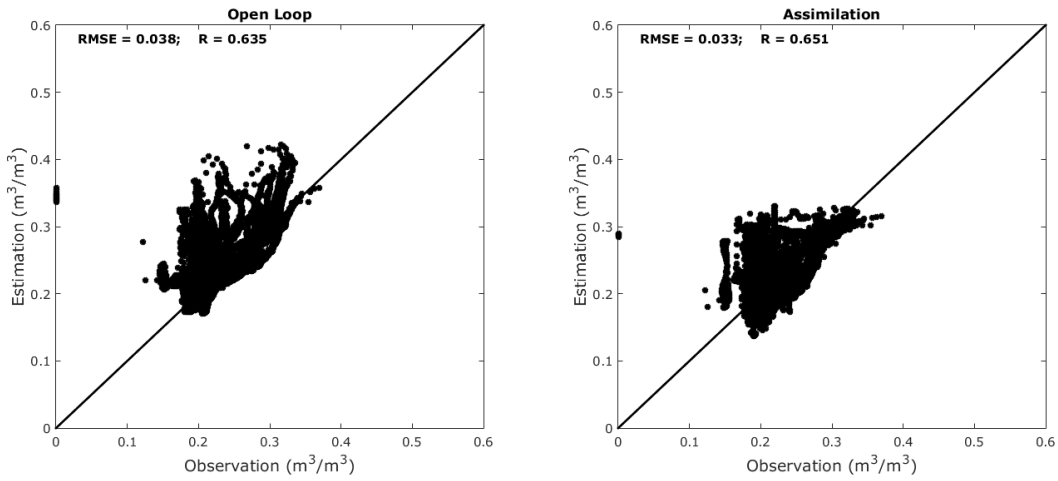

(b) Soil depth: 30-60cm

Figure 5.3: *Assessment of open loop, calibration, and updated estimates against in-situ soil moisture at the root-zone.*

against the in-situ flux tower observation in Figure 5.4.

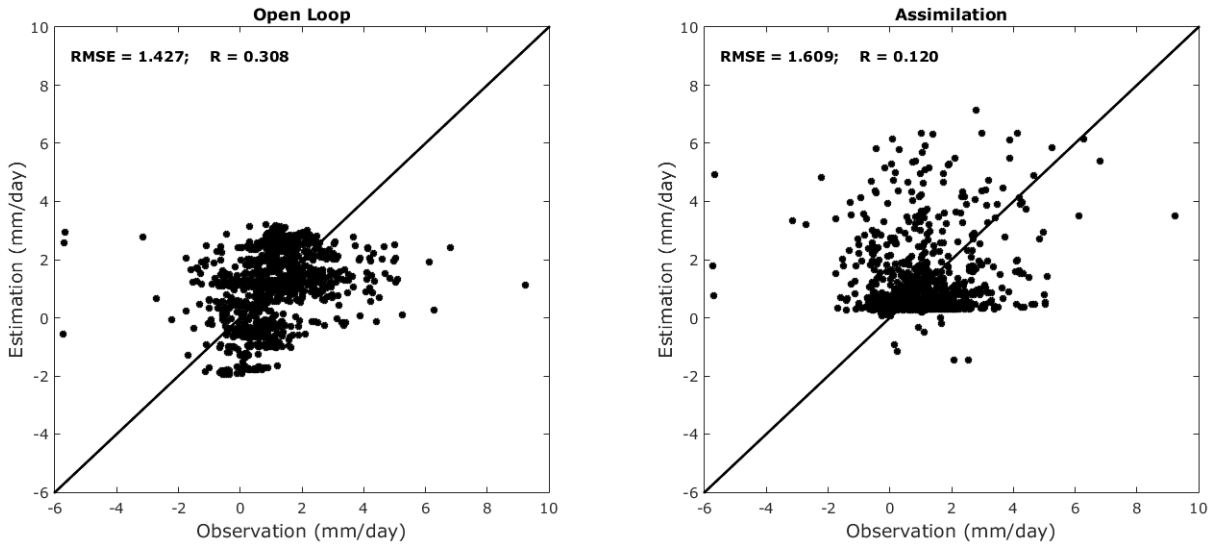

Figure 5.4: *Assessment of calibration and updated estimates against in-situ sensible heat flux at the tower location.*

Combining the soil moisture and evapotranspiration results, we found that data assimilation procedure does improve soil moisture estimation but this contribution is not directly positive for estimating evapotranspiration. These findings suggest inconsistent relationship between water and energy budgets in the JULES model.

Chapter 6

Summary and conclusion

The report outlined project activities undertaken during the past Japanese fiscal year. These activities include:

- Maintenance of the tower instrumentation and monitoring of the observation data from the flux tower and weather station.
- Validation of AMSR-2 soil moisture retrieved using JAXA and LPRM algorithms against in-situ soil moisture obtained from representative monitoring stations. The two soil moisture retrieval methods have similar accuracies with differences in performance observed for C-band and X-band.
- Evaluation of the MTSAT evapotranspiration against those obtained from the EC flux tower and scintillometer observations.
- Data assimilation of AMSR2 soil moisture into the JULES model using the EDA algorithm. Improvements found in soil moisture estimation do not directly enhance the estimation of evapotranspiration, suggesting inconsistencies in water and energy budgets of the JULES model.

Bibliography

Adams, J. R., McNairn, H., Berg, A. A., and Champagne, C. (2015). Evaluation of near-surface soil moisture data from an AAFC monitoring network in Manitoba, Canada: Implications for L-band satellite validation. *Journal of Hydrology*, 521:582 – 592.

Al Bitar, A., Leroux, D., Kerr, Y. H., Merlin, O., Richaume, P., Sahoo, A., and Wood, E. F. (2012). Evaluation of SMOS soil moisture products over continental US using the SCAN/SNOTEL network. *Geoscience and Remote Sensing, IEEE Transactions on*, 50(5):1572–1586.

Al-Yaari, A., Wigneron, J.-P., Ducharne, A., Kerr, Y., Wagner, W., De Lannoy, G., Reichle, R., Al Bitar, A., Dorigo, W., Richaume, P., and Mialon, A. (2014). Global-scale comparison of passive (SMOS) and active (ASCAT) satellite based microwave soil moisture retrievals with soil moisture simulations (MERRA-Land). *Remote Sensing of Environment*, 152:614–626.

Albergel, C., de Rosnay, P., Gruhier, C., Muñoz-Sabater, J., Hasenauer, S., Isaksen, L., Kerr, Y., and Wagner, W. (2012). Evaluation of remotely sensed and modelled soil moisture products using global ground-based in situ observations. *Remote Sensing of Environment*, 118:215–226.

Baghdadi, N., Cerdan, O., Zribi, M., Auzet, V., Darboux, F., El Hajj, M., and Kheir, R. B. (2007). Operational performance of current synthetic aperture radar sensors in mapping soil surface characteristics in agricultural environments: application to hydrological and erosion modelling. *Hydrological Processes*, 22(1):9–20.

Baldocchi, D., Falge, E., Gu, L., Olson, R., Hollinger, D., Running, S., Anthoni, P., Bernhofer, C., Davis, K., Evans, R., Fuentes, J., Goldstein, A., Katul, G., Law, B., Lee, X., Malhi, Y., Meyers, T., Munger, W., Oechel, W., Paw, K. T., Pilegaard, K., Schmid, H. P., Valentini, R.,

Verma, S., Vesala, T., Wilson, K., and Wofsy, S. (2001). Fluxnet: A new tool to study the temporal and spatial variability of ecosystem-scale carbon dioxide, water vapor, and energy flux densities. *Bull. Amer. Meteor. Soc.*, 82(11):2415–2434.

Beringer, J., Hutley, L. B., Tapper, N. J., and Cernusak, L. A. (2007). Savanna fires and their impact on net ecosystem productivity in North Australia. *Global Change Biology*, 13(5):990–1004.

Best, M. J., Pryor, M., Clark, D. B., Rooney, G. G., Essery, R. L. H., Mnard, C. B., Edwards, J. M., Hendry, M. A., Porson, A., Gedney, N., Mercado, L. M., Sitch, S., Blyth, E., Boucher, O., Cox, P. M., Grimmond, C. S. B., and Harding, R. J. (2011). The Joint UK Land Environment Simulator (JULES), Model description - Part 1: Energy and water fluxes. *Geosci. Model Dev. Discuss.*, 4:595–640, doi:10.5194/gmdd–4–595–2011.

Beyrich, F., De Bruin, H. A. R., Meijninger, W. M. L., Schipper, J. W., and Lohse, H. (2002). Results from one-year continuous operation of a large aperture scintillometer over a heterogeneous land surface. *Boundary-Layer Meteorology*, 105(1):85–97.

Brunsell, N. A., Ham, J. M., and Arnold, K. A. (2011). Validating remotely sensed land surface fluxes in heterogeneous terrain with large aperture scintillometry. *International Journal of Remote Sensing*, 32(21):6295–6314.

Cammalleri, C., Anderson, M. C., and Kustas, W. P. (2013). Upscaling of evapotranspiration fluxes from instantaneous to daytime scales for thermal remote sensing applications. *Hydrology and Earth System Sciences Discussions*, 10(6):7325–7350.

Champagne, C., Rowlandson, T., Berg, A., Burns, T., L'Heureux, J., Tetlock, E., Adams, J. R., McNairn, H., Toth, B., and Itenfisu, D. (2015). Satellite surface soil moisture from SMOS and Aquarius: Assessment for applications in agricultural landscapes. *International Journal of Applied Earth Observation and Geoinformation.*

Chehbouni, A., Watts, C., Lagouarde, J.-P., Kerr, Y. H., Rodriguez, J.-C., Bonnefond, J.-M., Santiago, F., Dedieu, G., Goodrich, D. C., and Unkrich, C. (2000). Estimation of heat and momentum fluxes over complex terrain using a large aperture scintillometer. *Agricultural and forest meteorology*, 105(1):215–226.

Collow, T. W., Robock, A., Basara, J. B., and Illston, B. G. (2012). Evaluation of SMOS retrievals of soil moisture over the central United States with currently available in situ observations. *Journal of Geophysical Research: Atmospheres*, 117(D9):D9. D09113.

Deb, K. and Goel, T. (2001). Controlled Elitist Non-dominated Sorting Genetic Algorithms for Better Convergence. volume 1993, pages 67–81, Swiss Federal Institute of Technology, Zurich Switzerland. Evolutionary multi-criterion optimization : first international conference, EMO 2001, Springer.

Deb, K., Pratap, A., Agrawal, S., and Meyarivan, T. (2002). A fast and elitist multiobjective genetic algorithm: NSGA-II. *IEEE Transactions on Evolutionary Computation*, 6(2):182–197.

de Nijs, A., Parinussa, R., de Jeu, R., Schellekens, J., and Holmes, T. (2015). A methodology to determine radio-frequency interference in amsr2 observations. *Geoscience and Remote Sensing, IEEE Transactions on*, 53(9):5148–5159.

Draper, C. S., Walker, J. P., Steinle, P. J., de Jeu, R. A. M., and Holmes, T. R. H. (2009). An evaluation of AMSR-E derived soil moisture over Australia. *Remote Sensing of Environment*, 113(4):703–710.

El Maayar, M., Chen, J. M., and Price, D. T. (2008). On the use of field measurements of energy fluxes to evaluate land surface models. *Ecological Modelling*, 214(2-4):293–304.

Ershadi, A., McCabe, M., Evans, J., Chaney, N., and Wood, E. (2014). Multi-site evaluation of terrestrial evaporation models using FLUXNET data. *Agricultural and Forest Meteorology*, 187(0):46–61.

Ershadi, A., McCabe, M., Evans, J., and Wood, E. (2015). Impact of model structure and parameterization on penman-monteith type evaporation models. *Journal of Hydrology*, 525:521–535.

Ezzahar, J., Chehbouni, A., Hoedjes, J., Ramier, D., Boulain, N., Boubkraoui, S., Cappelaere, B., Descroix, L., Mougenot, B., and Timouk, F. (2009). Combining scintillometer measurements and an aggregation scheme to estimate area-averaged latent heat flux during the AMMA experiment. *Journal of Hydrology*, 375(1):217–226.

Finnigan, J. J., Clement, R., Malhi, Y., Leuning, R., and Cleugh, H. A. (2003). A re-evaluation of long-term flux measurement techniques part I: averaging and coordinate rotation. *Boundary-Layer Meteorology*, 107(1):1–48.

Fisher, J. B., Tu, K. P., and Baldocchi, D. D. (2008). Global estimates of the land-atmosphere water flux based on monthly AVHRR and ISLSCP-II data, validated at 16 FLUXNET sites. *Remote Sensing of Environment*, 112(3):901–919.

Foken, T., Aubinet, M., Finnigan, J. J., Leclerc, M. Y., Mauder, M., and Paw U, K. T. (2011). Results of a panel discussion about the energy balance closure correction for trace gases. *Bulletin of the American Meteorological Society*, 92(4):ES13—-ES18.

Fujii, H., Koike, T., and Imaoka, K. (2009). Improvement of the AMSR-E Algorithm for Soil Moisture Estimation by Introducing a Fractional Vegetation Coverage Dataset Derived from MODIS Data. *Journal of The Remote Sensing Society of Japan*, 29(1):282–292.

García, M., Sandholt, I., Ceccato, P., Ridler, M., Mougin, E., Kergoat, L., Morillas, L., Timouk, F., Fensholt, R., and Domingo, F. (2013). Actual evapotranspiration in drylands derived from in-situ and satellite data: Assessing biophysical constraints. *Remote Sensing of Environment*, 131:103–118.

Hornbuckle, J., Christen, E. W., Land, C., and Water. (1999). *Physical properties of soils in the Murrumbidgee and Coleambally irrigation areas / J. Hornbuckle and E. Christen*. CSIRO Land and Water Canberra, A.C.T.

Hutley, L. B., Leuning, R., Beringer, J., and Cleugh, H. A. (2005). The utility of the eddy covariance techniques as a tool in carbon accounting: tropical savanna as a case study. *Australian Journal of Botany*, 53(7):663.

Imaoka, K., Kachi, M., Fujii, H., Murakami, H., Hori, M., Ono, A., Igarashi, T., Nakagawa, K., Oki, T., Honda, Y., and Shimoda, H. (2010). Global Change Observation Mission (GCOM) for Monitoring Carbon, Water Cycles, and Climate Change. *Proceedings of the IEEE*, 98(5):717–734.

Isbell, R., McDonald, W., and Ashton, L. (1997). Concepts and rationale of the australian soil classification. Technical report, CSIRO, ACLEP Land and Water, Canberra.

Isbell, R. F. (2002). The australian soil classification. Technical report, CSIRO Publishing, Melbourne, Revised Edition.

Jacquette, E., Al Bitar, A., Mialon, A., Kerr, Y., Quesney, A., Cabot, F., and Richaume, P. (2010). SMOS CATDS level 3 global products over land.

Kaimal, J. C. and Finnigan, J. J. (1994). *Atmospheric boundary layer flows: their structure and measurement*. Oxford University Press, New York.

Kerr, Y. H., Waldteufel, P., Wigneron, J. P., Martinuzzi, J. M., Font, J., and Berger, M. (2001). Soil moisture retrieval from space: The Soil Moisture and Ocean Salinity (SMOS) mission. *IEEE Transactions on Geoscience and Remote Sensing*, 39(8):1729–1735.

Kim, S., Liu, Y., Johnson, F. M., Parinussa, R. M., and Sharma, A. (2015). A global comparison of alternate AMSR2 soil moisture products: Why do they differ? *Remote Sensing of Environment*, 161:43–62.

Lagouarde, J.-P., Bonnefond, J.-M., Kerr, Y. H., McAneney, K. J., and Irvine, M. (2002). Integrated sensible heat flux measurements of a two-surface composite landscape using scintillometry. *Boundary-layer meteorology*, 105(1):5–35.

Lagouarde, J.-P., Irvine, M., Bonnefond, J.-M., Grimmond, C. S. B., Long, N., Oke, T. R., Salmond, J. A., and Offerle, B. (2006). Monitoring the Sensible Heat Flux over Urban Areas using Large Aperture Scintillometry: Case Study of Marseille City During the Escompte Experiment. *Boundary-Layer Meteorology*, 118(3):449–476.

Liu, S. M., Xu, Z. W., Zhu, Z. L., Jia, Z. Z., and Zhu, M. J. (2013). Measurements of evapotranspiration from eddy-covariance systems and large aperture scintillometers in the Hai River Basin, China. *Journal of Hydrology*, 487(0):24–38.

Lymburner, L., Tan, P., Mueller, N., Thackway, R., Lewis, A., Thankappan, M., Randall, L., Islam, A., and Senarath, U. (2011). The national dynamic land cover dataset (DLCD), record 2011/31, www.ga.gov.au/landcover,. Technical report, Geoscience Australia.

Mackay, D. S., Samanta, S., Ahl, D. E., Ewers, B. E., Gower, S. T., and Burrows, S. N.

(2003). Automated Parameterization of Land Surface Process Models Using Fuzzy Logic. *Transactions in GIS*, 7(1):139–153.

Maeda, T., Imaoka, K., Kachi, M., Fujii, H., Shibata, A., Naoki, K., Kasahara, M., Ito, N., Nakagawa, K., and Oki, T. (2011). Status of GCOM-W1/AMSR2 development, algorithms, and products. *Proc. SPIE*, 8176:81760N–81760N–7.

Maeda, T. and Taniguchi, Y. (2013). Descriptions of GCOM-W1 AMSR2 Level 1R and Level 2 Algorithms. Online. NDX-120015A.

McCabe, M. F., Ershadi, A., Jimenez, C., Miralles, D. G., Michel, D., and Wood, E. F. (2015). The GEWEX LandFlux project: evaluation of model evaporation using tower-based and globally-gridded forcing data. *Geoscientific Model Development Discussions*, 8(8):6809–6866.

McKenzie, N., Jacquier, D., Ashton, L., and Cresswell, H. (2000). Estimation of soil properties using the atlas of australian soils. Technical report, CSIRO Land and Water Technical Report 11/00. Available from http://www.clw.csiro.au/publications/technical2000/.

McKenzie, N. J. and Hook, J. (1992). Interpretations of the atlas of australian soils. consulting report to the environmental resources information network (erin). Technical report, CSIRO Division of Soils Technical Report 94.

McJannet, D., Cook, F., McGloin, R., McGowan, H., Burn, S., and Sherman, B. (2013). Long-term energy flux measurements over an irrigation water storage using scintillometry. *Agricultural and Forest Meteorology*, 168(0):93–107.

McJannet, D. L., Cook, F. J., McGloin, R. P., McGowan, H. A., and Burn, S. (2011). Estimation of evaporation and sensible heat flux from open water using a large-aperture scintillometer. *Water Resources Research*, 47(5):n/a—-n/a.

Meijninger, W. M. L. and De Bruin, H. A. R. (2000). The sensible heat fluxes over irrigated areas in western Turkey determined with a large aperture scintillometer. *Journal of Hydrology*, 229(1):42–49.

Moncrieff, J., Clement, R., Finnigan, J., and Meyers, T. (2005). Averaging, Detrending, and Filtering of Eddy Covariance Time Series. In Lee, X., Massman, W., and Law, B., edi-

tors, *Handbook of Micrometeorology*, volume 29 of *Atmospheric and Oceanographic Sciences Library*, pages 7–31. Springer Netherlands.

Monteith, J. L. (1965). Evaporation and environment. In *Symp. Soc. Exp. Biol*, volume 19, page 4.

Mu, Q., Zhao, M., and Running, S. W. (2011). Improvements to a MODIS global terrestrial evapotranspiration algorithm. *Remote Sensing of Environment*, 115(8):1781–1800.

Mu, Q., Zhao, M., and Running, S. W. (2013). MODIS Global Terrestrial Evapotranspiration (ET) Product (NASA MOD16A2/A3). *Algorithm Theoretical Basis Document, Collection*, 5.

Njoku, E. G., Ashcroft, P., Chan, T. K., and Li, L. (2005). Global survey and statistics of radio-frequency interference in AMSR-E land observations. *Geoscience and Remote Sensing, IEEE Transactions on*, 43(5):938–947.

Njoku, E. G., Jackson, T. J., Lakshmi, V., Chan, T. K., and Nghiem, S. V. (2003). Soil moisture retrieval from AMSR-E. *IEEE Transactions on Geoscience and Remote Sensing*, 41(2 PART 1):215–228.

Northcote, K. (1979). A factual key for the recognition of australian soils. Technical report, Glenside, South Australia: Rellim Technical Publications.

Owe, M., de Jeu, R., and Holmes, T. (2008). Multisensor historical climatology of satellite-derived global land surface moisture. *Journal of Geophysical Research F: Earth Surface*, 113(F1):F1.

Owe, M., De Jeu, R., and Walker, J. (2001). A methodology for surface soil moisture and vegetation optical depth retrieval using the microwave polarization difference index. *Geoscience and Remote Sensing, IEEE Transactions on*, 39(8):1643–1654.

Panciera, R., Walker, J. P., Jackson, T. J., Gray, D. A., Tanase, M. A., Ryu, D., Monerris, A., Yardley, H., Rudiger, C., Wu, X., Gao, Y., and Hacker, J. M. (2014). The Soil Moisture Active Passive Experiments (SMAPEx): Toward Soil Moisture Retrieval From the SMAP Mission. *Geoscience and Remote Sensing, IEEE Transactions on*, 52(1):490–507.

Parinussa, R. M., Holmes, T. R. H., Wanders, N., Dorigo, W. A., and de Jeu, R. A. M. (2015). A preliminary study toward consistent soil moisture from AMSR2. *Journal of Hydrometeorology*, 16(2):932–947.

Pauwels, V., Timmermans, W., and Loew, A. (2008). Comparison of the estimated water and energy budgets of a large winter wheat field during AgriSAR 2006 by multiple sensors and models. *Journal of Hydrology*, 349(3):425–440.

Polhamus, A., Fisher, J. B., and Tu, K. P. (2013). What controls the error structure in evapotranspiration models? *Agricultural and Forest Meteorology*, 169:12–24.

Reichle, R. H. (2008). Data assimilation methods in the earth sciences. *Advances in Water Resources*, 31(11):1411–1418.

Reichle, R. H., Crow, W. T., Koster, R. D., Sharif, H. O., and Mahanama, S. P. P. (2008). Contribution of soil moisture retrievals to land data assimilation products. *Geophysical Research Letters*, 35(L01404):doi:10.1029/2007GL031986.

Rowlandson, T. L., Hornbuckle, B. K., Bramer, L. M., Patton, J. C., and Logsdon, S. D. (2012). Comparisons of Evening and Morning SMOS Passes Over the Midwest United States. *Geoscience and Remote Sensing, IEEE Transactions on*, 50(5):1544–1555.

Samain, B., Defloor, W., and Pauwels, V. R. N. (2012a). Continuous Time Series of Catchment-Averaged Sensible Heat Flux from a Large Aperture Scintillometer: Efficient Estimation of Stability Conditions and Importance of Fluxes under Stable Conditions. *Journal of Hydrometeorology*, 13(2):423–442.

Samain, B., Ferket, B. V. A., Defloor, W., and Pauwels, V. R. N. (2011). Estimation of catchment averaged sensible heat fluxes using a large aperture scintillometer. *Water Resources Research*, 47(5).

Samain, B., Simons, G. W. H., Voogt, M. P., Defloor, W., Bink, N.-J., Pauwels, V. R. N., and Loew, A. (2012b). Consistency between hydrological model, large aperture scintillometer and remote sensing based evapotranspiration estimates for a heterogeneous catchment. *Hydrology & Earth System Sciences*, 16(7).

Savage, M. J. (2009). Estimation of evaporation using a dual-beam surface layer scintillometer and component energy balance measurements. *Agricultural and Forest Meteorology*, 149(3):501–517.

Smith, A. B., Walker, J. P., Western, A. W., Young, R. I., Ellett, K. M., Pipunic, R. C., Grayson, R. B., Siriwardena, L., Chiew, F. H. S., and Richter, H. (2012). The Murrumbidgee soil moisture monitoring network data set. *Water Resources Research*, 48(7):W07701.

Smith, A. B., Walker, J. P., Western, A. W. Young, R. I., Ellett, K. M., Pipunic, R. C.and Grayson, R. B., Siriwardena, L.and Chiew, F. H. S., and Richter, H. (2012). The murrumbidgee soil moisture monitoring network data set. *Water Resources Research*, 48(W07701):doi:10.1029/2012WR011976.

Su, C. H., Ryu, D., Young, R. I., Western, A. W., and Wagner, W. (2013). Inter-comparison of microwave satellite soil moisture retrievals over the Murrumbidgee Basin, southeast Australia. *Remote Sensing of Environment*, 134(2013):1–11.

Su, Z. (2002). The Surface Energy Balance System (SEBS) for estimation of turbulent heat fluxes. *Hydrology and Earth System Sciences Discussions*, 6(1):85–100.

Taylor, K. E. (2001). Summarizing multiple aspects of model performance in a single diagram. *Journal of Geophysical Research: Atmospheres*, 106(D7):7183–7192.

Twine, T. E., Kustas, W. P., Norman, J. M., Cook, D. R., Houser, P. R., Meyers, T. P., Prueger, J. H., Starks, P. J., and Wesely, M. L. (2000). Correcting eddy-covariance flux underestimates over a grassland. *Agricultural and Forest Meteorology*, 103(3):279–300.

Walker, J., Willgoose, G., and Kalma, J. (2002). Three-dimensional soil moisture profile retrieval by assimilation of near-surface measurements: Simplified kalman filter covariance forecasting and field application. *Water Resources Research*, 38(12):1301.

Ward, H. C., Evans, J. G., and Grimmond, C. S. B. (2013). Multi-season eddy covariance observations of energy, water and carbon fluxes over a suburban area in Swindon, UK. *Atmospheric Chemistry and Physics*, 13(9):4645–4666.

Ward, H. C., Evans, J. G., and Grimmond, C. S. B. (2014). Multi-scale sensible heat fluxes in the suburban environment from large-aperture scintillometry and eddy covariance. *Boundary-Layer Meteorology*, 152(1):65–89.

Webb, E. K., Pearman, G. I., and Leuning, R. (1980). Correction of flux measurements for density effects due to heat and water vapour transfer. *Quarterly Journal of the Royal Meteorological Society*, 106(447):85–100.

Wigneron, J.-P., Kerr, Y., Waldteufel, P., Saleh, K., Escorihuela, M.-J., Richaume, P., Ferrazzoli, P., de Rosnay, P., Gurney, R., Calvet, J.-C., Grant, J., Guglielmetti, M., Hornbuckle, B., Mtzler, C., Pellarin, T., and Schwank, M. (2007). L-band Microwave Emission of the Biosphere (L-MEB) Model: Description and calibration against experimental data sets over crop fields . *Remote Sensing of Environment*, 107(4):639 – 655.

Yee, M. S., Pauwels, V. R., Daly, E., Beringer, J., Rüdiger, C., McCabe, M. F., and Walker, J. P. (2015). A comparison of optical and microwave scintillometers with eddy covariance derived surface heat fluxes. *Agricultural and Forest Meteorology*, 213:226–239.

Yee, M., W., J. P., Monerris, A., Rüdiger, C., and Jackson, T. J. (2016). On the temporal and spatial variability of near-surface soil moisture for the identification of representative *in situ* soil moisture monitoring stations. *Journal of Hydrology*. In Press.

Zeweldi, D. A., Gebremichael, M., Wang, J., Sammis, T., Kleissl, J., and Miller, D. (2010). Intercomparison of sensible heat flux from large aperture scintillometer and eddy covariance methods: Field experiment over a homogeneous semi-arid region. *Boundary-layer meteorology*, 135(1):151–159.

Validation of global water and energy balance monitoring in the Australian Murray-Darling Basin using GCOM-W1 data

MONASH University
Engineering